STUDY OF GRANULAR TEMPERATURES IN GAS-SOLID FLUIDIZED BED BY DIFFUSING-WAVE SPECTROSCOPY

by

Liansong Xie

A thesis submitted to the University of Edinburgh for the degree of

Doctor of Philosophy

School of Engineering and Electronics
The University of Edinburgh
Edinburgh EH9 3JL

2004

Abstract

The thesis is motivated by the goal of developing techniques for measuring granular temperature in the fluidized bed by a non-intrusive method.

Experimental investigations have been carried out on Q-Cel® hollow glass micro-spheres with average diameter 60μm in several two dimensional rectangular air-fluidized beds. The particle bulk and effective densities were 110kg/m^3 and 200 kg/m^3 respectively. Fluidized bed expansion and pressure drop across the bed were studied. Despite theoretically belonging to Group C (cohesive, difficult to be fluidized) according to Geldart's powder classification, these micro-spheres fluidized easily and the bed expansion was extremely high when the gas velocity was increased above the minimum fluidization value. Using the diffusing-wave spectroscopy (DWS) technique in transmission and backscattering geometry, granular temperatures were determined throughout the gas fluidised bed for superficial velocities up to and somewhat beyond the minimum bubbling velocity, which was more than 4 times the minimum fluidisation velocity. The granular temperature was found to increase smoothly with superficial velocity between the minimum fluidisation and minimum bubbling velocities, contrary to the results of earlier workers who also used DWS, but consistent with the results of other workers using less direct methods. It was found that the granular temperature at a set superficial velocity increased with height above the distributor whilst the pressure gradient remained constant. This, combined with increasing laser light transmission, suggested particle clustering with the cluster size decreasing with height. Granular temperature was found to vary symmetrically about the bed centreline where it was also maximal, corresponding to velocity profiles observed by others for similar bed

geometries. Preliminary studies of particle microdynamics in a laboratory scale circulating fluidized bed were also made.

Acknowledgements

I would like to thank my supervisor, Dr. Don Glass, who has provided invaluable guidance throughout this study. I must also acknowledge his patience and support which helped me to conclude this project. I would also like to thank Dr. Mark Biggs for his supervision during my PhD study.

None of the work presented here would have been accomplished without the help from Dr. Stefan Egelhaaf. It was really a pleasure to discuss my research with Dr. Sara Romer and Dr. Franck Clement in the Dynamic Light Scattering (DLS) laboratory. My sincere thanks are also extended to Dr. Andrew Schofield who opened the door for me before I finally obtained a DLS lab key.

Mr. Bobby Hogg and Mr. Rab Kilgour provided valuable advice in making and designing the experimental rigs in the workshop. I would also thank Neil Stewart and Kevin Watson who worked on the project in their MSc and final year study.

This work was funded by the Engineering and Physical Sciences Research Council (EPSRC), UK. This project would not have seen light without Dr. Alistair McLeod's devotion.

Finally, my deepest thoughts go to my parents who, though 5985 miles away from the UK, supported me through these years of hard work.

Table of Contents

List of Figures

List of Tables

Nomenclature

a	Acceleration, $m \cdot s^{-2}$
A	Cross section of the bed, m^2
$A(t)$	A property that depends on the positions and momenta of particles
d_p	Particle diameter, m
D	Internal diameter of riser, m
E_b, $E1$, $E2$, $E3$	Fluidized bed expansions, dimensionless
E_p	Kinetic energy of particle, J
E_0	Scattered field at the detector from a single particle, $v \cdot m^{-1}$
$E(t)$	Superposition of electric fields from N particles, $v \cdot m^{-1}$
f	Frequency of the signal, Hz
g	Gravity acceleration, $m \cdot s^{-2}$
$G_2(t)$	Intensity autocorrelation function, dimensionless
$g_2(t)$	Normalized intensity autocorrelation function, dimensionless
$G_1(t)$	Electrical field autocorrelation function, dimensionless
$g_1(t)$	Normalized electrical field autocorrelation function, dimensionless
h	Bed height, m
h_0	Initial packing height, m
h_m	Measuring height, m
h_{mb}	Bed height at minimum bubbling velocity, m
h_{mf}	Bed height at minimum fluidization velocity, m
I	Intensity of the scattered light, PMT counts/second
k_0	Wavevector, m^{-1}

continue on next page

continue from previous page

L	Thickness of sample, m
l^*	Transport mean free path, m
l_a	Absorption length, m
m	Mass of particle, kg
ΔP	Pressure drop across the bed, $N \cdot m^{-2}$
$\boldsymbol{q}$	Scattering wavevector, m^{-1}
R	Reflection coefficient, dimensionless
Re	Reynolds number, dimensionless
$\boldsymbol{r}_i(t)$	Position of the ith particle.
Δt	Time interval, s
t	Time, s
$T(L)$	Transmission, dimensionless
U	Velocity of particle, $m \cdot s^{-1}$
U_l	Energy density of light, J/m^3
U_{mf}	Minimum fluidization velocity, $m \cdot s^{-1}$
U_{mb}	Minimum bubbling velocity, $m \cdot s^{-1}$
U_s	Superficial gas velocity, $m \cdot s^{-1}$
U_t	Particle terminal velocity, $m \cdot s^{-1}$
v	Particle velocity, $m \cdot s^{-1}$
v_s	Mean velocity component, $m \cdot s^{-1}$
v_s'	Fluctuating velocity component, $m \cdot s^{-1}$
v_n	RMS value of particle fluctuation velocity, $m \cdot s^{-1}$
W	Weight of particles in the bed, kg
Δx	Spacing between the LDA fringes, m
z_0	Penetration length, m

Greek letters

Θ	Granular temperature, $m^2 \cdot s^{-2}$
Θ_w	Granular temperature at the wall, $m^2 \cdot s^{-2}$

continue on next page

continue from previous page

κ	Granular temperature conductivity, $kg \cdot m^{-1} \cdot s^{-1}$
μ_s	Solid viscosity, $N \cdot s \cdot m^{-2}$
μ_g	Gas viscosity, $N \cdot s \cdot m^{-2}$
λ	Wavelength, m
ϕ	Half angle between crossing beams, rad
γ	Penetration coefficient, dimensionless
ε	Bed voidage, dimensionless
ϕ_s	Solid volume fraction, dimensionless
θ	Scattering angle, rad
ρ_s	Solid density, $kg \cdot m^{-3}$
ρ_g	Gas density, $kg \cdot m^{-3}$
β	A constant determined primarily by the collection optics, dimensionless
τ_0	Characteristic diffusion time, s
τ_c	Collision time, s

Chapter 1 Introduction

1.1 Motivation

A *granular material* is a conglomeration of discrete solid, macroscopic particles usually studied in bulk or relative motion. Particle interactions such as collisions are characterized by a loss of energy [1]. Examples of granular materials include nuts, coal, sand, rice, coffee, snow, ball bearings, and all powders. Granular materials are commercially important. They play an important role in many of our industries, such as the chemical industry, pharmaceutical industry, mining, agriculture, construction and energy production.

A *granular material flow* is a form of two-phase flow consisting of particulates and an interstitial fluid. In nature, examples of granular flows include avalanches, river sedimentation, dune formation, planetary ring dynamics, soil liquefaction, and ice flow mechanics. In industry, hoppers, chutes, and conveyor belts are widely used when transporting particulate materials such as foodstuffs, pharmaceuticals, sand and coal. Fluidized beds are frequently used as chemical reactors because they provide excellent heat and mass transfer properties and they are commonly used for chemical reactions involving a solid phase (granules) and a gas (or liquid) phase [2, 3]. Other industrial applications include packing of granular materials, particulate segregation, vibration, mixing and particulate drying, which also takes advantage of the excellent

heat and mass transfer characteristics. Both nature and industry make heavy use of a variety of granular materials covering an extremely broad range of shapes, sizes, micromechanical and chemical properties. The physics of granular materials has received much attention in the science and engineering fields.

Granular materials have flow characteristics that roughly resemble those of ordinary Newtonian fluids. However, granular materials are often inhomogeneous and nonisotropic. A granular material flow usually is a form of two-phase flow consisting of particulates and an interstitial fluid. When sheared the particulates may either flow in a manner similar to a fluid, or resist the shearing like a solid. Their bulk flow characteristics do differ from those of homogeneous fluids in several important ways. The dual nature of these types of flow makes them very difficult to analyze. Granular materials dissipate energy quickly, so techniques of statistical mechanics that assume conservation of energy are of limited use. Currently granular material systems are the subject of intense theoretical interest [4-10]. Understanding the behaviour of granular materials will provide information useful to their wide application and improve the performance of a number of industrial process operations such as fluid catalytic cracking, circulating fluidized bed combustors and pneumatic conveying.

In the field of granular flow, the fluidized bed is one of the most common pieces of equipment in the chemical industry. In a gas-solid fluidized bed, suspended solid particles are strongly agitated by an upward flow of fluid and can be considered to move freely and independently of their neighbours. The behaviour of the solid particles under such conditions is distinct from the quasi-static flows characteristic of solid discharge from hoppers [11, 12] or of particle motion within rotating drums [13-15]. Principally because of its excellent heat transfer characteristics and easy solids handling mobility, gas-solid fluidization probably constitutes the most important chemical industrial application involving gas-solid (granular) flows. A fluidized particulate bed is a common process operation, yet the dynamics of the granular flows in the bed are very complex, and it is difficult to scale-up fluidized bed units due to non-linear behaviour. The ability to improve existing fluidized beds and to design optimal future processes strongly depends on developing a better

understanding of these granular flow systems. In recent years much attention has been devoted to the study of granular flow by both experimental and numerical methods.

Many experimental techniques have been developed in the study of fluidized beds. Several kinds of heat transfer probes are used in the measurement of total heat transfer coefficient in circulating fluidized beds and fluidized bed heat exchangers [16-18]. They can also provide indirect information about the flow of solids inside the fluidized bed. For direct measurement of local solids fluxes, a simple technique, namely the suction probe, is applied [19-21]. A selection of measuring principles and instruments is available for the measurement of local solids volume concentration, its horizontal and vertical distribution and its dependence on operating conditions. These provide extremely useful information on the operation and control of fluidized beds. One of these methods is an optical measurement system which deduces the solid volume information from the reflection or emission of the light. Laser Doppler anemometry (LDA) has been used to determine the velocity of particles if optical access is available [22-25]. In recent years, a laser illumination technique combined with image analysis has been developed to study particle movement in the fluidized bed. Other optical techniques include particle image velocimetry (PIV) [26-29] and several tomography methods [30-32].

As well as experimental work, the fast development of computer hardware has made possible the application of a number of computational fluid dynamics (CFD) techniques to the study of fluidized beds. Numerical simulation models of fluidized beds can be divided into two groups: Lagrangian and Eulerian models. Other simulation methods such as lattice gas cellular automata and statistical mechanics have also been applied to study fluidized bed statistical mechanics [33, 34]. Particle velocity distributions, flow cluster patterns and predicted bubble size and rise velocity in bubbling fluidized beds have been investigated by different CFD models. In Lagrangian models, Newtonian equations of the solid particle motions are solved by the explicit calculation of the forces acting on each of the particles due to particle-particle and particle-fluid interactions [35, 36]. Because of large equipment

dimensions, the great number of the particles and the complex geometry of the fluidized bed, Lagrangian computation is very expensive. The drawbacks of Lagrangian models mean that Eulerian models are so far the only feasible approach for performing parametric investigations, scale-up and design studies. In the Eulerian approach, the solid phase is treated as a continuum, although physically it consists of individual particles[37-39]. Physical models derived from the kinetic theory of granular flow have been widely used in the Eulerian fluidized bed simulation [37, 40, 41]. Central to these models is the so-called ***granular temperature***, representing the ensemble average of squared particle fluctuation velocity. It was first proposed by Ogawa in 1978 [42].

The kinetic energy of particles is proportional to the square of their velocity v. This velocity can be divided into a mean v_s and a fluctuating part v_s'.

$$E_p = \frac{1}{2} m v^2 \tag{1.1}$$

$$v = v_s + v_s' \tag{1.2}$$

Analogous to the thermodynamic temperature for gases, the granular temperature can be introduced to represent the energy associated with the fluctuating velocity of particles. With the assumption of spatial uniformity and isotropy, granular temperature can be formulated as:

$$\Theta \equiv \left\langle v_s' \right\rangle^2 \tag{1.3}$$

Due to a lack of experimental data, the granular temperature predicted from different kinetic models is not well validated. As there are also qualitative and quantitative differences between different kinetic models [43], it is necessary to develop experimental techniques to acquire more experimental data to validate these models under certain geometries and operating conditions.

The aim of this project is to develop an advanced experimental method to study granular flow in the fluidized bed. Investigation of granular temperature by the diffusing-wave spectroscopy technology is of particular interest in this work. These experimental data can be used to validate different simulation models of granular flows.

1.2 Outline of thesis

This thesis presents work using diffusing-wave spectroscopy, a non-intrusive technique, to study the granular temperature in the gas-solid fluidized bed experimentally. This thesis is organised as follows.

Chapter 2 presents a general introduction of granular temperature measurement methods. Several intrusive and non-intrusive experimental methods are overviewed. Their advantages and disadvantages are compared.

The next chapter presents a general introduction to dynamic light scattering theory. A general overview of the theoretical fundamentals of multiple light scattering is presented. Based on two fundamental approximations, diffusing-wave spectroscopy theory and its experimental configurations are introduced. After a four-step data analysis process, particle granular temperature in the fluidized bed can be derived straightforwardly from the diffusing light intensity autocorrelation function.

Chapter 4 starts with a brief introduction to gas-solid fluidization and the Geldart particle classification. The two dimensional fluidized beds and particulate materials used in the experiment are described. The particles used in this study exhibited excellent fluidization characteristics although they belong to Geldart's group C, usually associated with cohesive behaviour and difficult fluidization behaviour. Small channel flows, smooth fluidization and bubbling fluidization are shown successively as gas superficial velocity is increased. The bed remains homogeneous and expands smoothly above the minimum fluidization velocity (U_{mf}) - this provides good measurement conditions for diffusing-wave spectroscopy. Bed expansion,

pressure drop across the bed, minimum fluidization velocity and minimum bubbling velocity (U_{mb}) are studied. Both measured velocity results agree well with their predicted values.

Chapter 5 deals with a parametric study of the diffusing-wave spectroscopy technique. Firstly the transmitted light intensity profile measurement method is introduced. By measuring the total transmission of scattering light, two important quantities in the analysis of diffusing-wave spectroscopy, transport mean free path l^* and absorption length l_a, can be determined quantitatively. The effect on both these quantities of the penetration coefficient γ and reflection coefficient R is discussed. Several factors in the DWS experiment, including transmission and backscattering measuring geometry, detector positions, laser power and polarization effect, are discussed in this chapter.

Chapter 6 presents granular temperature measurement results in the fluidized bed of Q-Cel5020 particles. Granular temperature variations at a fixed position under different gas superficial velocities and granular temperature variations at varying vertical and horizontal positions under fixed gas velocity are studied. Granular temperature results from transmission and backscattering geometries are compared. We find non-zero granular temperature before minimum bubbling velocity, which was not observed by previous researchers who used the same technique study solid glass beads fluidization [44]. We report for the first time to our knowledge, the variation of velocity fluctuations with position in the fluidized bed. Preliminary measurements on a laboratory scale circulating fluidized bed are reported. Granular temperature at riser and downcomer are investigated.

Finally, Chapter 7 summarizes the work undertaken through the thesis and future work is proposed.

Chapter 2 Overview of granular temperature measurement methods

A successful approach toward the understanding of granular flows requires reliable experimental data. There are several methods used in industry and academic research to study granular flow properties such as solid volume concentration, solid velocities, solid mass flows, granular flow patterns and vertical and horizontal distribution of solid. Some techniques that are applied in measuring flow properties in fluidized bed systems have already been widely used in routine industrial measurements. On the other hand, some techniques have limited application and have only been used in academic research so far. A number of methods have been used over the past 15 years to measure the granular temperature for a variety of systems. The methods used to study granular flows can be divided into two groups: intrusive methods and non-intrusive methods. The first attempts were made at Caltech, where fibre optic probes were used to measure streamwise velocity fluctuations in 3D chute flows [45, 46]. The non-intrusive techniques, which determine properties inside gas-solid flows by means of instruments located outside, are highly desirable because these measurements do not interfere with the granular flow. As this work is primarily focused on experimental study of fluidized beds to collect experimental data for future validation of CFD models and, in particular, the velocity fluctuation (granular temperature) in the first instance, non-intrusive methods for the determination of granular velocities are reviewed here. Subsequently we focus on the experimental

method of measuring the granular velocity and its fluctuation in a flow by non-intrusive techniques.

2.1 Laser-Doppler anemometry

Laser-Doppler anemometry (LDA) is widely used in particle velocity measurement. There are several different configurations for LDA [47], depending on the properties and accessibility of the flow. A diagram of a simple LDA set-up is shown below.

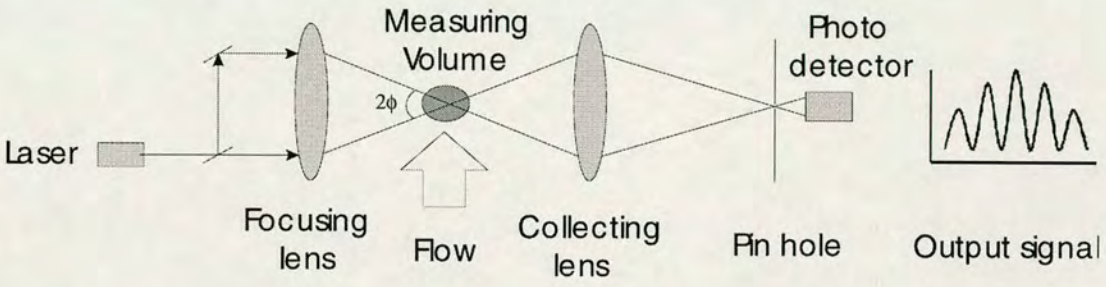

Figure 2.1 A Laser-Doppler anemometry set-up

The laser beam is first split into two parallel beams of equal intensity. Then these two beams are passed through a converging lens so that they cross at the focal point of the lens. The point where the two beams cross is the measuring volume, which might best be described as an ellipsoid. The interference of the two beams generates a series of light and dark fringes in the measuring volume perpendicular to the plane of the two beams. As a particle passes through the fringe pattern, light is scattered and a portion of the scattered light passes through the collecting lens towards the photodetector. A typical signal obtained from the photo-detector is shown in Figure 2.1.

It can be shown from optical theory that the spacing between the fringes is given by

$$\Delta x = \frac{\lambda}{2\sin\phi} \tag{2.1}$$

where λ is the length of the laser beam and ϕ is the half-angle between the crossing beams. By suitable electronic circuitry, the frequency of the signal f is measured, so the velocity is given by

$$U = \frac{\Delta x}{\Delta t} = \frac{\lambda f}{2\sin\phi} \tag{2.2}$$

where f is the frequency of the signal. The operation of LDA depends on the presence of particles in the flow to scatter the light. In liquid flows, the impurities of the fluid typically serve as scattering centres. In gaseous flows, it is sometimes necessary to 'seed' the flow with small particles.

Many researchers have used LDA to study granular flow. It has been used to measure particle concentration in high-temperature particle-laden flows by Kim et al. [48]. LDA was applied in measuring not only velocity but also fluctuating velocity and size distribution in the riser of a circulating fluidized bed by Zhang et al. [49]. Samuelsberg et al. [50] combined the LDA technique and phase Doppler anemometry to measure mean and root mean square (RMS) particle velocities for three different superficial gas velocities. The fluctuating velocity component was also studied. Using laser-beam pairs of different colours (wavelength), LDA has recently been used to provide two or three velocity components of a particle by Ibsen et al. [51].

As a non-intrusive method, the major advantage of LDA is that the flow field is not disturbed by the presence of a probe or wire support. A further advantage is that the velocity is measured in a very small flow volume, providing excellent spatial resolution. The main disadvantages of LDA is, in higher concentrated fluid-solid flows, the laser light may not be able to pass through the more or less opaque layer of particles on its way from the probe to the particles and back. This leads to a severe reduction in the rate of which valid data may be obtained [52].

2.2 Positron emission particle tracking

Positron emission particle tracking (PEPT) is a technique that allows non-invasive observation of the motion of a single radioactive tracer particle. It allows the flow path of a tracer particle to be followed in opaque flows. PEPT has been used to study particle trajectories and velocity profiles of a single radioactively labelled tracer particle in high solid fraction. It is schematically represented in Figure 2.2.

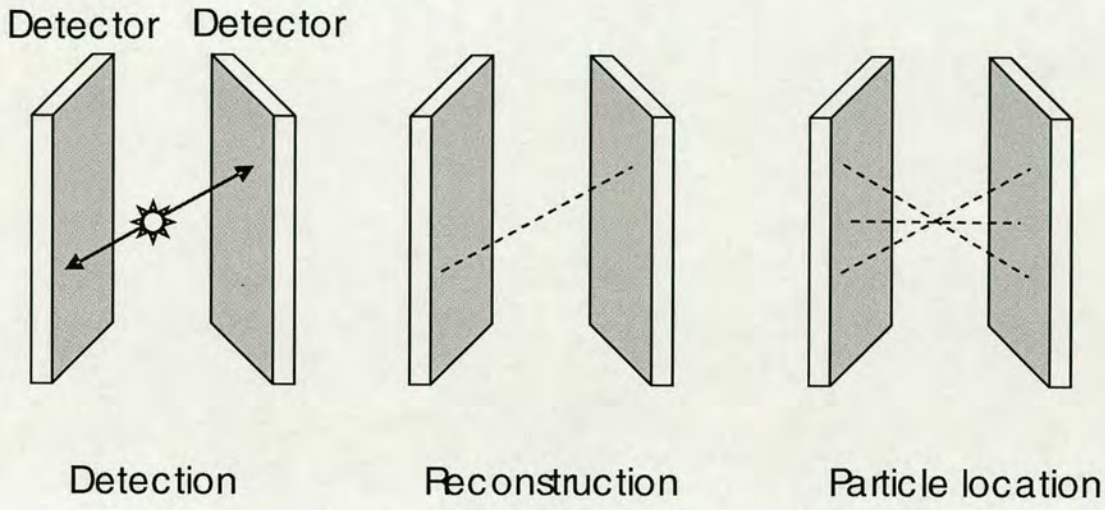

Figure 2.2 The principle of the PEPT technique

For example, a glass particle was irradiated with the ^{3}He beam from a cyclotron to produce the positron emitter ^{18}F from reactions involving the oxygen content of the glass. The decay of the ^{18}F isotope features the conversion of a proton to a neutron with the emission of a positron, the anti-particle of the electron. The positron then annihilates with an electron to produce a pair of back-to-back γ-rays. The γ-rays are detected by the positron camera, which consists of two position-sensitive γ-ray detectors. By using a reconstruction algorithm the position of the particle can be obtained as the intersection point of successive annihilation vectors. The algorithm employs an iterative scheme to discard corrupt annihilation vectors that can be caused by γ-ray scattering or random coincidences.

PEPT is applied to analyse non-intrusively solids flow on a laboratory scale. Granular temperature profiles in three-dimensional vibrofluidized granular beds were studied by Wildman et al.[53, 54]. The mean square fluctuation velocity about the mean was calculated through analysis of the short time mean squared displacement behaviour. This technique allows measurement of the granular temperature at packing fractions of up to 0.15. Wildman et al. also investigated the granular temperature distributions of a binary vibrofluidized granular bed [55, 56]. They found that the binary system, though supporting two separate granular temperature profiles, responds to changes in vibration velocity in a very similar fashion to a monosized granular bed.

Unlike conventional techniques which are restricted to measuring the flow at the surface or a transparent wall, PEPT reveals the motion of material throughout the entire bed [57]. When the tracer particle is stationary the more annihilation vectors are used the more accurately the particle position can be determined. However, when the particle is moving the set of annihilation vectors should be large enough to locate the particle accurately but not so large that it has moved significantly during the time period over which the set was measured. To extract not only the Eulerian ensemble average velocity field, but also to reconstruct density profiles and to calculate mass flows in a solids circulation system, a very high performance tracking system is needed.

2.3 Acoustic shot noise probe

Acoustic shot noise (ASN) is a non-intrusive probe of average granular temperature at the wall of fluidized beds. It is based on a quantitative analysis of the response of the wall of a vessel to random particle impact. Cody et al. utilized power spectral analysis for the derivation, in particular the fundamental theorem of Wiener and Khintchine which states that, for stationary random functions, the power spectrum of a random function is the Fourier transform of its autocorrelation function [58]. The average particle granular temperature can be obtained through independent measurement of the wall transfer function determining the coupling between the

acoustic shot noise excitation at one location and the response of an accelerometer at another. Quantitative information on the particle granular temperature is obtained by converting a vibration signal at the wall of the bed.

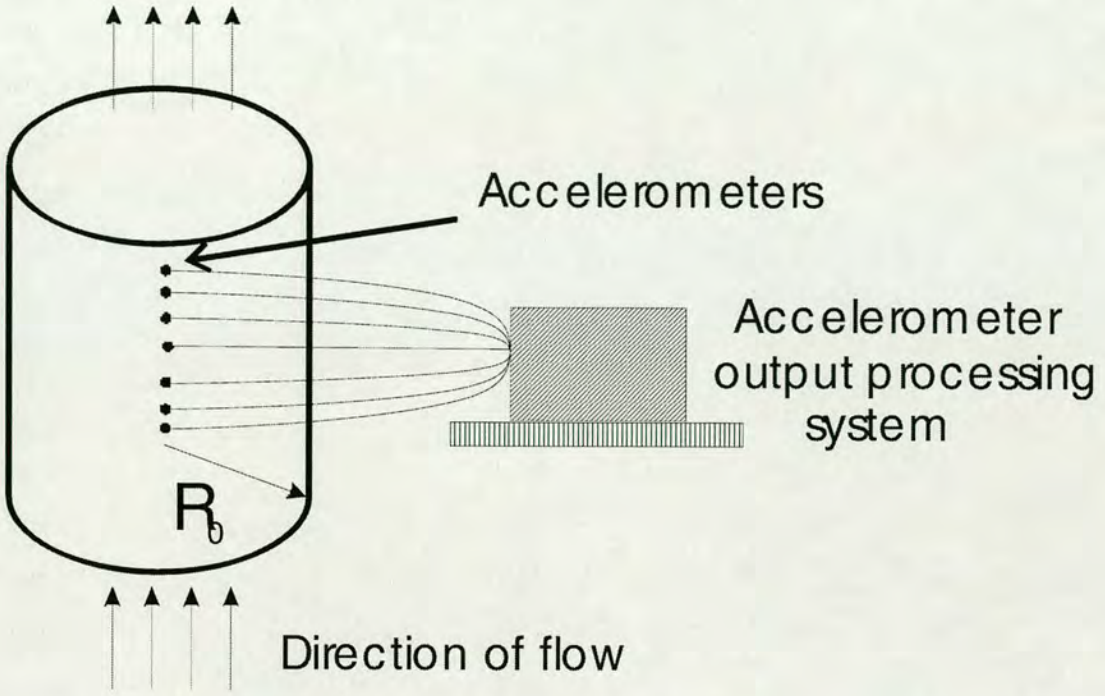

Figure 2.3 ASN probe to measure particle RMS acceleration near the wall.

Cody et al. [59], using the acoustic shot noise probe technique, measured RMS accelerations of mono-disperse particles at the wall of a gas fluidized bed. They observed differences in the dependence of the granular temperature on gas flow between Geldart B and A glass spheres and suggested a fundamental difference in particle dynamics between spheres in the two Geldart regimes. Time-dependence of the granular temperature under bed collapse was also studied. Furthermore, the acoustic shot noise probe was used to study particle motion and gas generation in the feed injection zone of the feed riser of a fluidized bed catalytic cracking unit [60]. The measurement of the ASN probe method is limited to the region near the wall of the fluidized bed because the probes can be mounted only at the wall.

2.4 Image analysis methods

Computer analysis of high speed video images is one of the most widely used non-intrusive methods in the study of granular flow. A number of teams have also used

this approach to study a variety of 2D vibro-fluidised systems [61-64]. Wildman et al. used high speed photography, image analysis and particle tracking software to determine accurate location of 5mm steel balls in a vibro-fluidized bed [62]. High speed photography, image analysis, and particle tracking software enabled accurate location of the grains. Appropriate analysis of the three mean squared displacement regimes allowed both the diffusion coefficient and the granular temperature to be measured at the same packing fraction.

Workers have used this approach to study strictly-2D chute and shear cell [65, 66] configurations where flows are dominated by long-term frictional contact between particles and, in the former, wall interactions. Drake et al. studied two dimensional flows of 6mm diameter plastic spheres in an inclined glass-walled chute by high speed camera [67]. Profiles of mean downstream velocity, velocity fluctuation, mean rotations, rotational temperature and bulk density in the flows were acquired by high-speed motion pictures. Measurements of two components of the average and fluctuating velocities in a flow of granular material in a 1 m high vertical channel with roughened sidewalls and with polished glass plates at the front and the back were performed by Natarajan et al. [68]. The particles used were glass spheres with a nominal diameter of 3 mm.

With the development of a high resolution measuring system, the image analysis method was used to study much smaller granules such as the granular temperature of FCC catalysts (diameter: 75 μm) in a circulating fluidized bed [69].

In recent years, significant progress has been made in the development of tomography and radiography methods. γ-ray and X-ray transmission tomography, X-ray radiography, neutron transmission tomography and radiography, positron emission tomography, X-ray diffraction tomography, nuclear magnetic resonance imaging, electrical capacitance tomography and ultrasonic tomography, which are widely used in medical research, are also used in the study of gas-solid flows in fluidized beds [70-75]. The primary disadvantage of these methods is low-resolution images in the interpretation and quantification of experiment data.

Based on light scattering technology, diffusing wave spectroscopy (DWS) has been applied in the study of micro-dynamics of colloid particles [76], gravity driven sands [77] and fluidized beds [44]. The DWS method is more attractive than other non-intrusive methods in that it can in principle detect motion at extremely short length (0.01-1 μm) and time scales (10^{-6} to 10^{-4} s). More details of this technique will be discussed in Chapter 3 and Chapter 5.

Non-invasive measurement techniques determine properties of gas-solid flow inside the fluidized bed by means of instruments located outside. They are highly desirable because these measurements do not interfere with the granular flows of research interest. In the development of such methods, however, it has to be taken into account that industrial applications of fluidized beds are typically very large reactors. For example, the fluidized bed reactors used in the chemical industry commonly have diameter between 3 and 5 m with heights ranging from 5 to 15 m. These dimensions are a big challenge for almost all non-invasive measurement techniques. It is not surprising therefore that the application of the above techniques is presently restricted to academic investigations of very small dimensioned fluidized beds compared with industrial operating units.

Although there are limitations to the employment of some of the above non-intrusive measurement methods in industry, they are still very important in the study of small scale systems in academic research and allow fundamental study of various objects under different conditions to validate granular flow theory and models.

2.5 Previous granular temperature studies

For chute flows, studies suggest the granular temperature increases with bulk velocity and decreases as the solid volume fraction increases from 10 to 40% [45, 46]. These studies also indicate that the nature of any solid surfaces and the coefficient of restitution may affect the variation of the granular temperature in the chute.

A small number of studies have focused on gas fluidized beds, which are of particular interest here. Gidaspow and Huilin [69, 78] used video image analysis to study fluidised cracking catalyst (FCC) in a large-scale gas circulating fluidised bed, where the superficial velocity, U_s, is greater than the terminal velocity of the particles leading to a fast moving dilute bed. The conclusions of these workers are very much in line with the results obtained for the dilute vibro-fluidized bed in respect of the variation of granular temperature with solids loading. High solids loadings, high speeds and the smallness of the particles means video, PEPT and NMR methods are not well suited to non-circulating fluidised beds. Cody *et al.* [59] found the granular temperature increased rapidly from zero beyond the minimum fluidization velocity, U_{mf}, before transitioning to a slower rate of increase at $1.5-2.5U_{mf}$, with the rate varying with particle type. Menon and Durian [77] observed behaviour similar to that of Cody *et al.* except in what appears to be one critical respect – they did not detect a granular temperature below the minimum bubbling velocity, U_{mb}. This absence of a granular temperature until the onset of bubbling prompted these workers to conclude that uniformly fluidization is a static network of particles – in effect, a solid. It is not entirely clear why the findings of these workers are at odds with those of Cody *et al.* in this regard, but it could be linked to the small differences between the minimum fluidisation and bubbling velocities and associated bed heights for the systems they investigated. Valverde *et al.* [79] attempted to resolve this conflict by using a bed of 8.5 μm toner particles whose minimum bubbling velocity and associated bed height are much greater than at the onset of bubbling. They determined the granular temperature by fitting a diffusion model to particle colour concentration data, transverse to the flow direction, for a non-circulating fluidized bed that initially contained equal masses of particles of two different colours, separated into the left and right halves of the bed respectively. Their results led them to propose the existence of two different regimes for uniform fluidised beds. In the first, located in the range of $U_{mf} < U_s < U_c$ with $U_c << U_{mb}$, the bed is solid-like, whilst in the second, located beyond U_c, the bed is fluid-like and the granular temperature is non-zero. This finding leads these workers to claim their results provide support for the conclusions of both Cody *et al.* and Menon and

Durian. It is, however, difficult to see how the latter would have observed the first of these two regimes given it would have occupied only a fraction of what was already a small velocity range between incipient fluidization and onset of bubbling.

Chapter 3 Diffusing-wave spectroscopy technique and data analysis

3.1 Introduction

3.1.1 Dynamic light scattering

Dynamic light scattering (DLS), which is also known as photon correlation spectroscopy or quasi-elastic light scattering (QELS), studies the time behaviour of fluctuations in the scattered light intensity. The technique of dynamic light scattering has been established as a powerful method for investigating dynamic processes since it is based on the scattering of light by moving particles. By measuring the temporal fluctuations of the scattered light, one can extract detailed information about the dynamics of the scattering medium.

According to classical light scattering theory [80-82], when light impinges on the object studied (usually an optically transparent sample), the electric field of the light induces an oscillating polarization of electrons in the molecules. Hence the molecules provide a secondary source of light and subsequently scatter light. The frequency shift, the angular distribution, the polarization, and the intensity of the scattered light are determined by the size, shape and molecular interactions in the scattering material.

Different methods can be used to study the dynamics of a system with particles in Brownian motion, depending on the time scale of the molecular fluctuations. Figure 3.1 is a simple dynamic light scattering experiment set-up. Several configurations can be used in various situations, as shown in Figure 3.2.

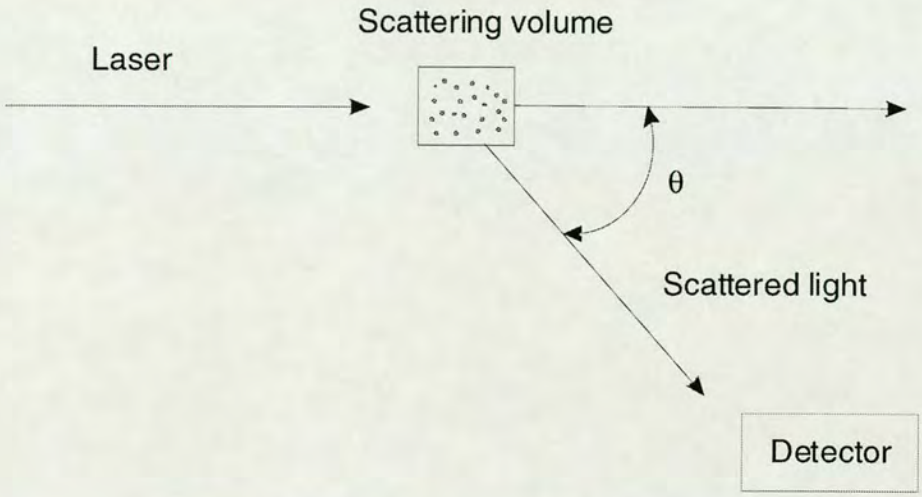

Figure 3.1 Dynamic light scattering experiment

Suppose DLS is used in the study of a monodisperse suspension of non-interacting spheres (i.e. dilute latex systems). Laser light with an incident wavevector, $\boldsymbol{k}_0$, illuminates the sample and is scattered no more than once before passing through the sample if the concentration of particles is dilute enough.

Light that is scattered through an angle θ with a wavevector $\boldsymbol{k}_s$ is then detected in the far field. If the scattered field at the detector from a single particle is E_0, then the total field E is the superposition of scattered fields from all N particles in the scattering volume:

$$E(t) = \sum_{i=1}^{N} E_0 \exp[i\boldsymbol{q}\cdot\boldsymbol{r}_i(t)] \qquad (3.1)$$

where $\boldsymbol{q}$ is the scattering wavevector defined by $\boldsymbol{q} = \boldsymbol{k}_s - \boldsymbol{k}_0$, and $\boldsymbol{r}_i(t)$ is the position of the *i*th particle. The argument of the exponential represents the phase shift introduced by scattering and depends on the position of each particle in the scattering volume.

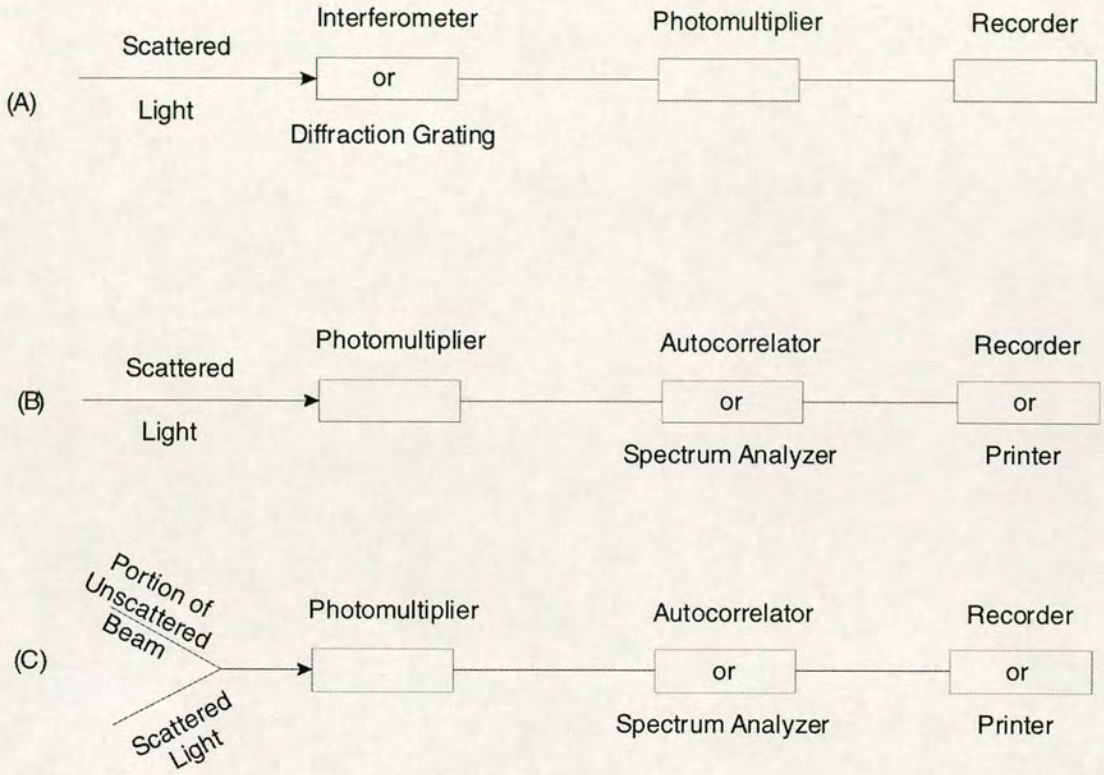

Figure 3.2 Various techniques used in the DLS experiments [81]

(A) filter methods; (B) homodyne; (C) heterodyne.

As the particles in the scattering volume move, the phase of the scattered field from each particle changes, causing the scattered intensity to fluctuate with time. Thus, the rate at which the intensity fluctuates is directly determined by the motion of the particles. These fluctuations can be characterized by their temporal autocorrelation function [81],

$$g_2(t)=\frac{1}{\beta}\left(\frac{\langle I(t)I(0)\rangle}{\langle I\rangle^2}-1\right)=\left(\frac{E(0)E(t)}{\langle|E|^2\rangle}\right)^2=|g_1(t)|^2 \tag{3.2}$$

where β is a constant determined primarily by the collection optics of the experiment, I is intensity of scattered light. The second equality in Eqn.(3.2) holds in many cases of experimental interest and is known as the Siegert relation. In general, the electric field autocorrelation function is given by

$$g_1(t)=\frac{\sum_{i=1}^{N}\sum_{j=1}^{N}\left\langle\exp\left\{i\boldsymbol{q}\cdot\left[\boldsymbol{r}_i(0)-\boldsymbol{r}_j(t)\right]\right\}\right\rangle}{\sum_{i=1}^{N}\sum_{j=1}^{N}\left\langle\exp\left\{i\boldsymbol{q}\cdot\left[\boldsymbol{r}_i(0)-\boldsymbol{r}_j(0)\right]\right\}\right\rangle} \tag{3.3}$$

For the case of non-interacting uncorrelated particles, the cross-terms $i \neq j$ vanishes to give

$$g_1(t)=\left\langle\exp\left[-i\boldsymbol{q}\cdot\Delta\boldsymbol{r}(t)\right]\right\rangle \tag{3.4}$$

where $\Delta\boldsymbol{r}(t)\equiv\boldsymbol{r}(t)-\boldsymbol{r}(0)$. Thus $g_1(t)$ decays appreciably when $\boldsymbol{q}\cdot\Delta\boldsymbol{r}(t)\cong\pi$, or, equivalently, when $\Delta r\approx\lambda$.

Originally dynamic light scattering applications were limited to weakly scattering media for which the light propagation could be described by a single-scattering model. The dynamic light scattering technique was successfully applied to study Taylor-Couette flow, vesicle-like droplets, rheology of complex fluids and granular fluidization [83-86]. It is one of the most popular methods to determine the size of particles [87].

3.1.2 Multiple light scattering

Dynamic light scattering requires that the concentration of scatterers be sufficiently dilute that the incident light is scattered only once by the sample. This means that most samples must be diluted to the point where they are optically almost clear. If multiple scattering occurs then multiple phase shifts of the scattered light occur with the result that the theory of the standard DLS method will no longer apply. The

traditional DLS technique cannot be applied to study optically opaque samples such as concentrated suspensions. However, a related form of laser light scattering, called diffusing-wave spectroscopy (DWS) is available and provides estimates of particle micro-dynamics.

3.2 Diffusing-wave spectroscopy

An important breakthrough in the field of dynamic light scattering is the extension of DLS to multiply scattering media. This technique is referred to as diffusing-wave spectroscopy (DWS) [88]. DWS extends the analytic power of DLS to very dense scattering media and opaque samples such as concentrated suspensions and colloidal systems, nematic liquid crystals, foams and flowing sands [89-94]. It is a very sensitive technique that yields two particle correlation functions at time intervals greater than 10^{-8} s and spatial separations greater than 1 Å. It has already widely been used to study homogeneous colloidal systems. A study of flowing sand was made using DWS by Menon et al [77]. They also used DWS to study a gas-solid fluidized bed [44].

The basic approximation is that light propagation through the very highly scattering medium is treated as a diffusive process [95]. This approximation neglects the interference effects of the light as it propagates through the scattering medium, and assumes that the light intensity undergoes a process of diffusion. This neglect of interference effects within the medium is predicated on the assumption that the light scattering is not so strong as to approach the localization of light due to random scattering. The scattering medium behaves as an insulator when the light reaches to a localized state. However, very little localization of light, and only under certain specific conditions, has been observed until recently [96, 97]. In fact it is the experimental observation that the strong localization of light is so difficult to achieve that gives the diffusion approximation its wide applicability. It is an excellent approximation in practice. Also, the use of the diffusion approximation makes it possible to calculate the distribution of paths taken by the photons propagating through the medium.

The second approximation in DWS is that the individual scattering events are approximated by the combination of a repeated average scattering event. Since each photon is scattered a large number of times as it is transported through the sample, the details of individual scattering events play a less critical role. In DWS, a change in the total path length by one wavelength is caused by the cumulative motion of a very large number of scatterers. Thus each scatterer need move only a small fraction of a wavelength. Therefore, using DWS it is possible to measure the motion of micrometer-sized particles on length scales as small as a few angstroms (Å).

3.2.1 Fluctuations and time-correlation functions

Time-dependent correlation functions have been familiar for a long time in the theory of noise and stochastic processes. They have become very useful in many areas of statistical physics and spectroscopy. Correlation functions provide a concise method for expressing the degree to which two dynamical properties are correlated over a period of time [81].

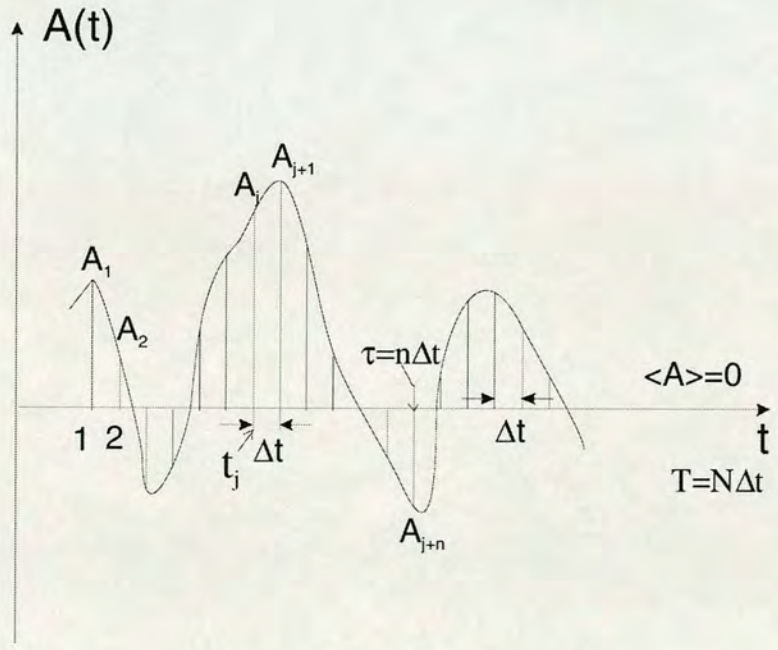

Figure 3.3 The property A(t) fluctuates in time as the scatterers move around in the fluid. The time axis is divided into discrete intervals, Δt, and the time average <A> is assumed to be zero for convenience.

Consider a property A(t) that depends on the positions and momenta of all the particles in the system. The time-dependence of the property A(t) will generally resemble a noise pattern. In Figure 3.3, we see that property A fluctuates about its time average, which can be expressed as

$$\langle A \rangle = \lim_{T\to\infty} \frac{1}{T} \int_0^T A(t)\,dt \tag{3.5}$$

When τ is very small, the property A(t+ τ) will be very close to A(t). As τ increases the deviation of A(t+ τ) from A(t) is more likely to be nonzero. Thus we can say that the value A(t+ τ) is correlated with A(t) when τ is very small but this correlation is lost as τ becomes large compared with the period of fluctuations. A measure of this correlation is the autocorrelation function of the property A which is defined by

$$\langle A(0)A(\tau)\rangle = \lim_{T\to\infty} \frac{1}{T} \int_0^T A(t)A(t+\tau)dt \tag{3.6}$$

Using Schwartz's inequality, according to which

$$\left|\sum_j A_j B_j\right|^2 \le \left|\sum_j A_j^2\right|\left|\sum_j B_j^2\right| \tag{3.7}$$

If we take $B_j = A_{j+n}$, divide both sides by N^2, take the limit $N \to \infty$ and recognize that:

$$\lim_{N\to\infty} \frac{1}{N} \sum_{j=1}^{N} A_j^2 = \langle A^2 \rangle \tag{3.8}$$

$$\lim_{N\to\infty} \frac{1}{N} \sum_{j=1}^{N} A_{j+n}^2 = \langle A^2 \rangle \tag{3.9}$$

$$\lim_{N\to\infty} \frac{1}{N} \sum_{j=1}^{N} A_j A_{j+n} = \langle A(0)A(\tau)\rangle \tag{3.10}$$

it follows that

$$\left|\langle A(0)A(\tau)\rangle\right|^2 \le \langle A^2 \rangle^2 \tag{3.11}$$

Since $\langle A(0)A(\tau)\rangle$ is real, the inequality

$$\langle A(0)A(\tau)\rangle \leq \langle A^2\rangle \tag{3.12}$$

is true. For times τ large compared to the characteristic time for fluctuation of A, A(t) and A(t+ τ) are expected to become totally uncorrelated, thus

$$\lim_{\tau\to\infty}\langle A(0)A(\tau)\rangle = \langle A(0)\rangle\langle A(\tau)\rangle = \langle A\rangle^2 \tag{3.13}$$

so that the time-correlation function of a nonperiodic property decays from $\langle A^2\rangle$ to $\langle A\rangle^2$ in the course of time [81]. This is shown in Figure 3.4. The normalized autocorrelation function will range from $\frac{\langle A^2\rangle}{\langle A\rangle^2}$ to 1. In the experiment we measured scattered light intensity and its fluctuations. Time-dependent light intensity autocorrelation functions were calculated. We found that the $\frac{\langle A^2\rangle}{\langle A\rangle^2}$ value of the normalized light intensity autocorrelation function varied from 1.85 to 1.40.

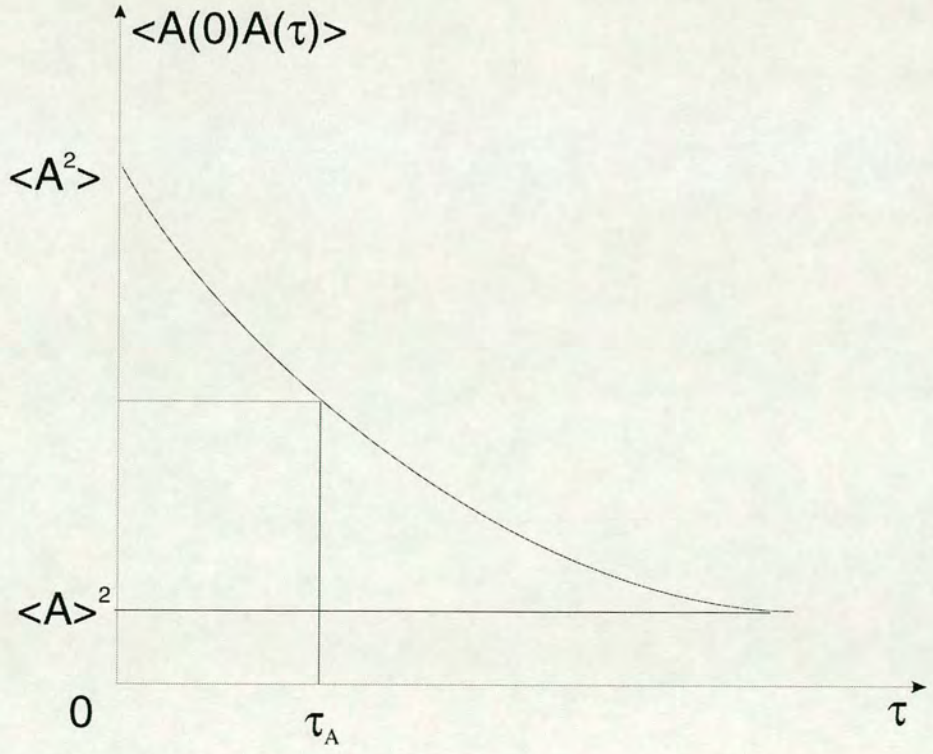

Figure 3.4 Time autocorrelation function, <A(0)A(τ)>. Initially this function is <A^2>. For times very long compared to the correlation time, τ_A, it decays to <A>^{2}.

In the light scattering experiment, the light intensity autocorrelation function and the electrical field autocorrelation are the two most relevant autocorrelations of interest. The light intensity autocorrelation can be measured by optical instrumentation, then converted to the electrical field autocorrelation, which is difficult to measure experimentally.

In the experiments, the scattered light intensity autocorrelation function was measured.

$$G_2(t) = \frac{I(0)I(t)}{\langle I \rangle^2} \tag{3.14}$$

which fulfils $G_2(0) = 1$

The normalized intensity autocorrelation is

$$g_2(t) = \frac{G_2(t) - 1}{\beta} \tag{3.15}$$

The electric field autocorrelation can then be acquired from the Siegert relation Equation (3.2).

3.2.2 DWS theory

The intensity fluctuations measured with DWS arise when the pathlength of the scattered light changes by one wavelength, just as they do in the traditional DLS. In the case of DWS, however, a change in the total path length by one wavelength is caused by the cumulative motion of a very large number of scatterers when multiple scattering happens.

The autocorrelation function of the scattered field is

$$g_1(t) = \frac{\int_{l^*}^{\infty} p(s) e^{-\frac{s}{l^*}\langle \delta\phi^2(t) \rangle} ds}{\int_{l^*}^{\infty} p(s) ds} \tag{3.16}$$

where $\langle \delta\phi^2(t) \rangle$ is the mean square phase shift per scattering event and $p(s)$ is a quantity that is determined by the fraction of scattered intensity in paths of length s. It depends on sample geometry, size and l^*.

The transport of light is described by the diffusion equation

$$\frac{\partial U_l}{\partial t} = D_l \nabla^2 U_l \tag{3.17}$$

where U_l is the energy density of light (or number of photons per unit volume) in the sample, and D_l is the diffusion coefficient of light.

To calculated $p(s)$, how much light intensity is scattered on average into paths of length s, an instantaneous laser pulse is assumed as the light source and the light is randomized within the sample over a distance comparable with l^*. If we describe the incident light pulse as an instantaneous source of diffusing light at distance $z_0 \approx l^*$ inside the sample, the initial condition is

$$U_l(z, t=0) = U_{l0}\delta(z - z_0, t) \tag{3.18}$$

The boundary condition, equation (3.19), can be obtained by requiring that for t>0 the net flux of diffusing light into the sample is zero

$$U_l + \frac{2}{3} l^* \hat{\boldsymbol{n}} \cdot \nabla U_l = 0 \tag{3.19}$$

With Laplace transform used, equation (3.20) can be obtained.

$$g_1(t) = \frac{\overline{U_l}(r, p)\Big|_{r_{out}}}{\overline{U_l}(r, 0)\Big|_{r_{out}}} \tag{3.20}$$

Combining with the different boundary and initial conditions in the experiments, explicit expressions for corresponding $g_1(t)$ have been worked out for various

geometries, such as backscattering and transmission from slabs, pairs of optical fibres dipping into a turbid sample and some other situations.

3.2.3 DWS Set-up

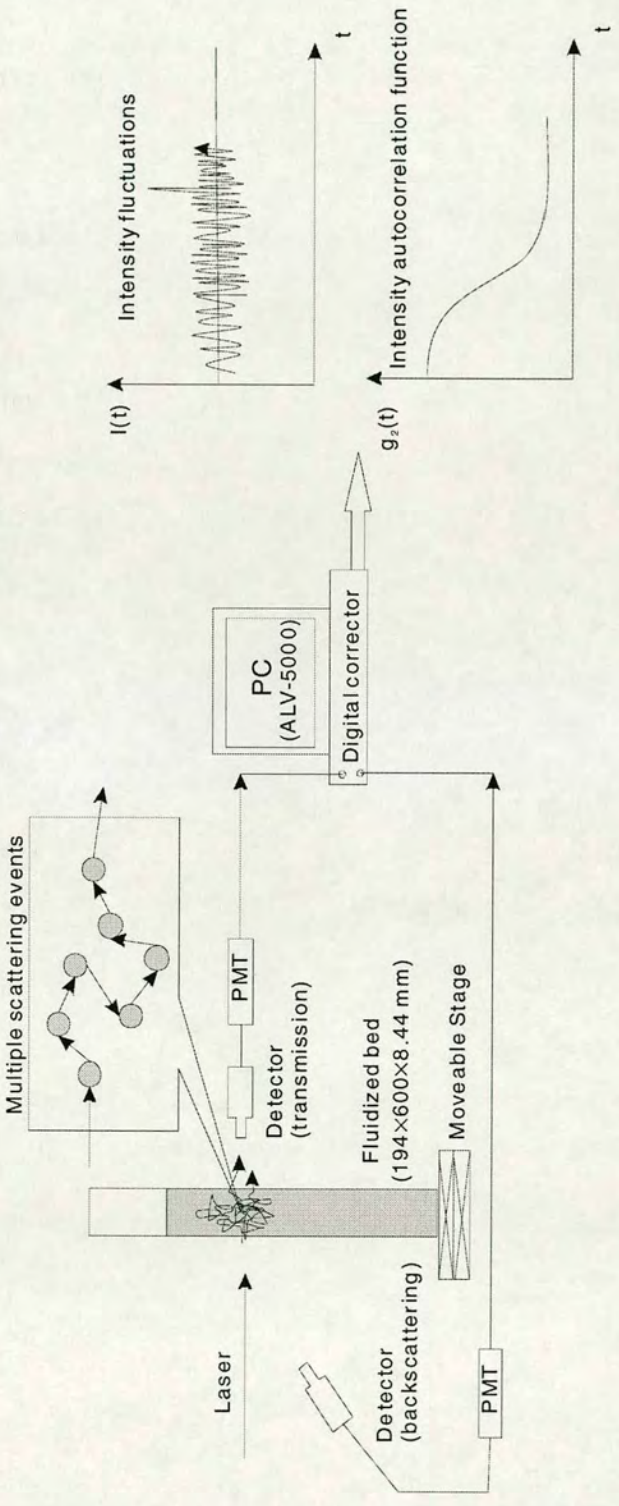

Figure 3.4 Using DWS to study a Fluidized Bed.

An incident monomode laser beam travels inside the sample (a fluidized bed in our experiments) along the various random scattering paths described by the photon random walk, and sets up a highly irregular intensity pattern called 'speckle', as a result of interference between many waves from many paths of various lengths, at the other side of the sample. The detector, which is an optical fibre connected to a photomultiplier tube, receives the multiply scattered photons. The signals are magnified and sent to the digital correlator ALV-5000E. The intensity in a given speckle spot fluctuates when the particles in the fluidized bed move with respect to each other. Due to motion of the scatterers (particles in the multiple light scattering region), the time-dependent phase shift of the scattered optical field accumulates along the paths and gives rise to speckle fluctuations on a path-length dependent time scale. The intensity and its autocorrelation functions data are calculated simultaneously and then saved in the computer to be analysed. In our experiment, the correlation time interval is 2×10^{-7} second when single channel (transmission or backscattering geometry) used. When dual channels are used simultaneously to collect signals from both geometries, the correlation time interval will be 4×10^{-7} second.

3.3 DWS data analysis

3.3.1 Data Transform

In the DWS experiment, the data (intensity and its autocorrelation function) are collected by an ALV-5000 multiple Tau digital correlator. The correlator does not provide any 'raw data output'. In order to obtain data that can be analysed by other software, a special program called ALV Transformer (AT) is used. AT can change the format of the experimental files from ASCII to binary or from binary to ASCII. A more useful function is that AT can extract pure values of the autocorrelation function and save them with corresponding retardation times as readable files which can be imported to other data processing programs (e.g. Origin, MS Excel, et al).

Intensity autocorrelation functions $G_2(t)$ from transmission and backscattering geometry measurements in one experiment can be acquired from AT by selecting different channels (0 or 1). They are exported to two different files although their original data are stored in one file by ALV-5000.

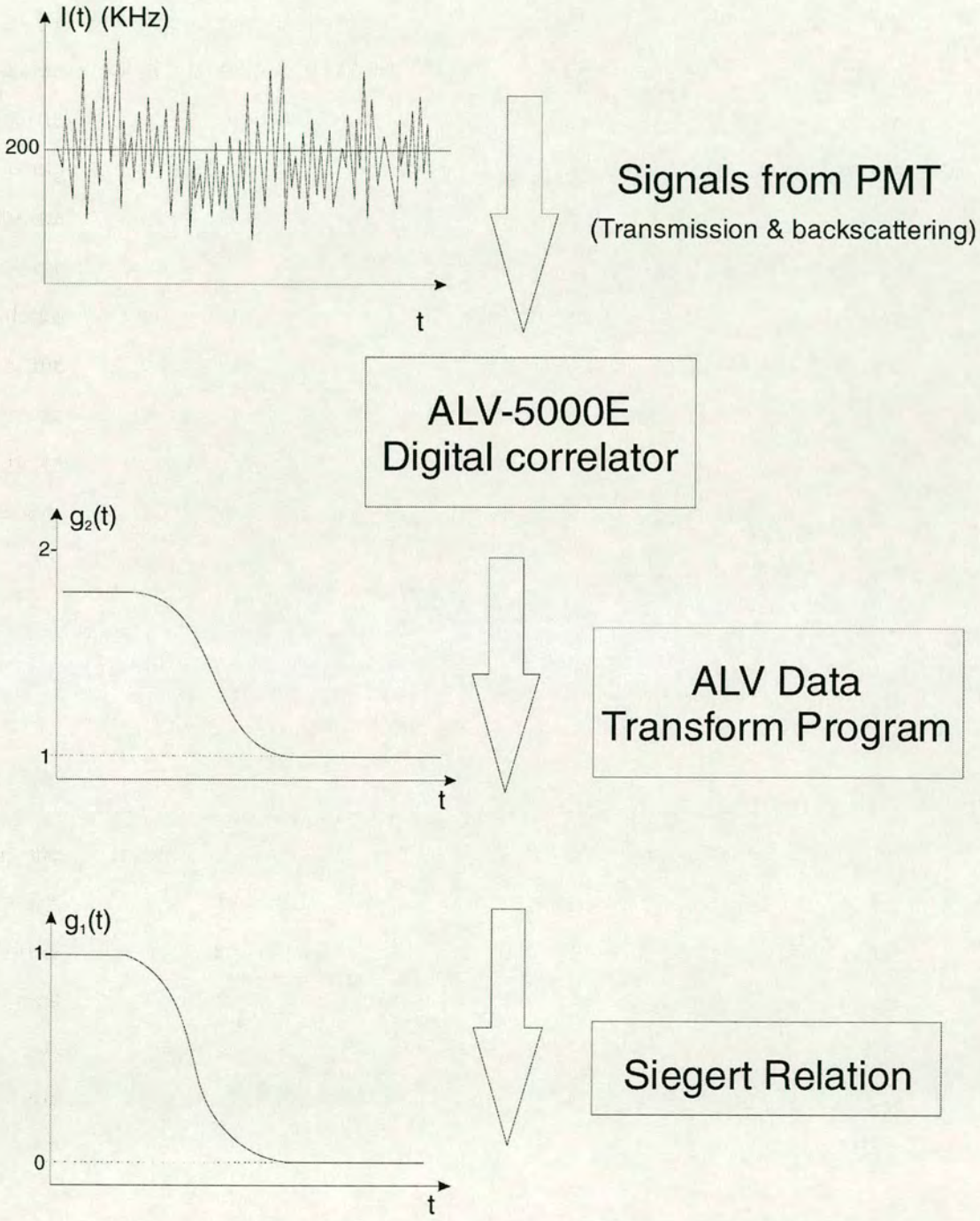

Figure 3.5 DWS experimental data analysis

3.3.2 From $g_2(t)$ to $g_1(t)$

Equation (3.2) is known as the Siegert Relation. It converts intensity autocorrelation functions $g_2(t)$ to electric field autocorrelation functions $g_1(t)$. β is a constant determined primarily by the collection optics of the experiment. In our experiment it is between 0.20 and 0.55.

The intercept of $G_2(t)$-1 is usually treated as β ($\beta \approx G_2(0)-1$) when the $G_2(t)$ curve is flat at short time intervals (Figure 3.6). In our experiment, sometimes there are fluctuations at the beginning of the $G_2(t)$ curve. Especially when the gas superficial velocity is high, the $G_2(t)$ curve for transmission geometry is very steep at short time intervals. It is necessary to perform a fitting of the curve over the first few time steps to estimate the value of β. The parameter β is constant in the same experimental configuration, but alters when the experimental conditions change (e.g. laser beam width). The influence of parameter β on the autocorrelation function will be discussed in Chapter5.

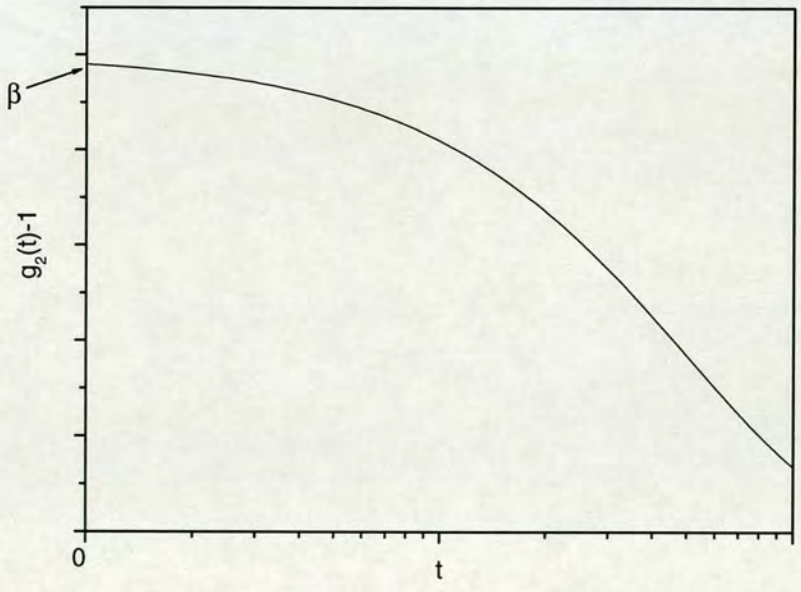

Figure 3.6 Estimation of β from intensity autocorrelation function

3.3.3 From $g_1(t)$ to $\Delta r^2(t)$

There are several autocorrelation functions available depending on different geometry and optical setup [98]. For transmission and planar source, the autocorrelation function is

$$g_1(t) = \frac{\frac{L/l^* + 4/3}{z_0/l^*}\left\{\sinh\left[\frac{z_0}{l^*}\sqrt{\frac{6t}{\tau_0}}\right] + \frac{2}{3}\sqrt{\frac{6t}{\tau_0}}\cosh\left[\frac{z_0}{l^*}\sqrt{\frac{6t}{\tau_0}}\right]\right\}}{\left(1+\frac{8t}{3\tau_0}\right)\sinh\left[\frac{L}{l^*}\sqrt{\frac{6t}{\tau_0}}\right] + \frac{4}{3}\sqrt{\frac{6t}{\tau_0}}\cosh\left[\frac{L}{l^*}\sqrt{\frac{6t}{\tau_0}}\right]} \tag{3.21}$$

$$\approx \frac{\left(\frac{L}{l^*}+\frac{4}{3}\right)\sqrt{\frac{6t}{\tau_0}}}{\left(1+\frac{8t}{3\tau_0}\right)\sinh\left[\frac{L}{l^*}\sqrt{\frac{6t}{\tau_0}}\right] + \frac{4}{3}\sqrt{\frac{6t}{\tau_0}}\cosh\left[\frac{L}{l^*}\sqrt{\frac{6t}{\tau_0}}\right]} \tag{3.22}$$

where L is the sample thickness, τ_0 is the characteristic diffusion time, $\tau_0 = 1/D_s k_0^{\,2}$, D_s is the diffusion coefficient in a system of spherical scatterers. $k_0 = \frac{2\pi}{\lambda}$ and λ is the wavelength of light in the medium. The second expression (equation 3.22) holds for $t << \tau_0$

For a point source

$$g_1(t) = C\int_Q^\infty J_0\left(\frac{R}{L}\sqrt{\xi^2 - Q^2}\right) D(\xi,\varepsilon,\zeta)\,\xi e^{-(1-\zeta)\xi} d\xi \tag{3.23}$$

where $Q \equiv [L/l^*]\sqrt{6t/\tau_0}$, $\varepsilon \equiv \frac{2l^*}{3L}$, $\zeta \equiv \frac{z_0}{L}$, and C is a normalization constant chosen so that $g_1(0) = 1$. The function $D(\xi,\varepsilon,\zeta)$ is given by

$$D(\xi,\varepsilon,\zeta) = \frac{2\varepsilon[(1+\varepsilon\xi) - (1-\varepsilon\xi)e^{-2\xi\zeta}]}{(1+\varepsilon\xi)^2 - (1-\varepsilon\xi)^2 e^{-2\xi}} \tag{3.24}$$

For an incident beam with a Gaussian cross-section of diameter d,

$$g_1(t) = C' \int_0^{\infty} e^{-(\xi^2 - Q^2)(\delta/4)^2} D(\xi, \varepsilon, \zeta) \xi e^{-(1-\zeta)\xi} d\xi \tag{3.25}$$

where $\delta = d / L$ and C' is a normalization constant.

With backscattering geometry and a planar source, the predicted autocorrelation function is

$$g_1(t) = \frac{\sinh\left[\sqrt{\frac{6t}{\tau_0}}\left(\frac{L}{l^*} - \frac{z_0}{l^*}\right)\right] + \frac{2}{3}\sqrt{\frac{6t}{\tau_0}}\cosh\left[\sqrt{\frac{6t}{\tau_0}}\left(\frac{L}{l^*} - \frac{z_0}{l^*}\right)\right]}{\left(1 + \frac{8t}{3\tau_0}\right)\sinh\left[\frac{L}{l^*}\sqrt{\frac{6t}{\tau_0}}\right] + \frac{4}{3}\sqrt{\frac{6t}{\tau_0}}\cosh\left[\frac{L}{l^*}\sqrt{\frac{6t}{\tau_0}}\right]} \tag{3.26}$$

For a sample of infinite thickness, equation (3.26) simplifies to give

$$g_1(t) = \frac{\exp\left[-\frac{z_0}{l^*}\sqrt{\frac{6t}{\tau_0}}\right]}{1 + \frac{2}{3}\sqrt{\frac{6t}{\tau_0}}} \tag{3.27}$$

For backscattering geometry and a planar source, the autocorrelation function is [99]

$$g_1(t) = \frac{1 + \frac{6\gamma}{\left[2(6t/\tau_0)^{1/2} + 3\right]^2}}{1 + \frac{2\gamma}{3}} \exp\left[-\gamma(6t/\tau_0)^{1/2}\right] \tag{3.28}$$

γ is the penetration coefficient. Details of this parameter will be discussed in Chapter5.

There are several approximate equations published [77, 88, 98, 100]. Unfortunately most of these approximations can only be used under specific conditions that do not hold in our experiments. To study a complex system like the microdynamics of hollow glass beads in a gas fluidized bed, the full equations (3.21) and (3.26) for $g_1(t)$ are therefore used in our data analysis.

We are interested in the particle mean square displacement in the fluidized bed. With a simple substitution $6t/\tau_0 = k_0^2 \langle \Delta r^2(t) \rangle$ [95], eqn.(3.21) and eqn.(3.26) can be written as a function of $\Delta r^2(t)$.

Transmission:

$$g_1(t) = \frac{\frac{L/l^* + 4/3}{z_0/l^*}\left\{\sinh\left[\frac{z_0}{l^*}\cdot\Delta r(t)\cdot k_0\right] + \frac{2}{3}\Delta r(t)\cdot k_0 \cdot \cosh\left[\frac{z_0}{l^*}\Delta r(t)\cdot k_0\right]\right\}}{\left(1+\frac{8}{3}\Delta r^2(t)\cdot k_0{}^2\right)\sinh\left[\frac{L}{l^*}\Delta r(t)\cdot k_0\right] + \frac{4}{3}\Delta r(t)\cdot k_0 \cosh\left[\frac{L}{l^*}\Delta r(t)\cdot k_0\right]} \quad (3.29)$$

Backscattering:

$$g_1(t) = \frac{\sinh\left[\Delta r(t)\cdot k_0 \cdot\left(\frac{L}{l^*} - \frac{z_0}{l^*}\right)\right] + \frac{2}{3}\Delta r(t)\cdot k_0 \cdot \cosh\left[\Delta r(t)\cdot k_0\left(\frac{L}{l^*} - \frac{z_0}{l^*}\right)\right]}{\left(1+\frac{8}{3}\Delta r^2(t)\cdot k_0{}^2\right)\sinh\left[\frac{L}{l^*}\Delta r(t)\cdot k_0\right] + \frac{4}{3}\Delta r(t)\cdot k_0 \cdot \cosh\left[\frac{L}{l^*}\Delta r(t)\cdot k_0\right]} \quad (3.30)$$

In the right hand side of equation (3.29) and(3.30), all the variables except $\Delta r(t)$ are known constants. $g_1(t)$ comes from the results of the 4.3.2 analysis. The mean square displacement, $\Delta r(t)$, then can be solved by numerical inversion of Eqn.(3.29) and Eqn. (3.30) by MathCad software.

3.3.4 From $\Delta r^2(t)$ to δV

If the scatterer behaviour shows ballistic movement at short time, each scatterer will remain in free flight for a short time until a collision with another particle. So during that short period, $\Delta r^2(t) = (\delta v)^2 \cdot t^2$ will be a linear with log-log axes. We can use $\Delta r^2(t) = A \cdot t^2$ to fit $\Delta r^2(t) \sim t$ curve to get A, which is equal to $(\delta v)^2$. Figure 3.7 is a $\Delta r^2(t) \sim t$ curve from the DWS experiment. At short time the curve fits a straight line very well. This proves that the scatterer behaviour is indeed ballistic at short time. A plot like Figure 3.7 is always plotted in order to determine granular temperature.

$(\delta V)^2$ is so-called granular temperature. In some references, $\Theta = \frac{1}{3}\langle \delta^2 v \rangle$, which is averaged in the three directions of space. Since DWS explores the diffusive nature of the propagation of the light through the sample medium; it averages over a large volume of the scattering matter. The granular temperature we get here and afterwards are all averaged value over three directions following four data analysis steps from Section 3.3.1 to 3.3.4.

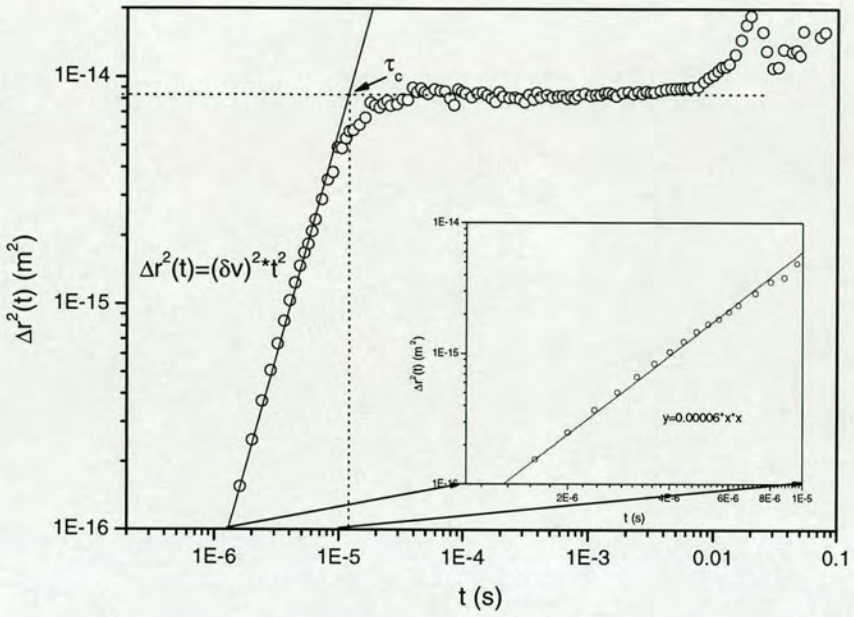

Figure 3.7 Fitting velocity fluctuations from $\Delta r^2(t) \sim t$ curve

Using DWS, Menon and Durian [77] measured glass bead granular temperatures and estimated mean free path in a gravity-driven flow. In Figure 3.7, we got similar curve as theirs. For the data in Figure 3.7, the average velocity fluctuation $\delta v \approx 7.7$ mm/s and the average collision time $\tau_c \approx 11$ μs. The mean free path $s = \delta v \tau_c$ is about 0.085 μm.

3.4 Conclusion

DWS is a non-intrusive measurement method that has been developed from the dynamic light scattering technique. Based on the light diffusion approximation and treating multiple scattering events as several averaged scattering paths during light

propagation, DWS can be applied to the study of particle dynamics in the gas-solid fluidized bed. By measuring the light intensity autocorrelation function, particle mean square displacement and its velocity fluctuations could be determined.

Chapter 4 Fluidization experiments

4.1 Introduction

4.1.1 Fluidization

Fluidization is one of the most important applications in the solid processing industry. When a gas is pumped through a bed of settled solid particles, several types of behaviour are possible. When the flow rate is very low, the particles will not be disturbed. This is a fixed bed. If the upward flow rate is very large the bed mobilizes pneumatically and particles may be swept out of the bed. In the intermediate flow rate regime, as shown in Figure 4.1, various forms of fluidization such as minimum fluidization, smooth fluidization, bubbling fluidization, slugging, turbulent fluidization and fast fluidization occur, depending on fluidizing velocity and the properties of the system.

A fluidized bed displays a number of liquid-like properties, with both desirable and undesirable characteristics. Its advantages are:

- The smooth, liquid like flow of particles allows continuous automatically controlled operations with easy handling;
- Rapid mixing, leading to uniform temperatures and concentrations throughout the reactor;
- Applicability for large or small scale operations
- Heat and mass transfer rates between gas and particles are high, as are

transfer rates between the bed and walls or immersed surfaces.

There are also some disadvantages:

- Particle break-up is common. Friable solids are pulverized and entrained by the gas
- Erosion of pipes and vessels from abrasion by particles can be serious
- The rapid mixing of solids in the bed causes non-uniform residence times when the bed is used as a continuous flow reactor

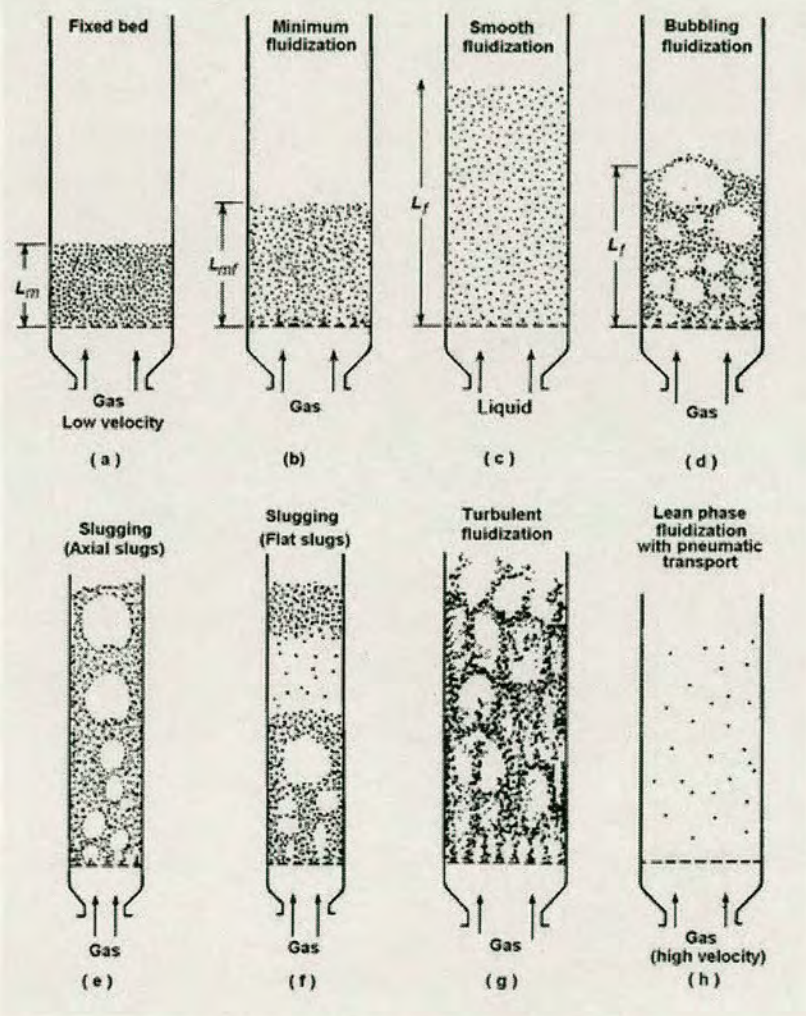

Figure 4.1 Various forms of contacting a batch of solid with fluid [101]

The uses of fluidized beds are wide in industry. Typical uses include reactors, heat exchange, adsorption, granulation, drying operations and coating.

4.1.2 Prediction of minimum fluidization

Consider a bed of particles resting on a distributor designed for uniform upflow of gas. The onset of fluidization occurs when

$$drag\ \ force\ \ by\ \ upward\ \ moving\ \ gas = weight\ \ of\ \ particles$$

Or

$$(pressure\ \ drop)\times(cross\ \ \text{sec}tional\ \ area\ \ of\ \ the\ \ bed) = (volume\ \ of\ \ bed)$$
$$\times(volume\ \ fraction\ \ of\ \ solids)\times(specific\ \ weight\ \ of\ \ solids)$$

$$\Delta P \cdot A = W = A \cdot h_{mf} \cdot (1-\varepsilon_{mf})\left[(\rho_s - \rho_g)\, g\right] \tag{4.1}$$

by rearranging, the minimum fluidization condition is

$$\frac{\Delta P}{h_{mf}} = (1-\varepsilon_{mf})(\rho_s - \rho_g)\, g \tag{4.2}$$

The frictional pressure drop through fixed beds of length L_m containing a single size of isotropic solids of screen size d_p at a voidage ε_m has been correlated by Ergun [102] by the equation

$$\frac{\Delta P}{L_m} = 150\frac{(1-\varepsilon_m)^2}{\varepsilon_m^{\,3}}\frac{\mu u_o}{(\phi_s d_p)^2} + 1.75\frac{1-\varepsilon_m}{\varepsilon_m^{\,3}}\frac{\rho_g u_o^{\,2}}{\phi_s d_p} \tag{4.3}$$

The superficial velocity at minimum fluidizing conditions, U_{mf}, is found by combining eqn. (4.2) and eqn. (4.3):

$$\frac{1.75}{\varepsilon_{mf}^{\,3}\phi_s}\left(\frac{d_p u_{mf}\rho_g}{\mu}\right)^2 + \frac{150(1-\varepsilon_{mf})}{\varepsilon_{mf}^{\,3}\phi_s^{\,2}}\left(\frac{d_p u_{mf}\rho_g}{\mu}\right) = \frac{d_p^{\,3}\rho_g(\rho_s-\rho_g)g}{\mu^2} \tag{4.4}$$

in the special case of very small particles, eqn. (4.4) simplifies to

$$u_{mf} = \frac{d_p^2 (\rho_s - \rho_g) g}{150\mu} \frac{\varepsilon_{mf}^3 \phi_s^2}{1-\varepsilon_{mf}} \qquad \mathrm{Re}_{p,mf} < 20 \qquad (4.5)$$

For very large particles,

$$u_{mf}^2 = \frac{d_p (\rho_s - \rho_g) g}{1.75\rho_g} \varepsilon_{mf}^3 \phi_s \qquad \mathrm{Re}_{p,mf} > 1000 \qquad (4.6)$$

4.1.3 The Geldart particle classification

By observing the fluidization of many types of solids, Geldart classified particles into four groups according to their fluidization properties at ambient conditions. The Geldart Classification of Powders is now widely used in the field of powder technology [103].

Group A powders, when fluidized by air at ambient conditions, give a region of non-bubbling fluidization beginning at U_{mf}, followed by bubbling fluidization as fluidizing velocity increases. The fluidization regime is called 'delayed bubbling' between the state of minimum fluidization and the fluidization state in which bubbles form. For group A particles, $U_{mf} < U_{mb}$.

Group B powders give only bubbling fluidization under these conditions, $U_{mf} \square U_{mb}$.

Group C powders are very fine and cohesive. They are incapable of fluidization in the strict sense.

Group D powders are large particles that are distinguished by their ability to produce deep spouting beds.

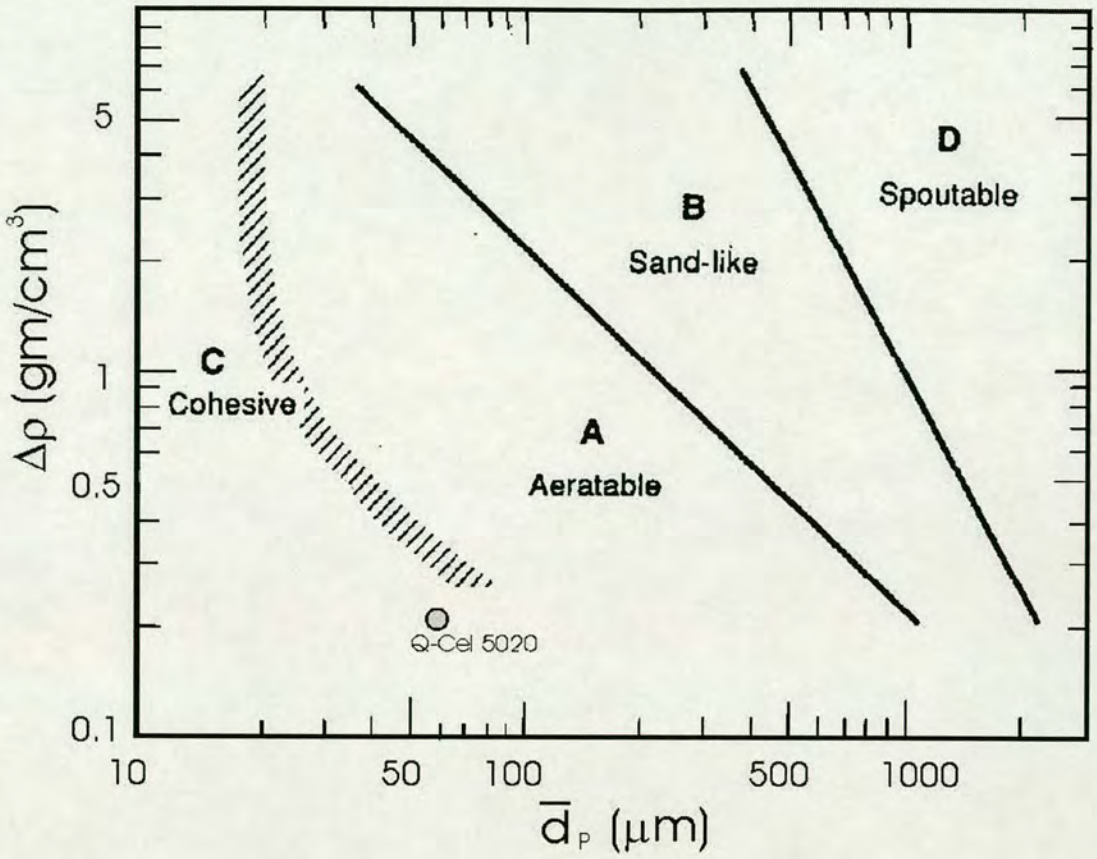

Figure 4.2 Geldart diagram of particle group classification. The particle used in the experiment, Q-Cel 5020, is in Group C region

Much work has been done on the bubble velocities and shapes, agglomerations, elutriation and segregation in fluidized beds. Homogeneous fluidization of fine powders using various gases and pressures has been studied by Geldart et al [104, 105]. Representative Geldart B particles are glass beads and sands, which are commonly used in many cold model experiments. A lot of work has also done on the inter-particle forces between Group C particles [106, 107].

In recent years, simulation-based study of fluidization has been actively pursued in both academic circles and industry. Although many researchers proposed new models and quantitative results, experimental data are still needed to validate these models.

4.2 Fluidized bed

Several two-dimensional rectangular fluidized beds were built. These fluidized beds are 194 mm in width and 600mm in height (except bed No. 2). To minimize the static build-up and disruption of the flow phenomena by adhesion, the two walls were made of transparent glass plates. The non-scratch glass is also a good optical medium which does not distort the laser transport path. The glass sheets were mounted on the aluminium frames of different thicknesses. The various frame thicknesses made the bed thickness vary from 5.44 mm to 12.07 mm, as shown in Table 4.1. Air was introduced through a wind box below a sintered metal gas distributor. The fluidized bed was fixed on a position-adjustable stage so that DWS measurements could be made over wide regions of the bed without the constant need to realign the optics. The particle dynamics at different parts of the bed could then be studied by moving the stage in horizontal and vertical directions. The design of the bed is shown in Figure 4.4. The whole fluidizing system is shown in Figure 4.3.

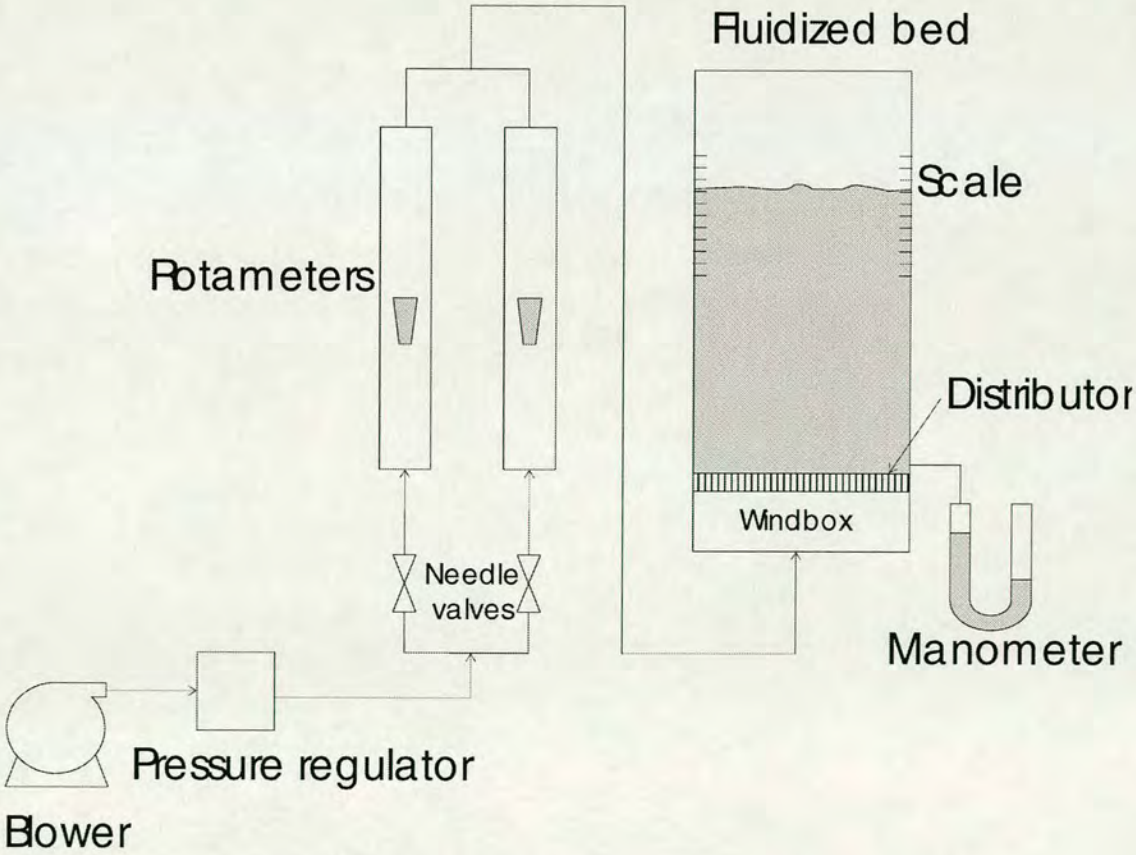

Figure 4.3 Fluidized bed operating system

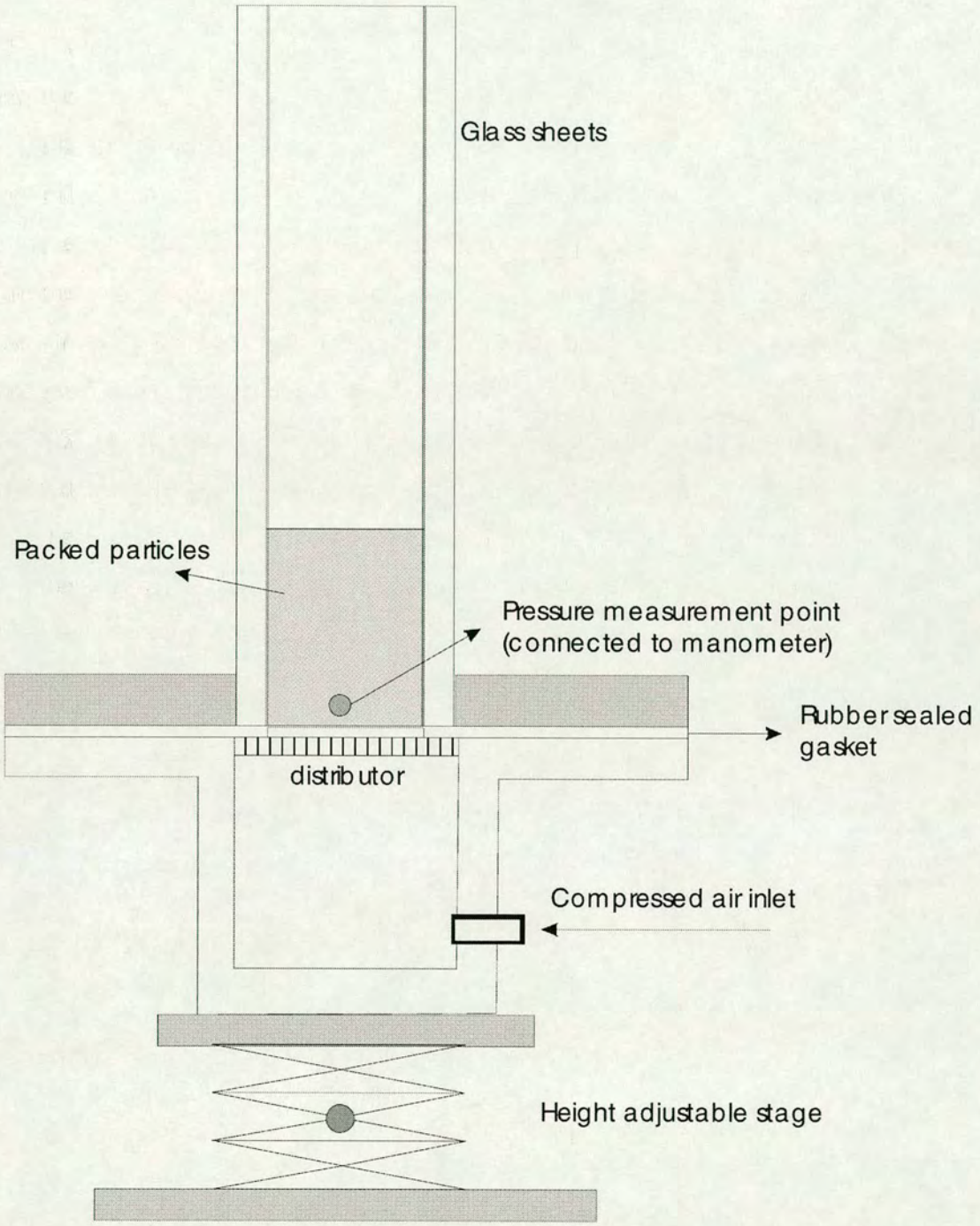

Figure 4.4 Sectional view of a fluidized bed

Table 4.1 Dimensions of fluidized beds used in the experiment

Fluidized bed number	Dimension (Height × width × depth, mm)
1	600 × 194 × 5.44
2	360 × 155 × 7.73
3	600 × 194 × 8.42
4	600 × 194 × 10.2
5	600 × 194 × 12.1

4.3 Fluidizing material

In all experiments compressed air was used as fluidizing gas. The air-conditioned Light Scattering Laboratory has constant temperature and humidity. All fluidization experiments were run under ambient conditions. The flow rate was controlled by two needle valves and measured with two parallel rotameters.

Two kinds of particles were used as fluidizing materials. The first one was a used FCC catalyst with brownish colour. This FCC catalyst belonged to Geldart group A. Because of its dark colour and strong light absorption, a powerful laser would be needed to acquire a satisfactory signal. In the DWS experiments, FCC catalyst didn't work well because very little scattered light passed through the fluidized bed and it was difficult to calculate the quantitive effect of strong light absorption although this particle displays excellent fluidization between U_{mf} and U_{mb}.

The second material used in the experiment was Q-Cel® 5020 hollow glass beads, manufactured by the PQ Cooperation. According to the Geldart particle classification, Q-Cel® 5020 particles should in theory belong to group C, which is cohesive and difficult to fluidize.

MALVERN INSTRUMENTS MASTERSIZER

Result: Analysis Report

Sample Details

Sample ID: hollow glass beads
Sample File: 03181102
Sample Path: C:\LIANSONG\
Sample Notes: Q-CEL hollow glass beads 5020

Run Number: 3
Record Number: 1

Measured: 18 Nov 2002 11:11
Analysed: 18 Nov 2002 11:11
Result Source: Analysed

System Details

Range Lens: 300 mm
Presentation: 3OHD
Analysis Model: Polydisperse
Modifications: None

Beam Length: 2.40 mm
[Particle R.I. = (1.5295, 0.1000); Dispersant R.I. = 1.3300]

Sampler: None

Obscuration: 21.0 %
Residual: 0.306 %

Result Statistics

Distribution Type: Volume
Mean Diameters:
D [4, 3] = 60.14 um

Concentration = 0.0681 %Vol
D (v, 0.1) = 10.56 um
D [3, 2] = 21.02 um

Density = 1.700 g / cub. cm
D (v, 0.5) = 53.76 um
Span = 2.021E+00

Specific S.A. = 0.1679 sq. m / g
D (v, 0.9) = 119.18 um
Uniformity = 6.376E-01

Size Low (um)	In %	Size High (um)	Under%	Size Low (um)	In %	Size High (um)	Under%
0.49	0.05	0.58	0.05	22.49	3.33	26.20	26.56
0.58	0.09	0.67	0.14	26.20	3.72	30.53	30.28
0.67	0.12	0.78	0.26	30.53	4.27	35.56	34.56
0.78	0.13	0.91	0.39	35.56	4.98	41.43	39.54
0.91	0.14	1.06	0.53	41.43	5.82	48.27	45.35
1.06	0.13	1.24	0.66	48.27	6.70	56.23	52.06
1.24	0.13	1.44	0.79	56.23	7.60	65.51	59.66
1.44	0.12	1.68	0.92	65.51	8.46	76.32	68.12
1.68	0.12	1.95	1.04	76.32	8.43	88.91	76.55
1.95	0.14	2.28	1.18	88.91	7.67	103.58	84.21
2.28	0.17	2.65	1.35	103.58	6.24	120.67	90.45
2.65	0.23	3.09	1.58	120.67	4.52	140.58	94.97
3.09	0.32	3.60	1.90	140.58	2.88	163.77	97.85
3.60	0.44	4.19	2.35	163.77	1.54	190.80	99.40
4.19	0.61	4.88	2.96	190.80	0.60	222.28	100.00
4.88	0.83	5.69	3.78	222.28	0.00	258.95	100.00
5.69	1.08	6.63	4.87	258.95	0.00	301.68	100.00
6.63	1.37	7.72	6.24	301.68	0.00	351.46	100.00
7.72	1.68	9.00	7.91	351.46	0.00	409.45	100.00
9.00	1.98	10.48	9.90	409.45	0.00	477.01	100.00
10.48	2.25	12.21	12.15	477.01	0.00	555.71	100.00
12.21	2.49	14.22	14.64	555.71	0.00	647.41	100.00
14.22	2.68	16.57	17.32	647.41	0.00	754.23	100.00
16.57	2.86	19.31	20.17	754.23	0.00	878.67	100.00
19.31	3.06	22.49	23.23				

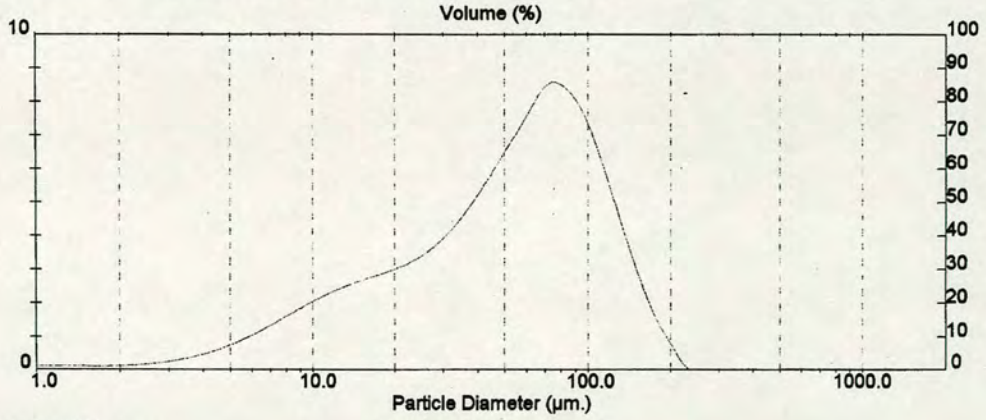

Malvern Instruments Ltd.
Malvern, UK
Tel:=+[44] (0)1684-892456 Fax:+[44] (0)1684-892789

Mastersizer S long bed Ver. 2.15
Serial Number: 33148-06

18 Nov 02 1

Figure 4.5 Q-Cel® 5020 particle size distribution

(measured by MasterSizer S, Malvern, UK)

The physical form of Q-Cel® 5020 hollow glass beads is a white free-flowing powder. According to the product specification, these particles have a hollow structure with bulk density 0.11 g/cm^3 and effective density 0.20 g/cm^3. They are used as sensitizers for water based industrial explosives used in mining, quarrying and construction. Their maximum working pressure is 3.4 MPa which is far above our experimental pressure of one atmosphere. The particle size was analysed by a Malvern Master Sizer (attached Figure 4.5). The particle diameter ranged from 20 to 100 μm and the mean diameter is 60 μm. From the Geldart particle classification diagram, these particles should theoretically lie in the Group C region.

4.4 Particle characterization

Compressed air was introduced into the fixed bed. As the gas flow increased, the bed passed through different types of fluidization. At low gas velocity, the bed remained in the fixed state without any changes in height as the gas velocity increased and pressure drop increased. When the gas velocity reached nearly 1.45×10^{-3} m/s, the bed started expanding smoothly with some small channelling flows observed near the bottom of the bed. There was a rapid increase in pressure drop after $U_s=1.45\times10^{-3}$ m/s, which might have been caused by the work required to overcome the cohesive forces between particles. More small channelling flows could be observed in the inhomogeneous bed when gas velocity increased. At higher gas velocity (6.28 mm/s), these small channels disappeared in the bulk volume of the bed except that a few bubbles appeared occasionally near the gas distributor.

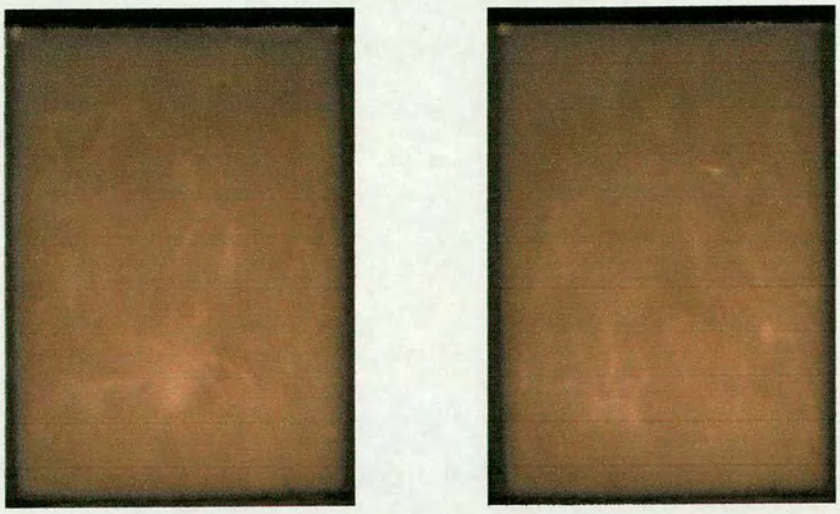

Figure 4.6 Snapshot of fluidization status of Q-Cel 5020 hollow glass particles I. Channel flows could be found in the bed at low gas velocity. The pictures were taken at U_s=1.93 mm/s

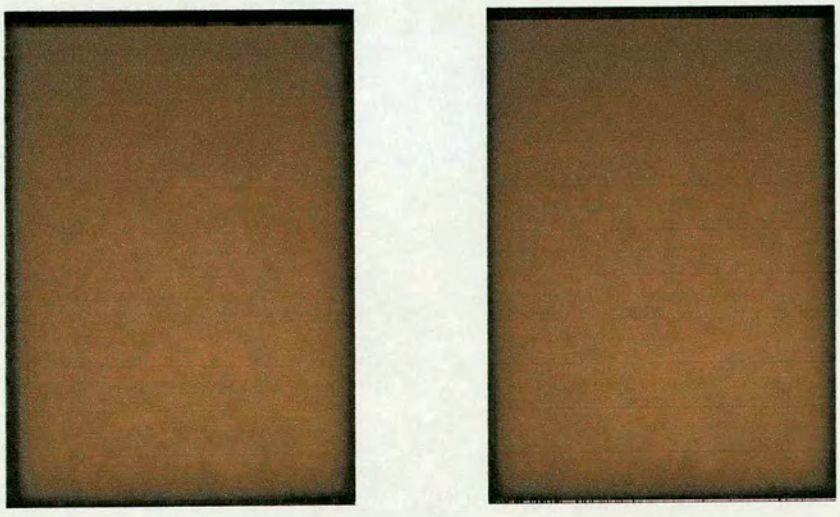

Figure 4.7 Snapshot of fluidization status of Q-Cel 5020 hollow glass particles II. When gas velocity increased, more channel flows could be found in the bed above the gas distributor, the bed was still inhomogeneous. The pictures were taken at U_s=3.62 mm/s

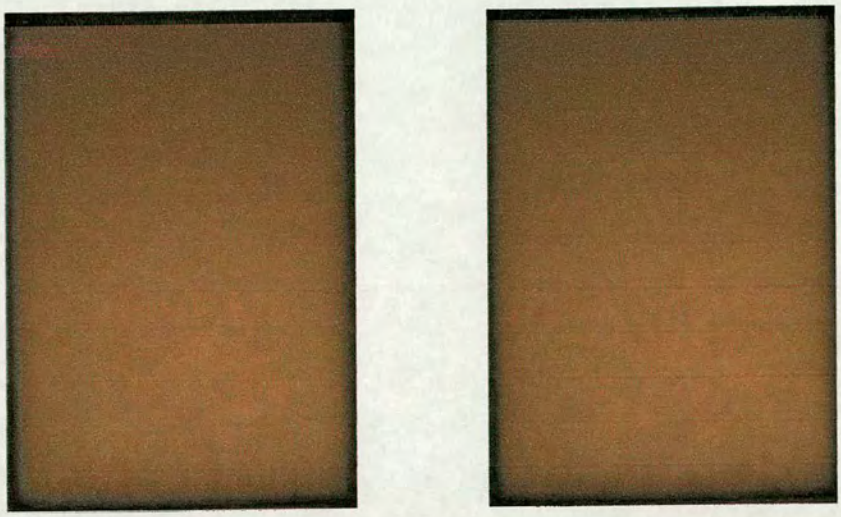

Figure 4.8 Snapshot of fluidization status of Q-Cel 5020 hollow glass particles III. As gas velocity was increased, the bed became homogeneous, yet some channels still could be found occasionally near the distributor. The pictures were taken at U_s=6.28 mm/s

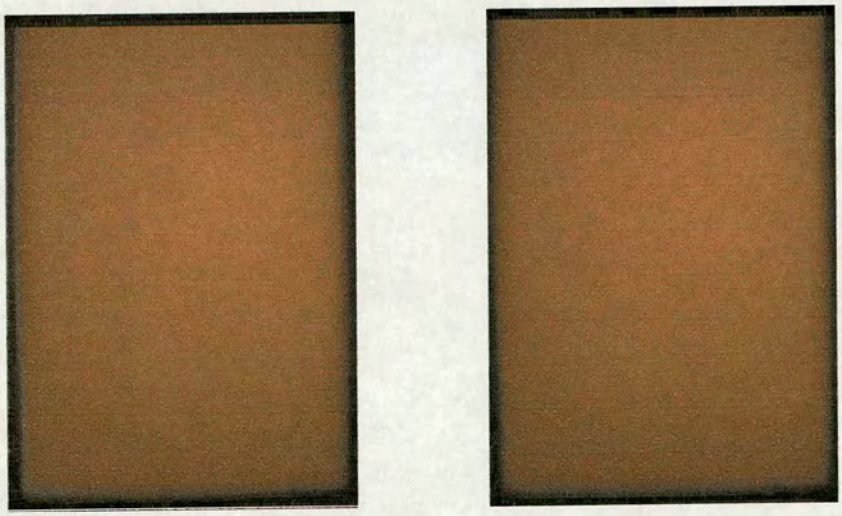

Figure 4.9 Snapshot of fluidization status of Q-Cel 5020 hollow glass particles IV. When the gas velocity is high, the whole bed is homogeneous. The pictures were taken at U_s=12.08 mm/s

4.4.1 Bed expansion

Bed expansion is one of the most important parameters of a fluidized bed. From Figure 4.10, we find that the bed expansion increased with gas superficial velocity, particularly for low excess gas velocities. However, as the velocity increased, the expansion became slower and for the higher velocities the additional expansion from an increase in the velocity was small. (Section 4.4.3 and 4.4.4 are details of estimation of U_{mf} and U_{mb}, which are showed in Figure 4.10)

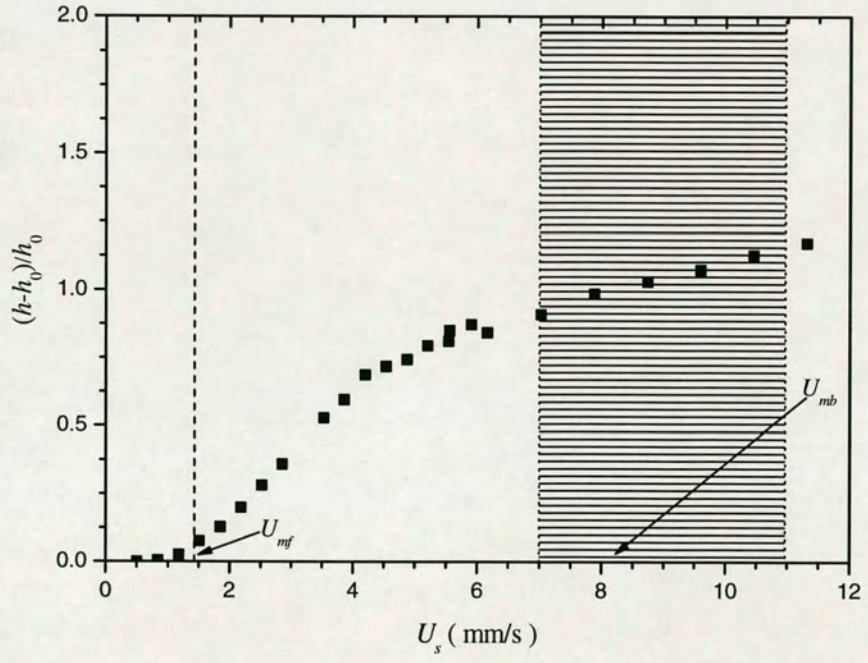

Figure 4.10 Bed expansion versus gas superficial velocity

4.4.2 Pressure drop across the bed

The ΔP-versus-u_s diagram is particularly useful as a rough indication of the quality of fluidization, especially when visual observations are not possible. Minimum fluidization velocity and minimum bubbling velocity can also be determined by the pressure drop versus velocity curve.

Figure 4.11 shows the variation of pressure drop across the bed with gas velocity. From the curve the pressure increased quickly at velocities between 1.25 and 1.45 mm/s. There was a peak near 1.45 mm/s which might have been the point where the drag forces caused by the gas flow broke the interparticle cohesive force. After that the bed started to expand, and the pressure drop kept increasing slowly until gas superficial velocity was 4 mm/s then remained constant. The pressure drop across the bed beyond this point is approximately 5% less than the weight of the bed.

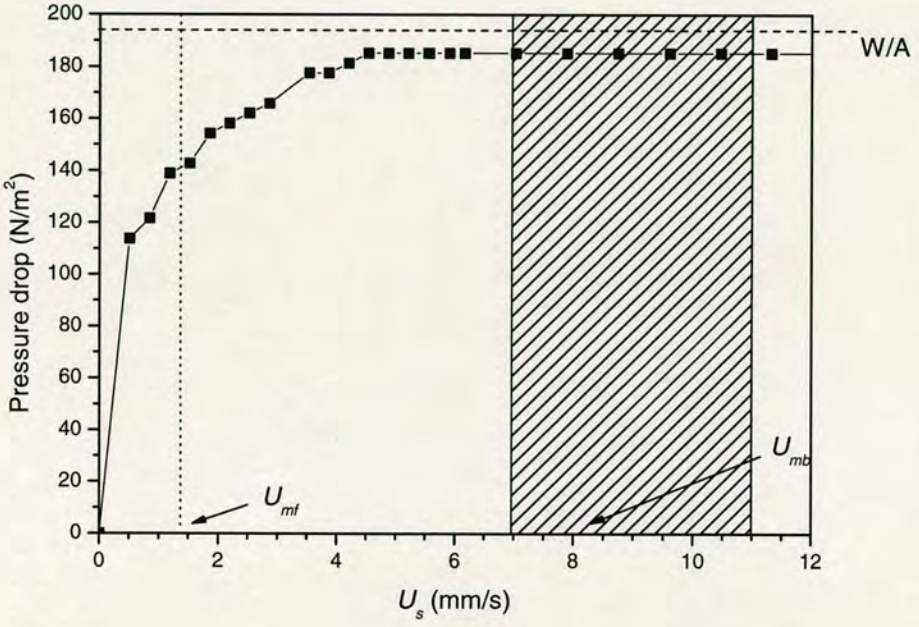

Figure 4.11 Pressure drop across the bed versus gas superficial velocity

The U_{mf} as shown by pressure drop line is more like 4 mm/s, which is larger than the U_{mf} result indicated by the bed expansion curve (1.45 mm/s) and by the theoretical calculation below (1.35 mm/s). The cohesion in the bed might be one reason that delayed the pressure drop becoming constant. One other possible reason is that there were small channels near the gas distributor when superficial velocity was above 1.45 mm/s. The region near the distributor (where the pressure drop was measured by U-tube manometer) was not homogeneous which might also delay the pressure drop across the bed becoming constant in Figure 4.11. Disagreement between U_{mf} values

obtained from ΔP versus U_s and bed expansion can be found in previous work on micron-size ceramic powders and aerogel powders (both in Geldart group C). These publications also present non-linear ΔP versus U_s curves [106, 107]. As Q-Cel 5020 powder is micron size and also in Group C, under this situation we preferred to determine U_{mf} from the bed expansion curve rather than the ΔP vs. U_s.

4.4.3 Minimum fluidization velocity U_{mf}

Equation (4.7) was used to calculate U_{mf} [101]:

$$U_{mf} = \frac{\left(60\times10^{-6}\right)^2\times(110-1.29)\times9.81}{150\times1.73\times10^{-5}}\cdot\frac{(0.67)^3\times1}{1-0.67} \qquad (4.8)$$
$$= 1.35\times10^{-3} \quad m\cdot s^{-1}$$

when the gas superficial velocity is 1.35×10^{-3} m·s^{-1}, the Reynolds number is:

$$\mathrm{Re} = \frac{\rho u d}{\mu} = \frac{1.29\times1.35\times10^{-3}\times60\times10^{-6}}{1.73\times10^{-5}} = 6.04\times10^{-3} \leq 20 \qquad (4.9)$$

So the usage of equation (4.8) here is valid.

From the experimental bed expansion versus gas superficial velocity curve we determined the minimum fluidization velocity to be 1.45×10^{-3} m/s, which is quite close to the estimated value.

4.4.4 Estimation of Minimum Bubbling Velocity

Usually U_{mb} is defined as the gas velocity when the first bubble appears in the bed. In fluidization experiments it is difficult to find a clearly defined superficial gas velocity at which the first bubble appears in the bed, especially when the fluidizing particles are semi-transparent white powders. A decreasing gas velocity method was used to measure U_{mb} in a rectangular fluidized bed (15mm × 312mm × 600mm). The measured U_{mb} (defined as the velocity at which there were no visible bubbles surfacing) was 8.2 mm/s approximately. This value was in good agreement with the range of 7 – 11 mm/s which was based on analysis of bed expansion data, as shown below.

4.4.4.1 Low-velocity (nonbubbling) regime

Between the minimum fluidizing and minimum bubbling velocities, the bed is assumed to expand in a "particulate" manner in which increases in fluidizing velocity are compensated for by increases in the interparticle spacing so as to keep the drag force on each particle constant and equal to its weight. This behaviour should be described by the Richardson-Zaki correlation [108]:

$$\frac{u}{u_t} = \varepsilon^n \tag{4.10}$$

where u is the superficial fluidizing velocity, u_t the terminal velocity of the particles and ε the bed void fraction, which for this behaviour is the true interparticle void fraction.

These particles are small and even at the highest superficial velocity used the Reynolds number is only 0.24, so the exponent should be the Richardson and Zaki value for the lowest Reynolds number range, 4.65.

The implication is that a logarithmic plot of superficial velocity versus voidage should be a straight line with a slope of 4.65.

In the packed bed state (bed height h_0), the bulk density of the particles is 110 kg/m^3 as opposed to an effective density of the particles equal to 200 kg/m^3, suggesting that the solids volume fraction is 0.55. At any greater bed height h, the solids volume fraction will be $0.55h_0/h$ and voidage

$$\varepsilon = 1 - 0.55\frac{h_0}{h} \tag{4.11}$$

A logarithmic graph of superficial velocity u versus ε showed a straight line of constant slope $n = 6.94$ and correlation coefficient 0.997, up to a superficial velocity of 7.54 mm/s. This suggests that the minimum bubbling velocity is about 7.54 mm/s, corresponding to a voidage $\varepsilon_{mb} = 0.76$.

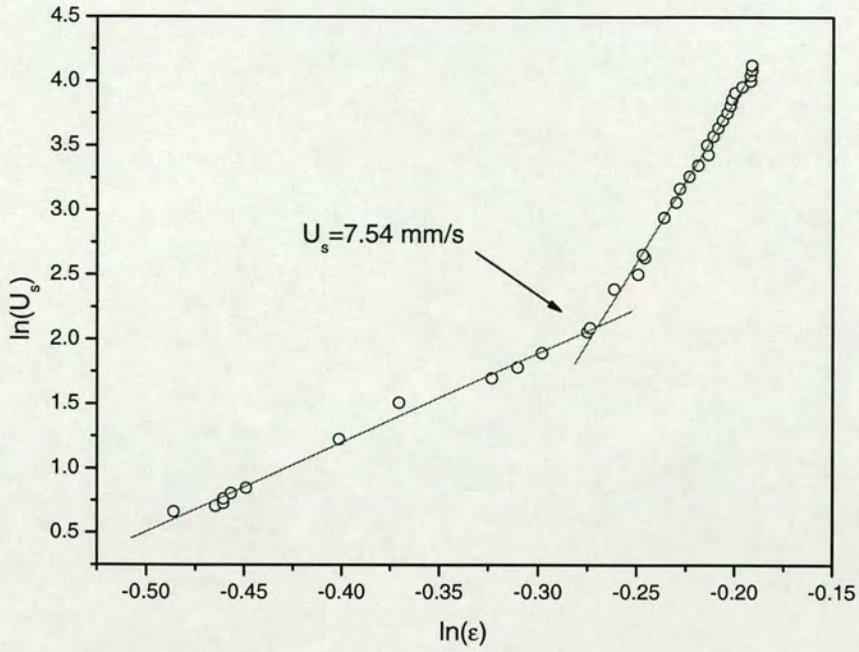

Figure 4.12 Determining U_{mb} by $U_s \sim \varepsilon$ curve

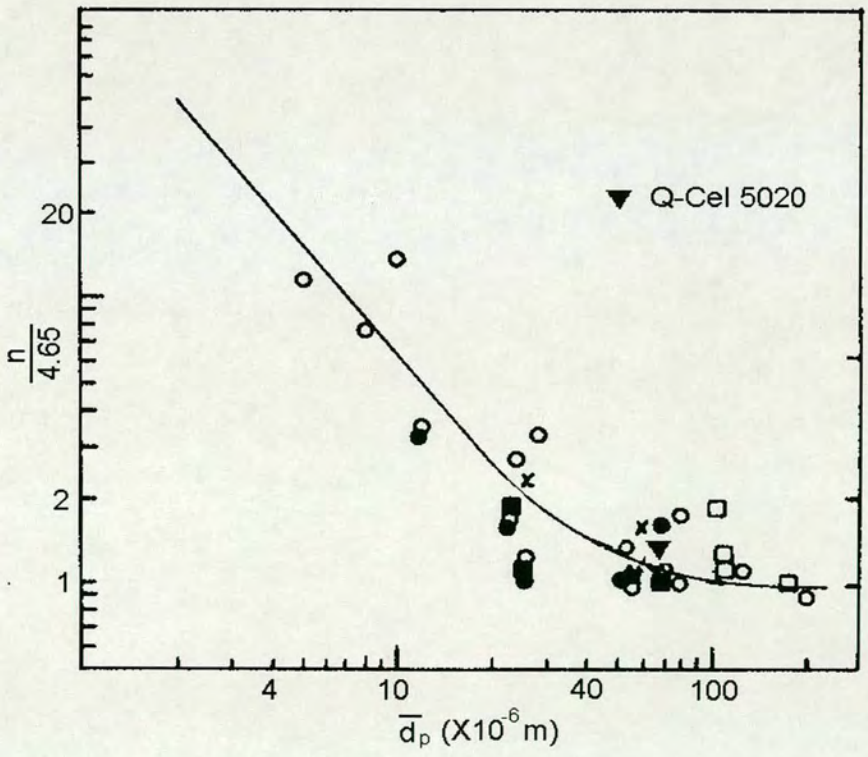

Figure 4.13 n/4.65 as a function of mean particle size [109]

The slope of Q-Cel 5020 particle $U_s \sim \varepsilon$ is 6.94. It accords well with Geldart and Wong's correlation curve Figure 4.13 [109].

4.4.4.2 Higher velocity (bubbling) regime

In this regime, the further bed expansion is assumed to be due to the holdup of the bubbles rising through the bed. If this is the case, a graph of $\frac{h}{h-h_{mb}}$ versus $\frac{1}{u-u_{mb}}$ should be a straight line with a slope of U_a, the absolute rise velocity of the bubbles that cause the expansion [110].

Here, we take U_{mb} to be 7.4 mm/s as estimated above. h_{mb}/h_0 at this fluidizing velocity was equal to 2.29.

$\frac{h}{h-h_{mb}}$ was plotted against $\frac{1}{u-u_{mb}}$ on a linear plot and it was found that the data above 7.54 mm/s, except for the point at 11.6 mm/s which is the next above 7.4 mm/s, fell on a straight line with a correlation coefficient of 0.997 and a slope of 61 mm/s, which is taken to be a reasonable value for the rise velocity of the first small bubbles formed.

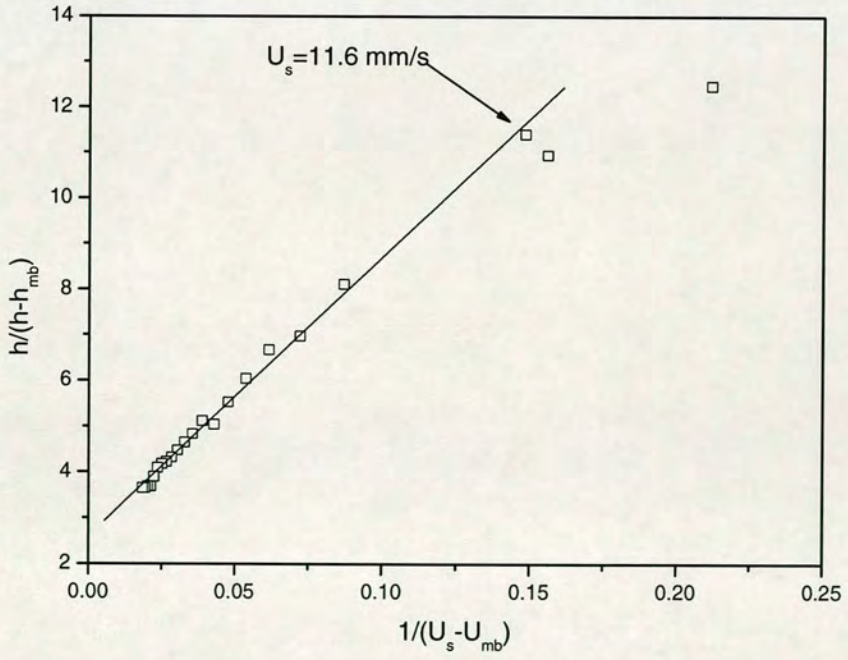

Figure 4.14 Determing U_{mb} by $h/(h-h_{mb})$ vs. $1/(U_s-U_{mb})$ curve.

The conclusion is that the minimum bubbling velocity of the particles is somewhere between 7.54 and 11.6 mm/s. Compared with a minimum fluidizing velocity of only 1.45 mm/s, this gives a wide regime of smooth expansion and homogeneous bed behaviour above the minimum fluidizing velocity.

4.5 Conclusion

According to the Geldart particle classification, the Q-Cel 5020 hollow glass particles should belong to group C which is very difficult to fluidize. On the contrary, these particles presented excellent fluidization behaviour: they could be fluidized easily, and the bed expanded smoothly at gas velocity higher than U_{mf}. Small channelling flows and bed inhomogeneities could be found above U_{mf}. However, these channels disappeared at higher gas velocities. The bed became homogeneous and remained expandable up to a relatively high gas velocity.

Chapter 5 Parametric study of DWS experiments

5.1 Transmitted light intensity profile measurement

Transmitted light intensity is an important factor in the DWS experiment. If the transmitted light intensity is still very strong after being scattered several times by the moving particles in the fluidized bed, it might damage the light sensitive photomultiplier tube (PMT). On the other hand, if the transmitted light intensity is low, the small signal to noise ratio will make the measurement more difficult. Also as will be discussed in Section 5.2, by measuring transmitted light intensity we can determine two key parameters in the DWS experiment data analysis— transport mean free path l^* and absorption length l_a.

To find a proper signal to noise ratio suitable to the PMT measurement range, the transmitted light intensity profile was studied first.

5.1.1 Total transmission measurement

In the Dynamic Light Scattering lab, the Coherent Innova 90 argon ion laser system produces a fixed laser beam with width about 2 mm. In the intensity measurement experiments when the particles in the fluidized bed were illuminated by the laser, because the light is scattered randomly in every direction, the scattering region is

roughly cylindrically shaped with its axis in the light propagation direction, as shown in Figure 5.1.

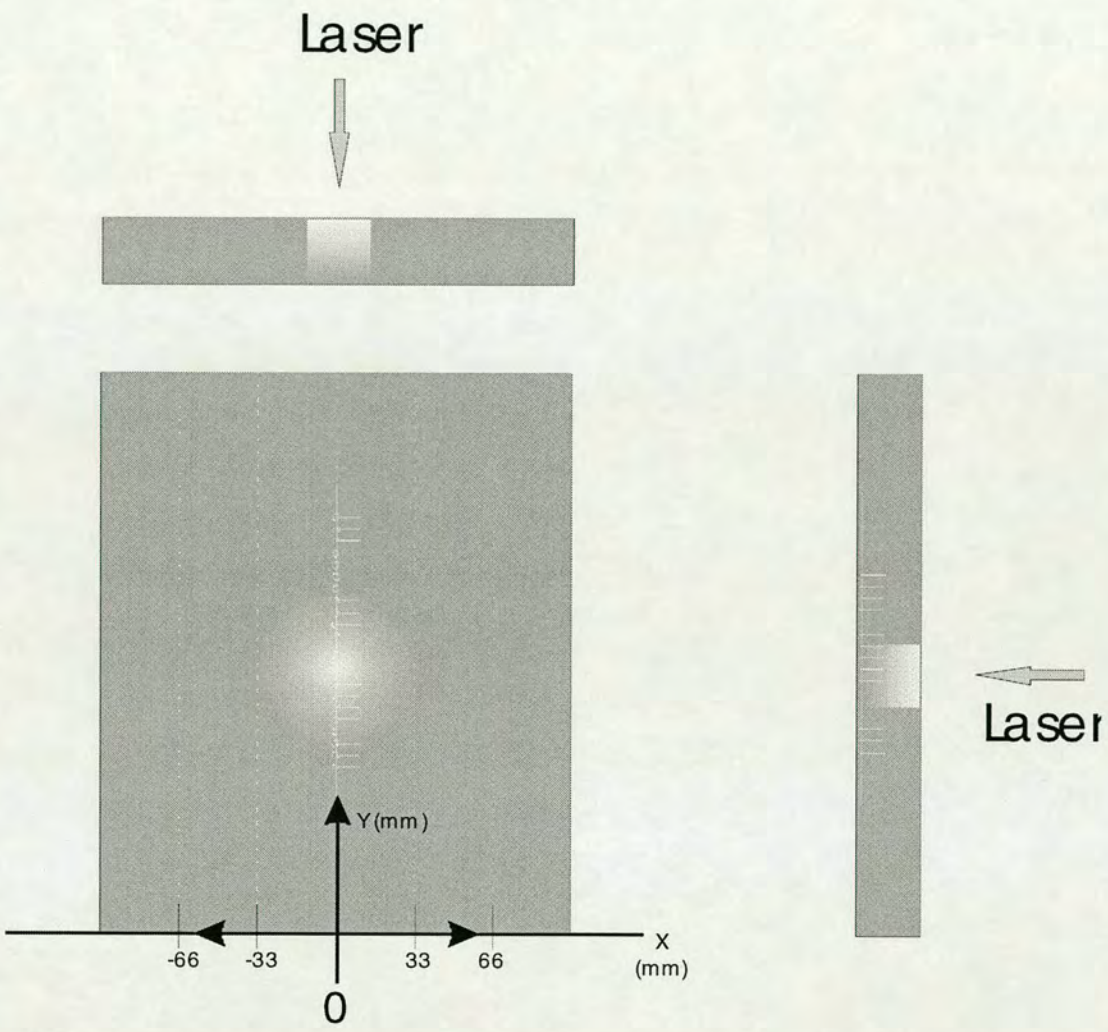

Figure 5.1 Light propagation in the fluidized bed (arrows indicate laser direction)

Due to different gas superficial velocities and thicknesses of the fluidized bed used in the experiment, various sizes of light spot could be found on the other side of the fluidized bed. Usually the round scattering areas grew bigger as the superficial gas velocity was increased or as thicker fluidized beds were used. The maximum light intensity was detected in the centre of the scattering area while there was no clear boundary between the scattering area and the non-scattering area as the light decayed in the bed.

An image analysis method was initially used to study the intensity profiles. The results showed that the light intensity was isotropic. Then the profile of the transmissions was measured in the vertical direction using an optical fibre which was fixed on a linear stage. By adjusting the height of the stage, the intensity information at different positions could be measured. In the experiment the distance between successive measurement positions was 1mm with accuracy 0.1 mm. Depending on the size of the light scattering area, up to 32 positions were studied for one intensity profile curve.

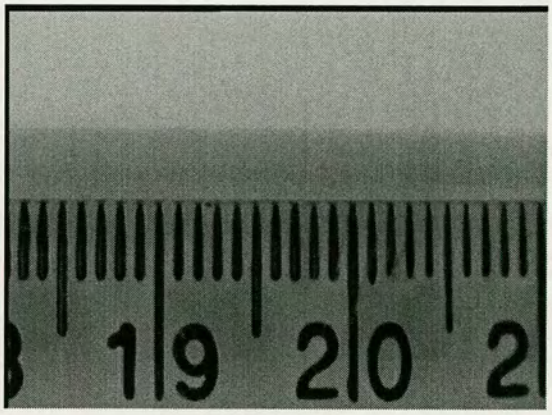

Figure 5.2 Calibration used in the image analysis process. The scale in this picture was used to determine the real dimensions of the object in the following pictures.

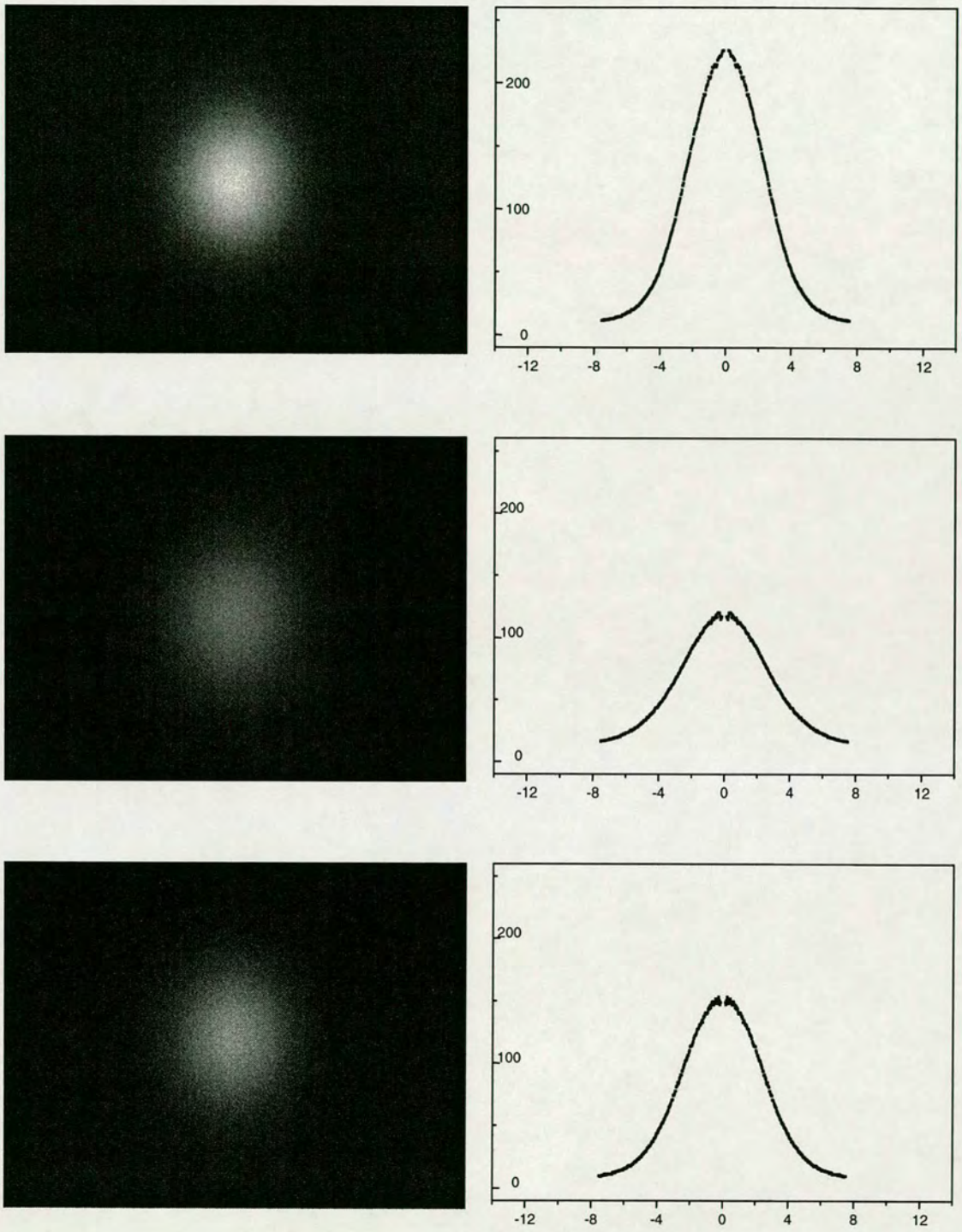

Figure 5.3 Using image analysis methods, the transmitted light intensity profiles were measured. The vertical axis is grey scale value (assume pure white is 255 and pure black is 0), the horizontal axis is measuring position with units of millimetres.

A stream of photons arrives at the fibre detector after being multiply scattered in the fluidized bed. The frequency of these photons (the number of photons encountered by the detector per second), which is proportional to the intensity of the transmitted light, was counted by the ALV-5000E digital autocorrelator.

Figure 5.4 -- Figure 5.7 are the transmission measurement results at different superficial gas velocities and in various fluidized beds. The transmitted intensities obey Gaussian profiles (smooth curves) very well. These results also agree well with results from the image analysis method (Figure 5.3). By integration of the photon frequency curve, the relative transmission can be calculated.

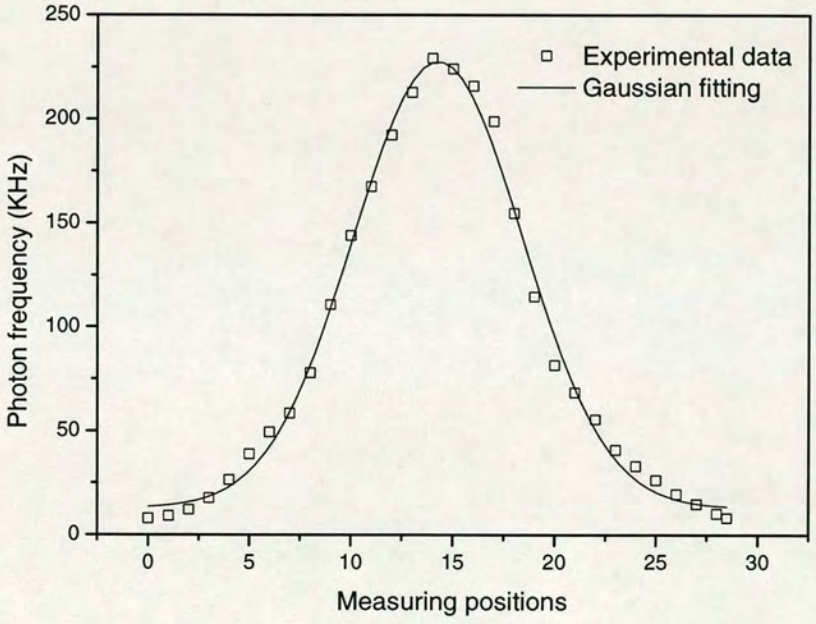

Figure 5.4 The transmission measurement results from fluidized bed 3, measuring position X=33, Y= 250 mm, bed expansion E_b = 0.538

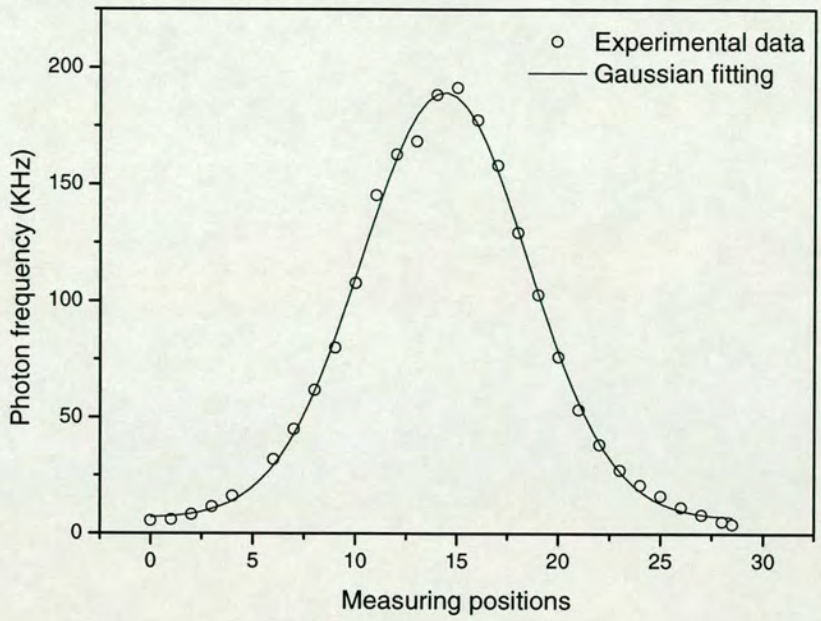

Figure 5.5 The transmission measurement results from fluidized bed 3, measuring position X=-66, Y= 180 mm, bed expansion E_b = 0.538

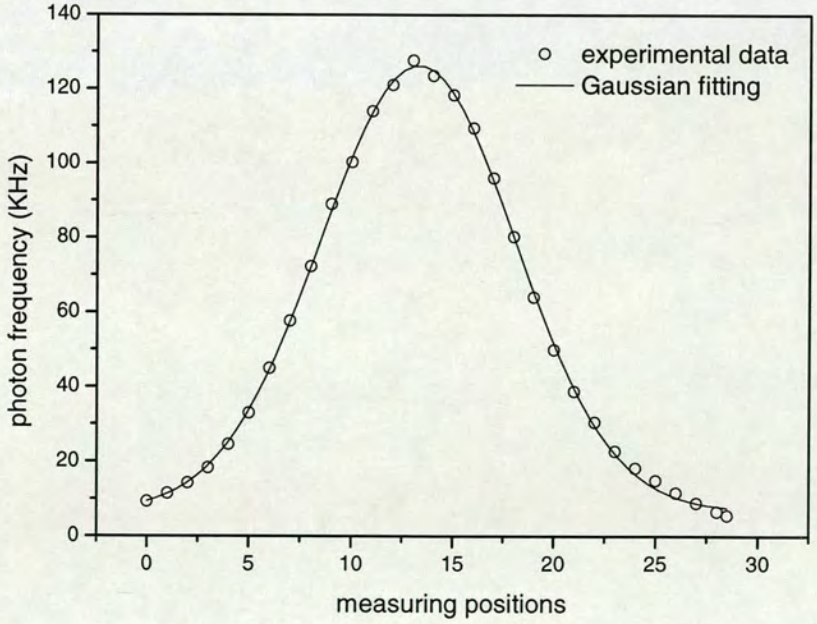

Figure 5.6 The transmission measurement results from fluidized bed 4, measuring position X=33, Y= 200 mm, bed expansion E_b = 0.733

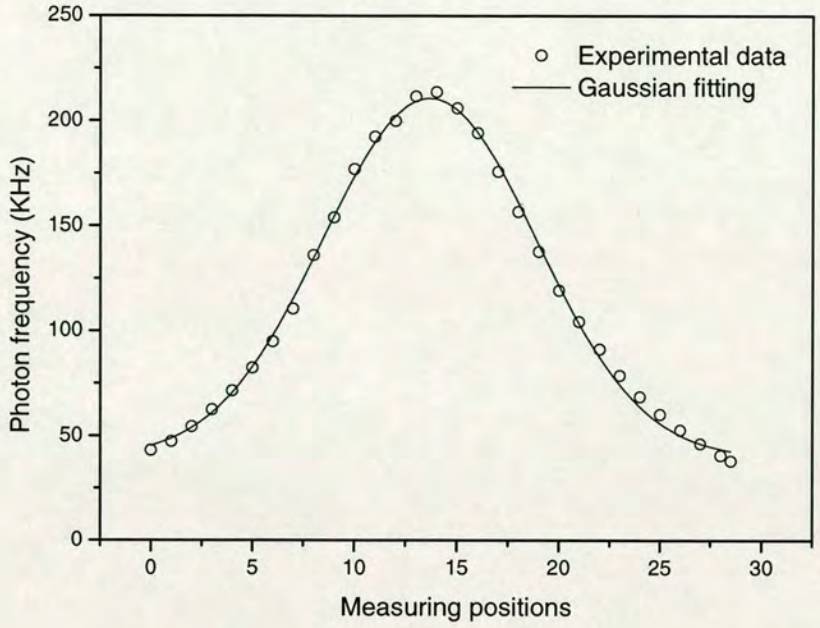

Figure 5.7 The transmission measurement results from the reference latex sample. The measuring position was in the centre of the rectangular cell.

To provide a consistent incident light source, the laser producing system was turned on and warmed up for at least one hour before the first data collection. Usually the laser power was stable, but it was difficult to adjust due to the coarse scale and control screw available. Direct readings of laser power were approximate: two direct readings of laser power from the scale might correspond to different laser powers on successive days. This was also confirmed by digital autocorrelator measurements that counted the quantity of transmitted photons encountered by the fibre detector. To remove the laser power drift effect, a cell filled with a latex emulsion was used as a reference sample to standardize the intensity data measured at different laser powers from day to day. The transmission of the standard cell was measured repeatedly. Thus we were able to measure only the ratio of the transmission of the sample cell to a standard cell. In the DWS experiments, the fluidized bed optical transmissions were calibrated by comparing the transmitted intensity with that of the latex sample.

Repeated measurements at the same thickness indicated that transmission measurements obtained in this apparatus fluctuated by ~5%. This systematic uncertainty dominates the error bars in Figure 5.8 and Figure 5.9.

5.1.2 Measuring conditions

Total transmissions of five fluidized beds (Table 4.1) were measured at three gas superficial velocities corresponding to three bed expansions. Under each gas superficial velocity, 9 to 15 positions across the fluidized bed width were studied at three heights. The results showed that the transmissivity varied little at the same horizontal positions, but changed sharply with height. To simplify the problem, we treat the transmissivity as a function of gas superficial velocity/bed expansion and height in the bed, but assume that it is constant at the same height. The three fractional bed expansions studied were $E1$=0.385, $E2$=0.538 and $E3$=0.733.

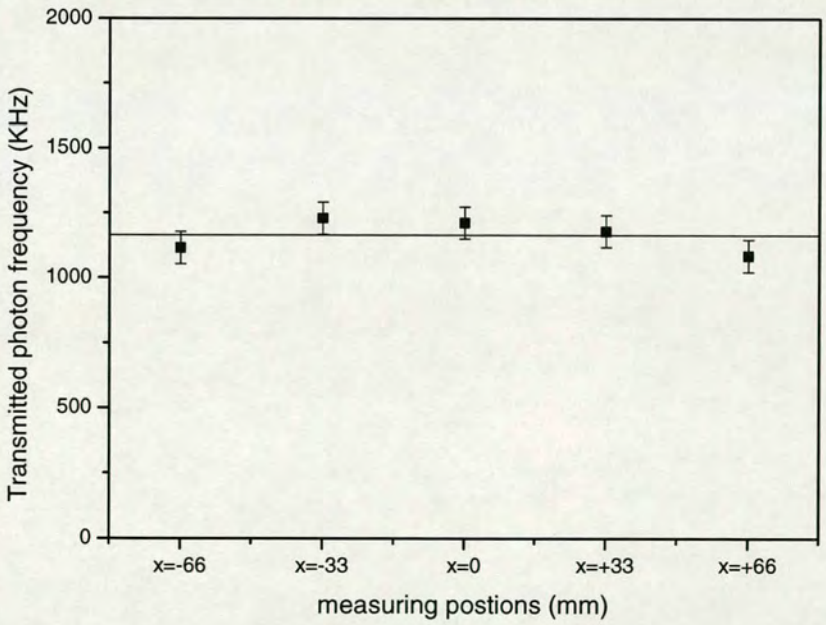

Figure 5.8 Intensity remains constant at the same measuring height.
h_m=110 mm, bed expansion E_b=0.73, Fluidized bed No.3

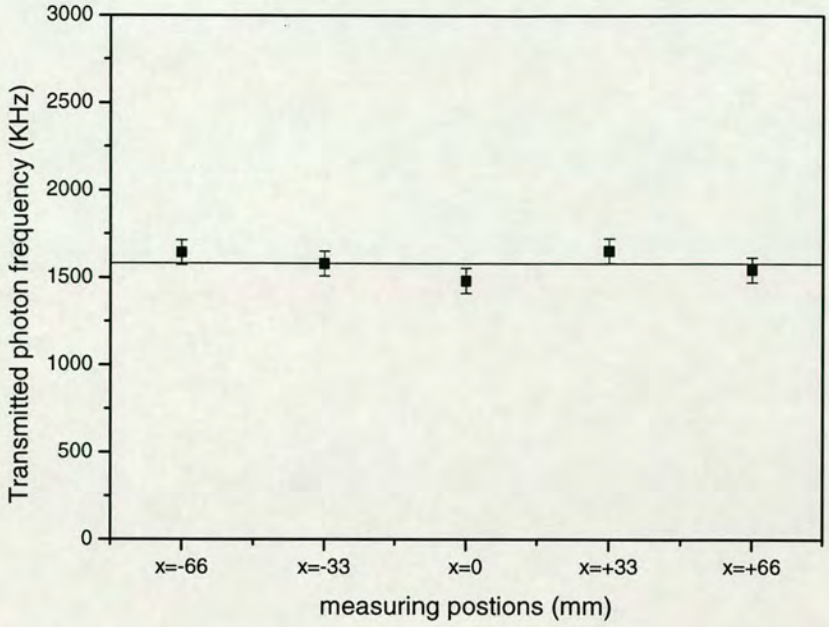

Figure 5.9 Intensity remains constant at the same measuring height. h_m=100 mm, bed expansion E_b=0.54, Fluidized bed No.3

5.2 Calculation of l^* and l_a

5.2.1 Theory background

$l^*$and l_a are two important parameters in the calculation of particle movement properties from the results of DWS experiments. The transport mean free path, l^*, which is the distance that a photon must travel before its direction is completely randomized, characterizes the scattering medium itself.

In any DWS experiment there will always be some absorption. The absorption alters the effective path length by attenuating the longer paths. One way to treat this problem theoretically is to include an absorption term in the diffusion equation for light. The absorption length, l_a, which is used to characterize the absorption of the study objects, is needed to process the results from strongly absorbing materials.

By simply replacing $P(s)$ with $P(s)\exp(-s/l_a)$ in equation (4.17) for $g_1(t)$, the autocorrelation functions could be derived in an otherwise similar way.

First, the l^* and l_a measurement of a reference sample was obtained. The sample, a suspension of latex beads, was contained in a rectangular glass cell of much larger lateral dimensions (10 cm × 10 cm) than depth (2cm).

The method in the reference [111] was used to determine the l^* and l_a in our gas-solid fluidization system. Equation 4 in reference [111] was applied to analyse both parameters:

$$T(L)=\frac{\sinh\left(\gamma l^*/l_a+\varepsilon_b\right)\sin\left(\varepsilon_b\right)}{\varepsilon\sinh\left(L/l_a+2\varepsilon_b\right)} \tag{5.1}$$

$$\text{where } \varepsilon_b=\frac{1}{2}\ln\left[\frac{1+\beta l^*/l_a}{1-\beta l^*/l_a}\right] \tag{5.2}$$

For a weakly absorbing dilute latex system,

$$T_1(L)=\frac{1}{L+2\beta l^*} \tag{5.3}$$

For a strongly absorbing system, a simple but very good approximation for $T(L)$ reads:

$$T_2(L)\approx\frac{l^*}{l_a}2(\beta+\gamma)\frac{1}{1+2\beta l^*/l_a}e^{-L/l_a} \tag{5.4}$$

$$\beta=\frac{2(1+R)}{3(1-R)} \tag{5.5}$$

where R denotes the reflection coefficient of diffusing waves and the parameter γ is expected to be in the order of 1 at the point where light starts to diffuse.

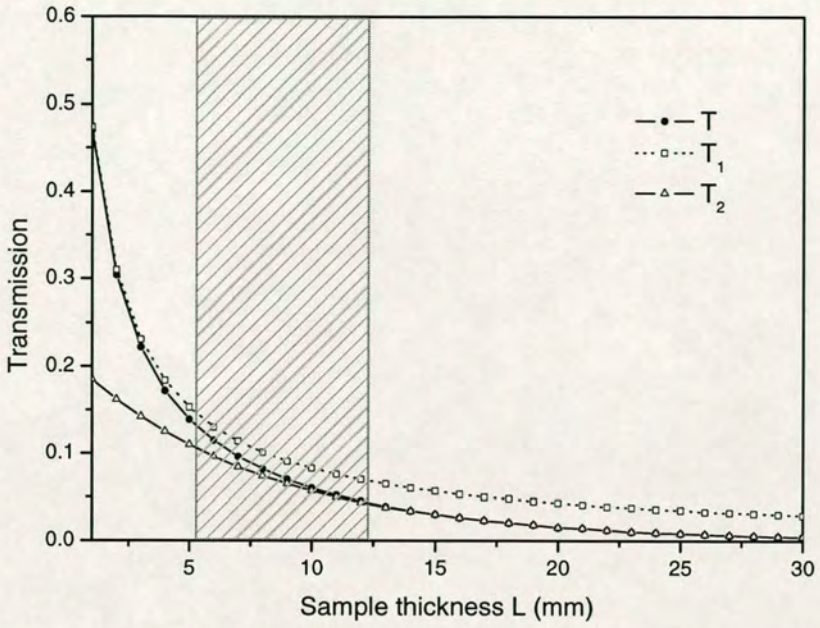

Figure 5.10 Comparison of different transmission equations. The thickness of the fluidized beds used in DWS experiments lay in the rectangular area.

The thickness of the fluidized beds in our experiment is from 5.44 to 12.07 mm. In this range we found that neither of the simplified equations (square and triangle curves in Figure 5.10) was valid. Thus full expression of transmission (eqn. (5.1), circle curve in Figure 5.10) was used in the evaluation of l^* and l_a.

5.2.2 Parameter γ

In DWS theory, the distance over which the incident light is randomized is defined as z_0.

$$z_0 = \gamma \cdot l^* \tag{5.6}$$

As γ is a constant in eqn.(5.1). in the transmission measurement, it will not introduce errors. Two γ values, 1 and 5/3 are usually used to describe the light diffusion in the medium [82, 95]. There were almost no differences between these two γ values for total transmission measurement, as shown in Figure 5.11.

For our DWS experiments, γ is also a non-sensitive parameter that will not change the autocorrelation functions dramatically. As shown in Figure 5.12, we found that the difference in autocorrelation function between $\gamma=1$ and $\gamma=\frac{5}{3}$ was very small.

In DWS theory, z_0 is defined as the distance over which the incident light is randomized. In most cases of our experiment, this distance was much smaller than the sample thickness L ($z_0/L<0.06$). This small distance will not dominate the whole light diffusion process in the fluidized bed. Thus in the data analysis the difference between these two values of γ is ignored.

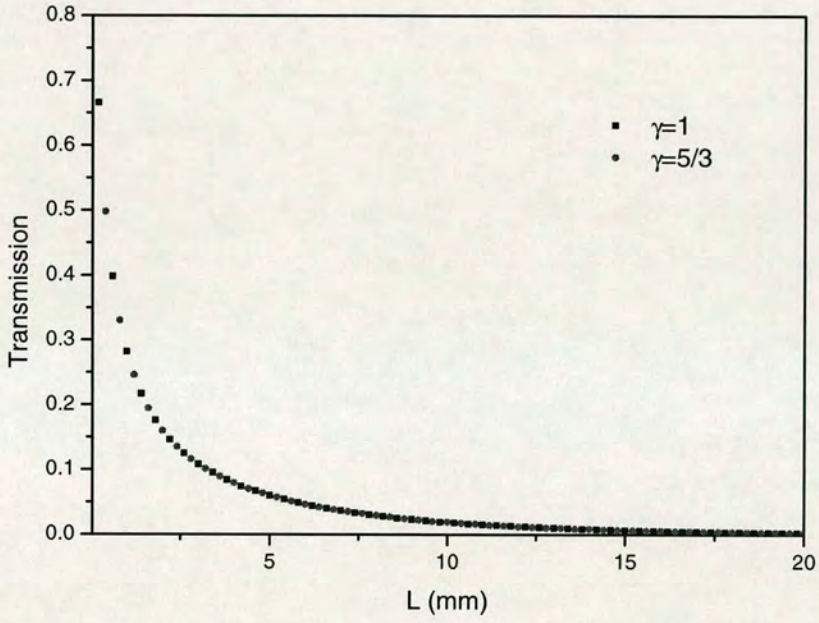

Figure 5.11 Effect of γ on the total transmission

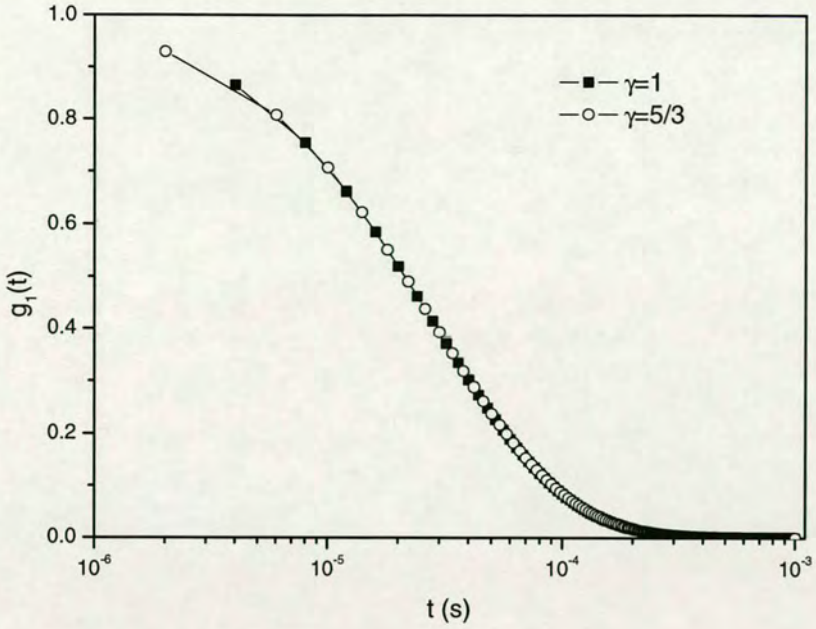

Figure 5.12 Effect of γ on the autocorrelation functions in the DWS.

5.2.3 Reflection coefficient *R*

The reflection coefficient *R* of diffusing waves in eqn. (5.5) is a crucial parameter in the DWS analysis when there are large differences between two interfaces of sample cell. The indices of refraction of sample solvent, sample cell material and cell surrounding medium are rarely matched. Kaplan et al.[112] studied polystyrene spheres with diameters of 205 and 460 nm. Their sample cells were immersed in water and surround by air respectively. They estimated that the reflection coefficient in water is ~0.02 (water-glass-water), while the coefficient in air may have been as large as 0.10 (water-glass-air) [112]. In our experiment, when the standard latex sample was surrounded by air, for this situation *R*~0.10, while for the fluidized bed which is also surrounded by air, the reflection coefficient of (air-glass-air) would have been near 0. We can ignore this effect in our experiments.

5.2.4 l^* and l_a results

Transport mean free path was measured at three bed expansions. Transmission was measured at several positions in the fluidized bed and the transport mean free path l^*

was determined from eqn.(5.1). The results are shown in Table 5.1. In Table 5.1 it may be seen that l^* increases with bed expansion and measuring height. (Position1 measuring points are near the base of the fluidized bed, Position2 points are near the middle of the bed and Position3 points are in the top part of the bed).

Table 5.1 l^* at different positions under different bed expansions

E_b (Fluidized bed expansion)	Transport mean free path l^* (mm)		
	Position1	Position2	Position3
0.385	0.1219	0.1480	0.2106
0.538	0.1428	0.1871	0.3713
0.733	0.2158	0.2838	0.7010

In Figure 5.13 l^* has been fitted by polynomial equations. l^* increases slowly with height when the gas velocity is small, but changes quickly when the bed expansion is high. Values of l^* at other heights and bed expansions were obtained by interpolation. In the experiments values of l_a were between 3.42 to 4.8 mm (Figure 5.14). It is treated as a constant in the data analysis. These data will be adopted in the analysis of granular temperatures in Chapter 6.

For fluidized bed No.3, these expansions corresponded to the following superficial velocities: 4.8, 6.2 and 7.2 mm/s.

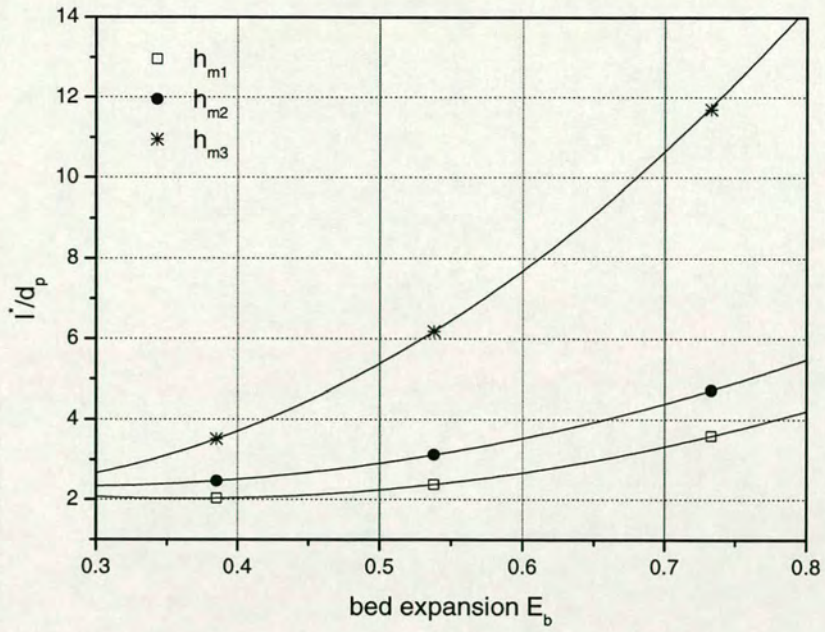

Figure 5.13 Transport mean free path l^* versus bed expansion

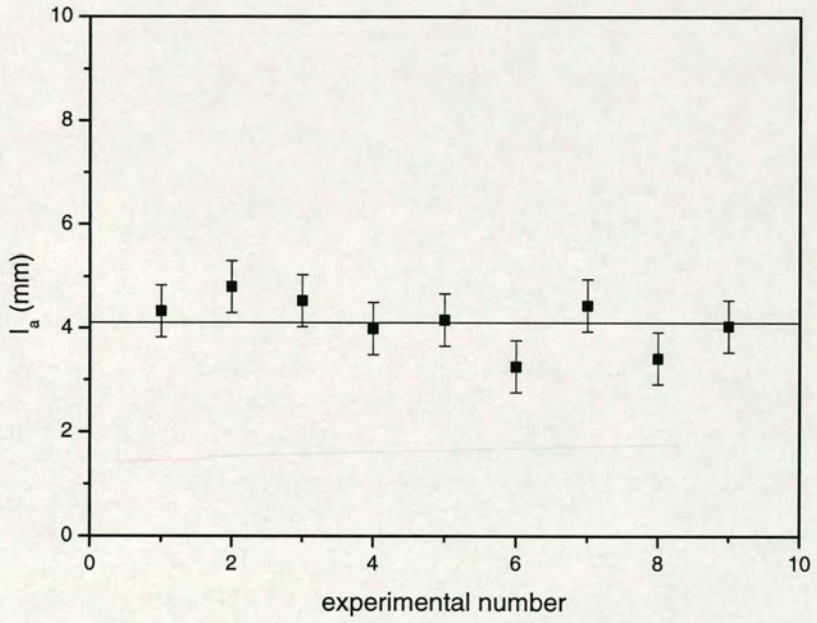

Figure 5.14 Absorption length from total transmission measurement

5.3 Measuring geometry and position studies

As mentioned in Chapter 3, there are two geometries used in the DWS measurements: transmission and backscattering. Depending on the experimental situation, different

geometric configurations were applied to collect particle movement information in different parts of the fluidized bed.

5.3.1 Transmission and backscattering geometries

In the transmission experiment, the light is incident on one side of a sample of thickness L and is detected on the opposite side by the transmission fibre detector. Transmission geometry is simpler to interpret than backscattering geometry because all paths through the sample are long compared with l^* and are therefore accurately described within the photon diffusion approximation.

Another geometry commonly used in DWS experimentation is data gathering using backscattered light. The fibre detector was put on the same side of the bed as the incident light to collect back-scattered radiation. This geometry is very convenient because it requires access to the sample from only one side, which can be particularly useful in industrial situations. Another advantage of backscattering geometry is that it does not require independent knowledge of the transport mean free path in order to interpret the autocorrelation function.

Autocorrelation functions from both geometries have been studied.

5.3.2 Detector positions

Figure 5.15 presents different detector positions in the experiments. For transmission geometry, the distance between the fluidized bed and detector fibre is not crucial to the autocorrelation function results since the scattered light propagation does not change after it travels through the fluidized bed and before it arrives at the detector if there is no aperture, filter or polarizer before it. (Case II in Figure 5.15)

By adjusting the FB position when the incident light is not normal to the fluidized bed, a reflected spot that does not coincide with the incident light could be found in the last mirror which was used to adjust the light route (Case III in Figure 5.15). Small differences in the autocorrelation functions could be found at long time delays,

as shown in Figure 5.16. Although the difference is small, it is better to adjust the incident light to be normal to the fluidized bed to fulfil the assumptions of the DWS model. To collect at the maximum intensity of the scattered light, the detector was usually adjusted to the position corresponding to the centre of the scattering area.

For the backscattering geometry, this detector position is crucial to the measurement of the autocorrelation function. By adjusting the measuring angle of the fibre detector, a maximum intensity position could be found which should correspond to a study region at the centre of the scattering area.

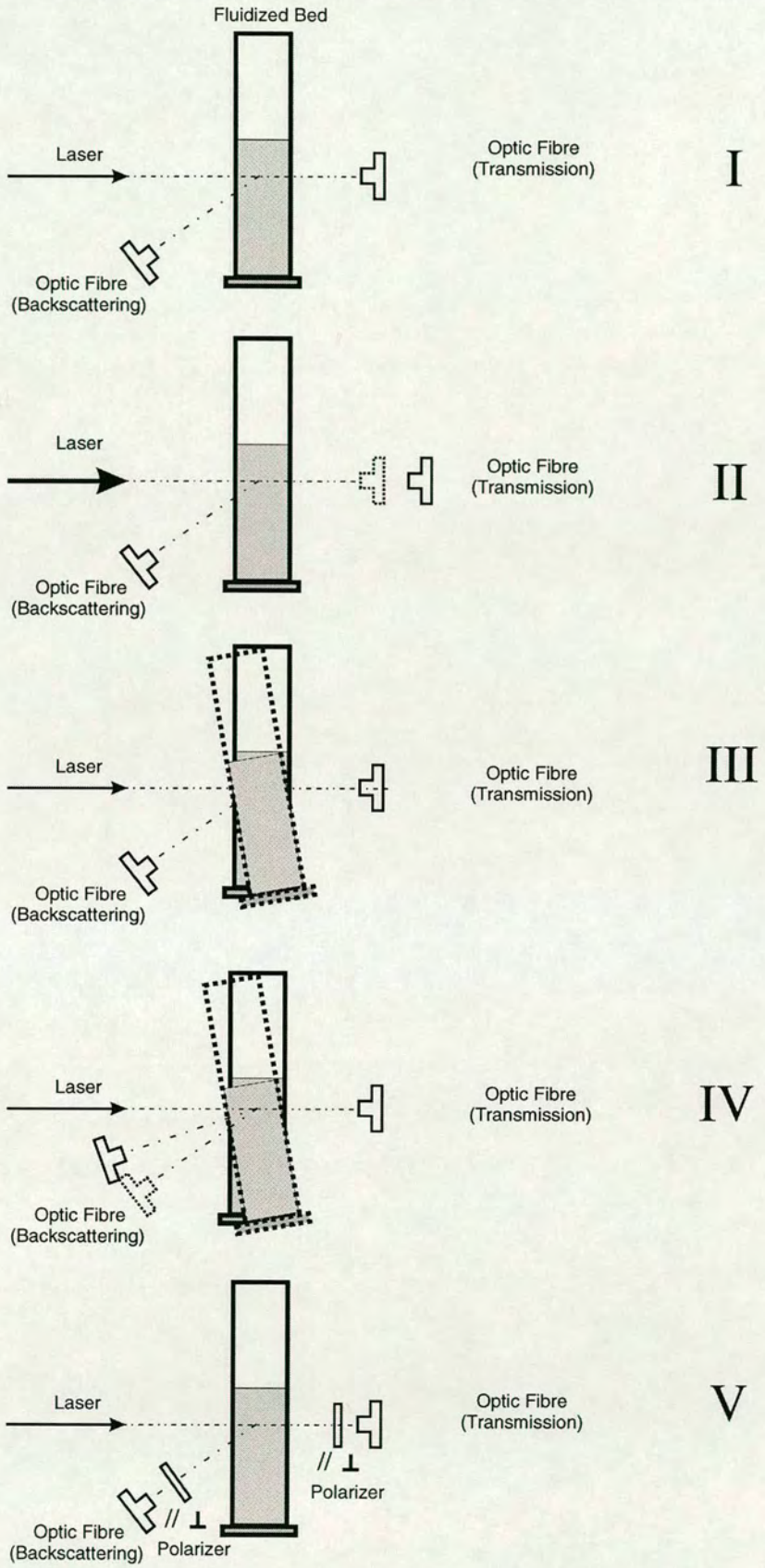

Figure 5.15 Different measuring configurations

If the measuring position is far from the position of maximum intensity (the scattering area), what DWS studies will not be the scattering area, but another area of uncertain position. Further, in that region the multiple scattering approximation might not be valid since less light diffuses to it. It can be seen in Figure 5.18 and Figure 5.19 that, when the fibre was put far from the centre of the laser reflection position, the transmitted light intensity received was relatively low and its autocorrelation function was significantly changed. In backscattering measurement, it was important to control the detector position. This could be done by adjusting both fluidized bed position and fibre detector angle. (Case IV in Figure 5.15)

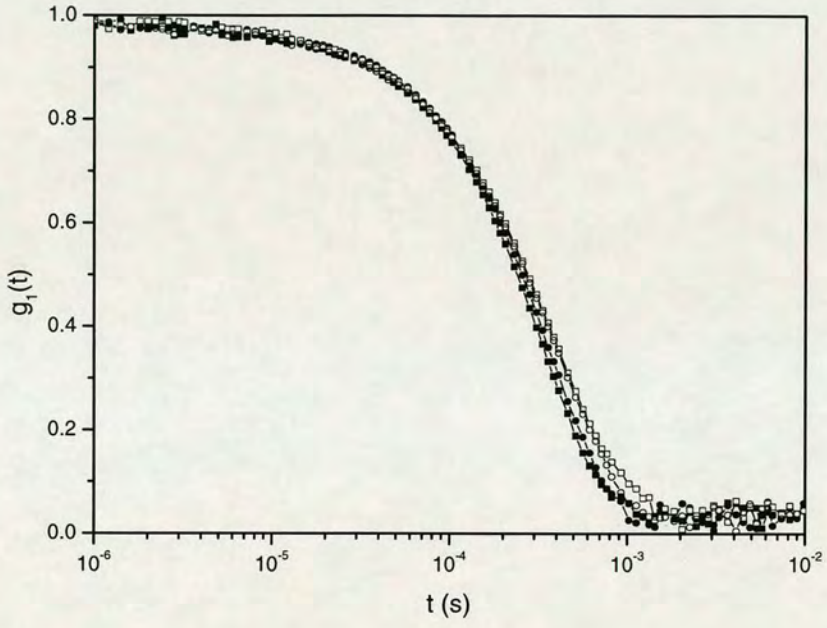

Figure 5.16 Transmission measuring position study. ■: FB at original place; ●: FB moved closer to the fibre; □: FB moved further to the fibre; ○: reflection not perpendicular to the FB.

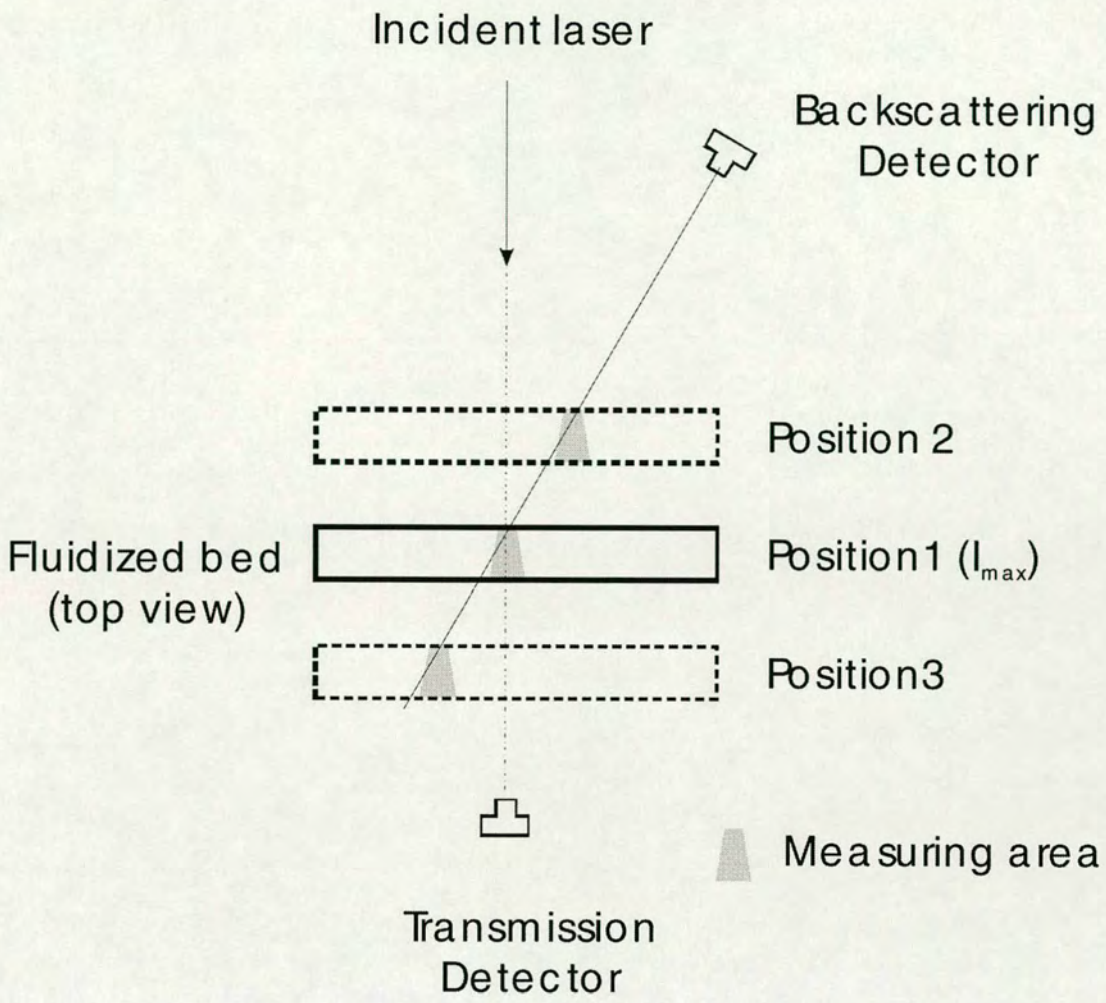

Figure 5.17 For backscattering measurements the fluidized bed position is crucial. At position 1 the detector received the strongest light intensity. Its region of study is the same as for transmission measurement. When the fluidized bed was moved to position 2 and position 3, although we still could receive backscattered light, the regions of study were different from those in transmission measurement.

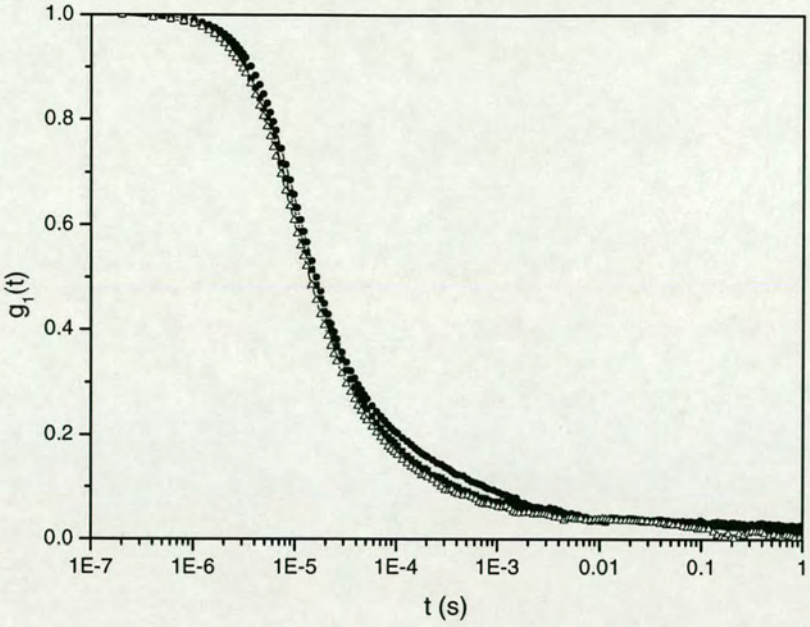

Figure 5.18 Autocorrelation function at different measuring positions (backscattering geometry) ■: intensity=112KHz, ●: intensity=391KHz, □: intensity=120KHz

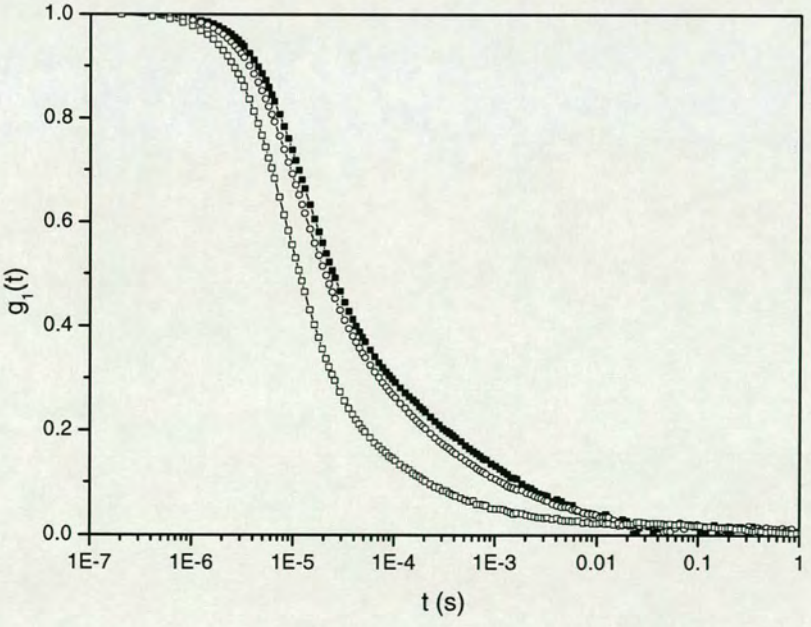

Figure 5.19 Autocorrelation function at different measuring positions (backscattering geometry) ■: intensity=430KHz, ○: intensity=430KHz, □: intensity=180KHz

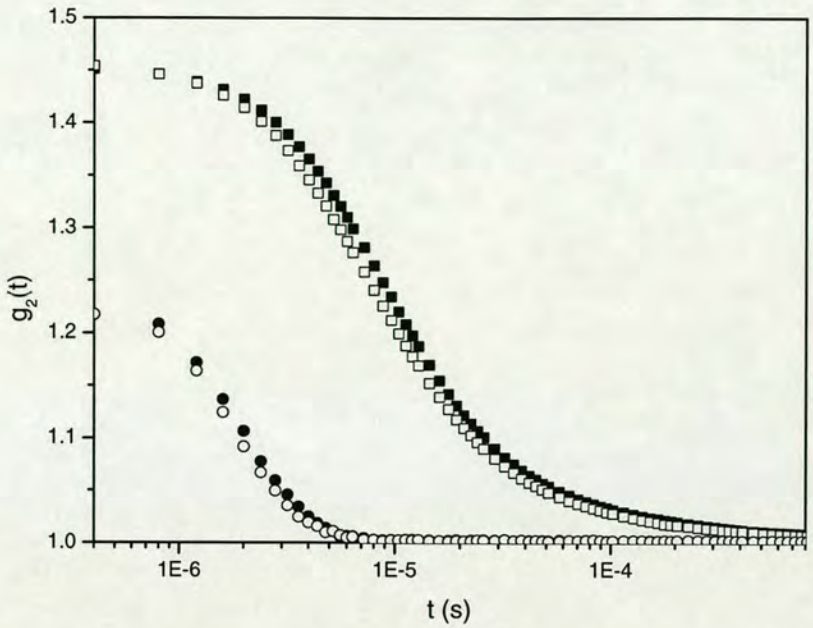

Figure 5.20 Exchange fibre detectors. ■ and ●: transmission and backscattering autocorrelation functions, □ and ○: transmission and backscattering autocorrelation functions after exchanging fibre detectors.

In our application of DWS, the transmission and backscattering fibre detectors were made by different manufacturers. A test experiment was done by exchanging two detectors. From Figure 5.20 we found the four autocorrelation functions were unchanged; this proved that the two geometry configurations in the DWS experiments are reliable and their system errors are the same.

5.4 Laser power effect

As discussed in section 5.1, the laser power direct reading is not accurate due to the coarse scale and adjustment screw. Usually the DWS measurement will start at least one hour after the laser system has warmed up. To ensure that all the measurements were taken under the same conditions, adjustments of laser power during the measurement were avoided. When the sample was not transparent or semi-transparent, a powerful laser was needed to illuminate the sample. Under this condition usually point laser sources were preferred since an expanded light source needed a much more powerful laser source to create a strong enough signal to be

detected by the optical fibre. Yet sometimes, because the optical properties varied across the thickness of the object studied, the laser power had to be increased to achieve a high enough signal/noise ratio, or to be decreased to protect the fibre detector from burning out for thin samples. A too powerful laser might not only damage the detector but also heat the sample, adding more experimental uncertainties. The laser power effect is discussed below.

Table 5.2 Laser power values in DWS experiments.

Experiment No.	Laser power
250203	0.05
250204	0.10
250205	0.15
250206	0.20
250207	0.25
250208	0.30
250209	0.50

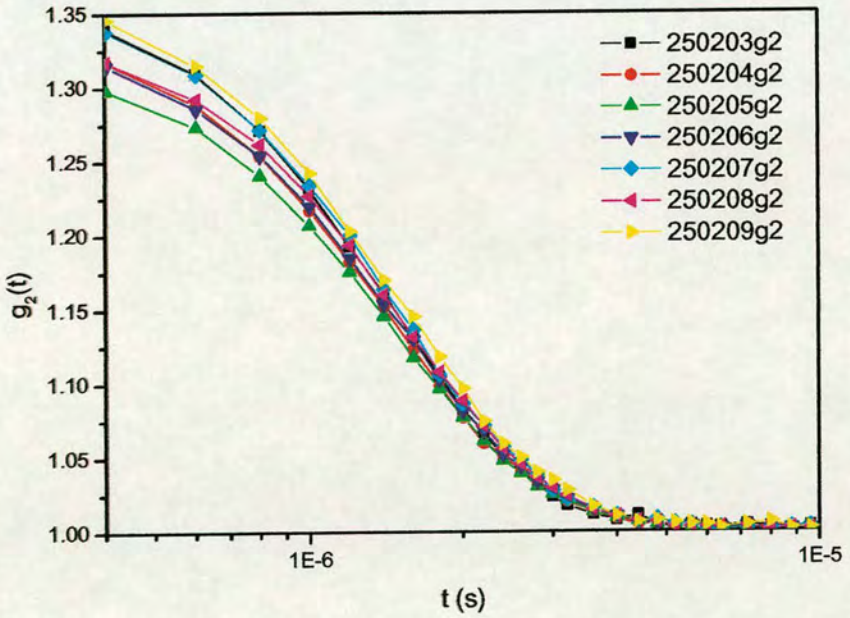

Figure 5.21 Laser power effect on the autocorrelation functions. Differences could be found at short autocorrelation times.

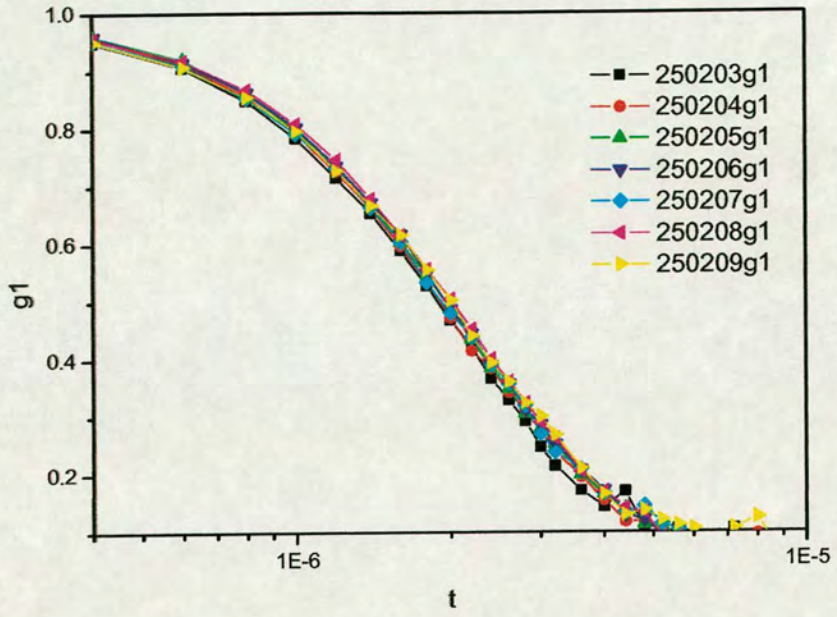

Figure 5.22 Laser power effect on the autocorrelation functions. After $g_2(t)$ was transformed to $g_1(t)$, the electrical field autocorrelation functions were almost identical.

Changing the laser power will affect the photon intensity directly. It is important in the transmission measurement but not critical to the DWS autocorrelation functions. As in Figure 5.21, the intensity autocorrelations $g_2(t)$ change slightly, but when they are converted to electrical field autocorrelations $g_1(t)$ they remain the same (Figure 5.22).

5.5 Polarization effects

Transmission and backscattering measurement with and without a polarizing filter were studied.

For the transmission geometry, as in Figure 5.24, a lot of fluctuations could be found at short time delays when a polarizer was added just before the fibre detector. They might have been caused by the following reason:

The laser light was multiply scattered by the particles in the fluidized bed. After the laser passed through the fluidized bed, the photons would have random movement in all directions, but only those with the same direction as the polarizer (a very small fraction of the total) would be received by the fibre detector, especially at short times which corresponded to those 'maximum scattered' photons travelling the longest distance in the fluidized bed. Due to the low photon frequency collected by the detector, there would be fluctuations at short time because of the low signal to noise ratio. Since the transmitted light received by the detector had already travelled over a path at least equal to the thickness of the sample, the photons must have been scattered multiply before they encountered the detector fibre. It is not therefore recommended that a polarizer should be used in the transmission geometry because it would decrease the scattered light intensity dramatically. In some situations, when the scattered light intensity was still very high, to protect the detector, a size-adjustable pinhole would be put before the fibre to collect only a small portion of the scattered light.

In reflection (backscattering) geometry, some of the photons received by the detector would have been scattered only a few times, which might violate the multiple scattering approximation. To avoid collecting these photons, a polarizer perpendicular to the laser polarization angle was added before the detector. After the (polarized) laser light was introduced to the fluidized bed, the photons were scattered by the particles in the bed. The scattered light would propagate in every possible direction, but only those parallel to the polarizer, which has a phase change, would pass through it and be collected by the fibre detector. The photons scattered along short paths would preserve polarization to a large extent, and so would be filtered by the polarizer and not be detected by the fibre.

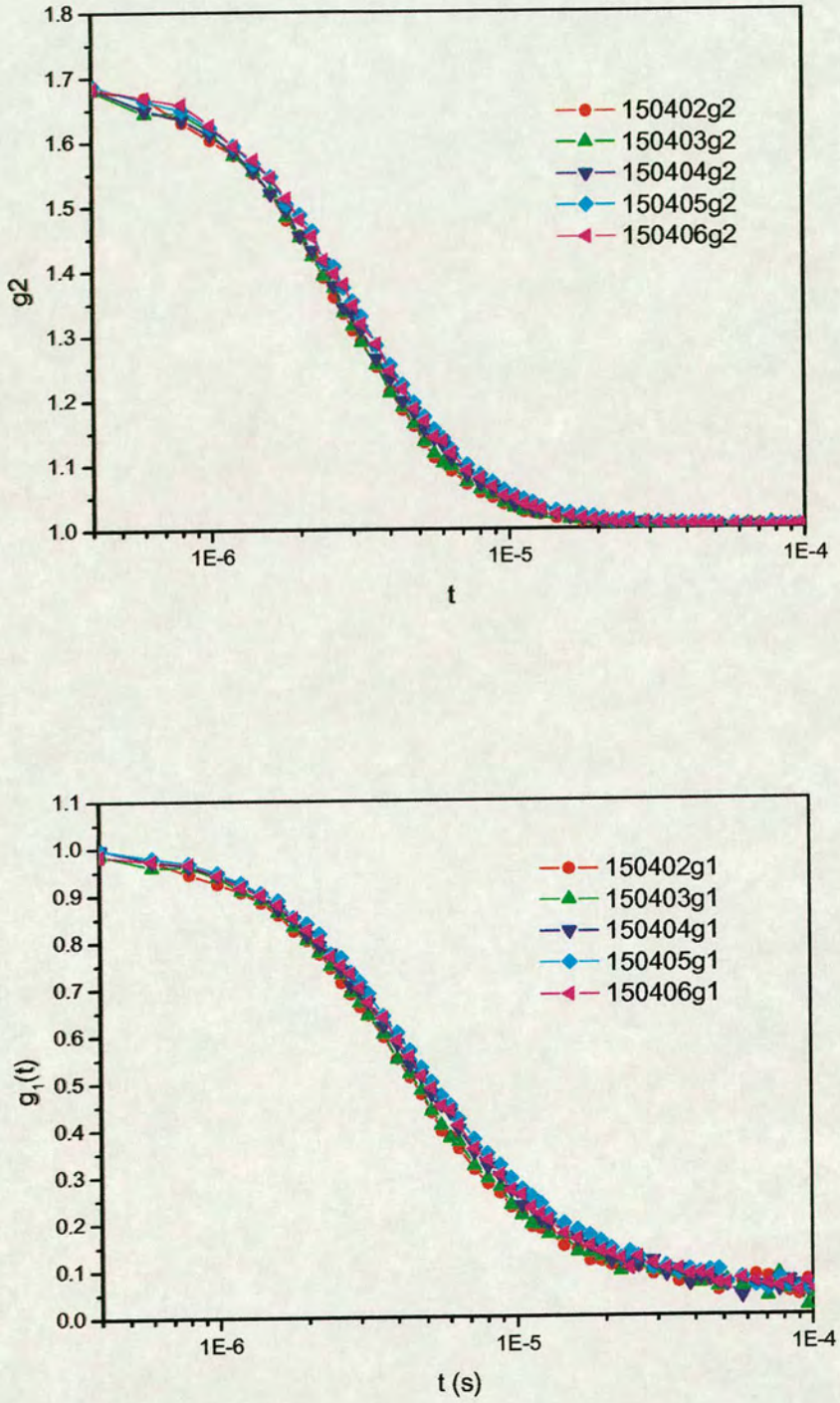

Figure 5.23 Autocorrelation functions from different polarization angles. (Transmission geometry). The polarization angle is 0°, 30°, 45°, 60°, 90° in experiments 150402 to 150406.

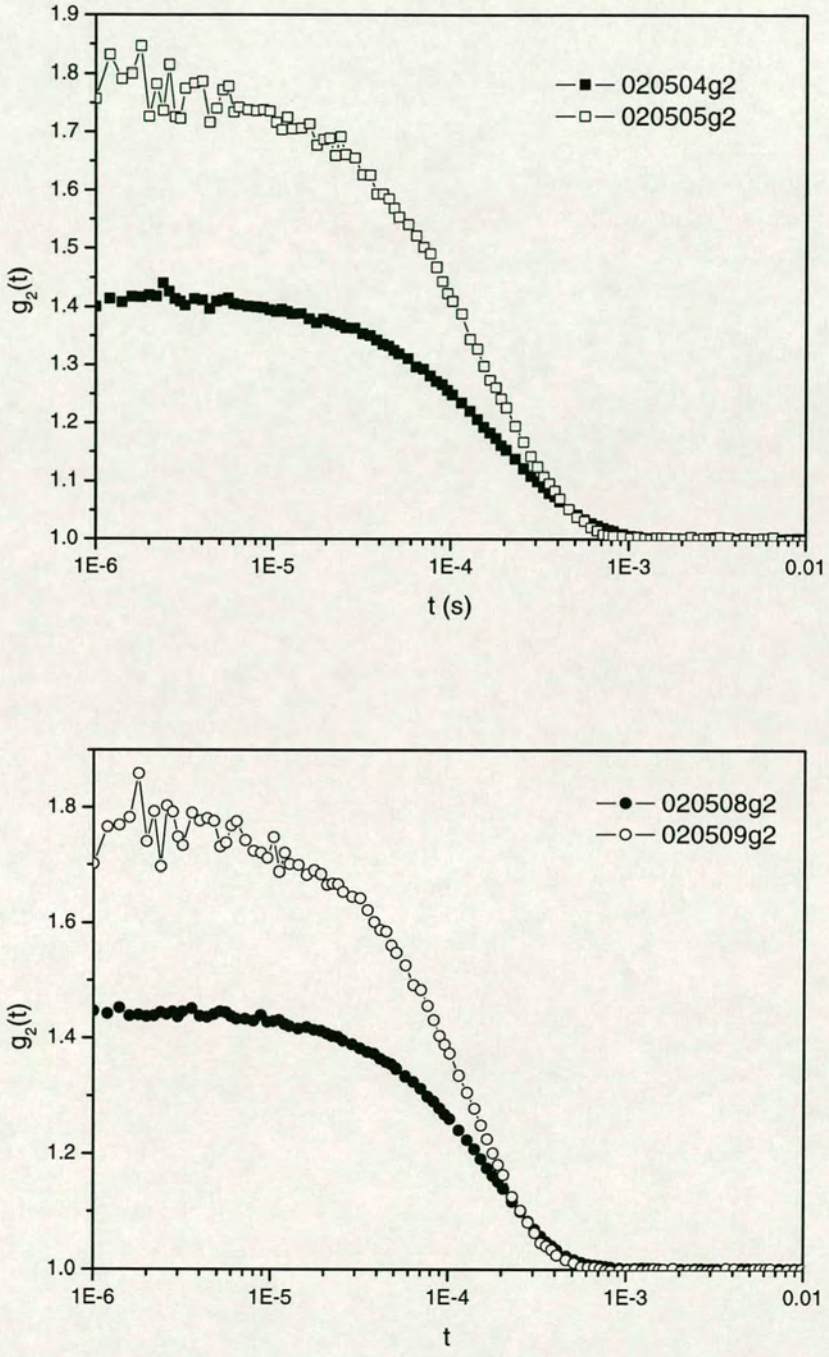

Figure 5.24 Fluctuations could be found in the transmission geometry with the polarizer at short autocorrelation time. Polarization angle -♦-: 0 °, -o-: 90°.

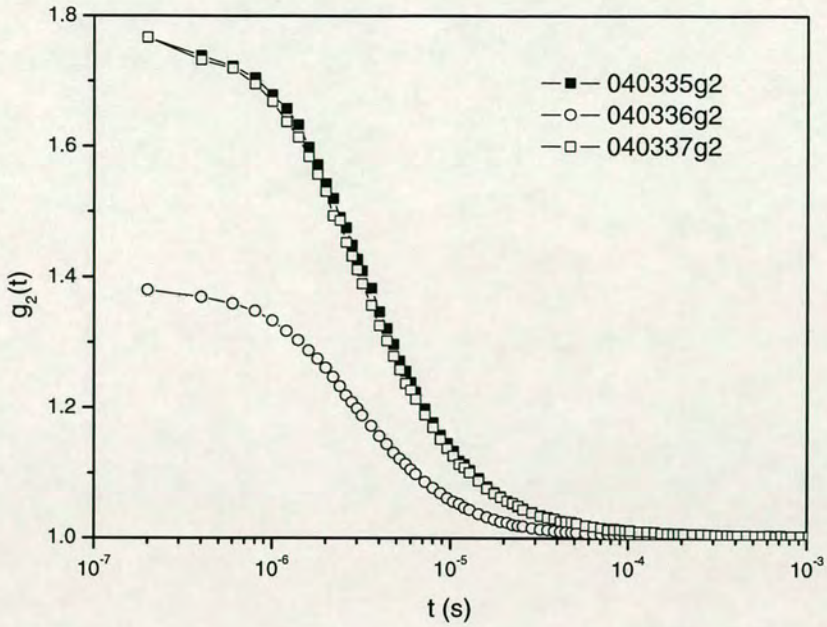

Figure 5.25 Under backscattering geometry, intensity autocorrelation functions varied with different polarizer angles. ■: vertical polarization, ○: without polarizer, □: horizontal polarization

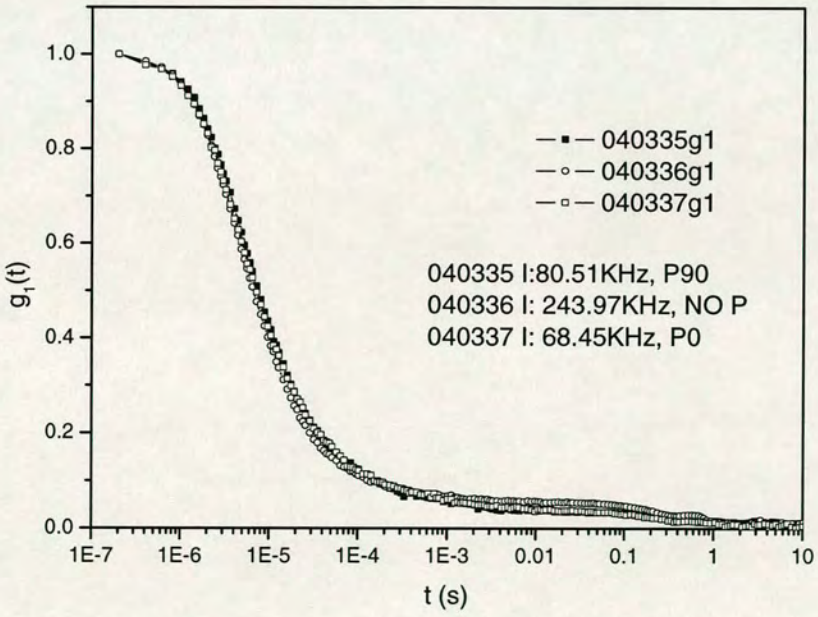

Figure 5.26 After being transferred to electrical field autocorrelation functions under backscattering geometry, they remained the same with different polarizer angles. ■: vertical polarization, ○: without polarizer, □: horizontal polarization

Autocorrelation functions under backscattering geometry with differing polarizer angles are compared in Figure 5.25 and Figure 5.26. Three cases are studied: without polarizer, polarizer parallel or perpendicular to the laser direction (vertical). We found that intensity decreased when the polarizer was added, since only light with the same direction would reach the detector. There is no large difference between the three electric field autocorrelation functions, which means that in our experiments only small amount of light were not multiply scattered when they reached the fiber detector. Although usually a polarizer was put before the backscattering detector to ensure that only multiply scattered photons were received by the fiber, this system configuration was not used when the reflecting intensity was low.

5.6 Conclusions

Firstly a total transmitted light intensity measurement method was studied. Results show that the total transmitted light intensity follows a Gaussian profile and varies with bed thickness and fluidized bed expansion. Transport mean free path and absorption length were determined by measuring total transmitted light intensity under different fluidized bed thicknesses, bed expansions and measuring positions. Transport mean free path increased with bed expansion. At higher measuring positions, larger transport mean free paths were found. Absorption length was treated as a constant in the experiment. The effects of different measuring geometries, detector positions, laser powers and polarization angles to the autocorrelation functions were studied.

Chapter 6 Granular temperatures in the fluidized bed

DWS is a multiple scattering technique that yields two particle correlation functions at time intervals greater than 10^{-8} s and length scales of 0.01 to 1 μm [77]. As mentioned in the previous chapter, Menon et al. [44]have studied particle motions in the gas-fluidized bed under different gas superficial velocities by DWS. In their work, they used solid glass beads of averaged diameters 49 μm, 96 μm and 194 μm. The fluidized bed used in their study had a 6 cm × 6 cm square cross section. With these dimensions and with solid glass beads as filling materials, only backscattering DWS could be used. In our project, we also used DWS to study a gas-solid fluidized bed. However, the fluidizing materials in our research were hollow glass beads with semi-transparent optical properties Transmission DWS was able to be applied when this kind of material was fluidized in a two-dimensional bed. More importantly, because Menon et al used Geldart group B solid glass beads (density = 2500 kg/m^3) as fluidizing material, the bed expansion before minimum bubbling was very small (less than 12%), so the velocity difference between minimum fluidization and minimum bubbling was negligible, especially for their large glass beads. The low effective density Q-Cel® 5020 particles which were used in our experiment presented Geldart A fluidization behaviour and the bed could be easily expanded to >50%. The distinctive particulate fluidization and large bed expansion provided us with a wide range of fluidization state to study particle micro-dynamics with both transmission and backscattering DWS techniques. In all DWS experiments, light was multi-

scattered in the fluidized bed and no localization phenomena observed so the first approximation of DWS theory [95] was always valid. Based on the second approximation [95], a plot like Figure 3.7 was always used to determine average granular temperature in the cylindrical region (Figure 5.1).

6.1 Granular temperature at a fixed position under different gas superficial velocities

Using DWS, granular temperatures at a fixed position under varying conditions of gas superficial velocity were studied first.

In our first experiment, as shown in Figure 6.1, a position on the centre line at about h_m=140mm above the gas distributor was studied. The reason why such a position near the gas distributor was selected was that we were interested in the particle movement as related to gas velocity. Firstly, if it were too close to the gas distributor, e.g. less than 100 mm above the distributor, it would be difficult to acquire stable and repeatable measurement data even with long measuring times because quantities of coarse bubbles produced from the gas distributor above U_{mb} disordered the flow badly. Secondly when large bubbles appeared, the local voidage was high. The high transmissivity might damage the PMT. In the experiment we found that the signals at heights above 100 mm were in a reasonable range (100-300KHz) and they were stable. One other reason was that the transport mean free path l^*didn't change much near the bottom part of the bed when the gas velocity increased (Figure 5.13). Thus we were able to simply consider the granular temperature at this position as a function of gas velocity only.

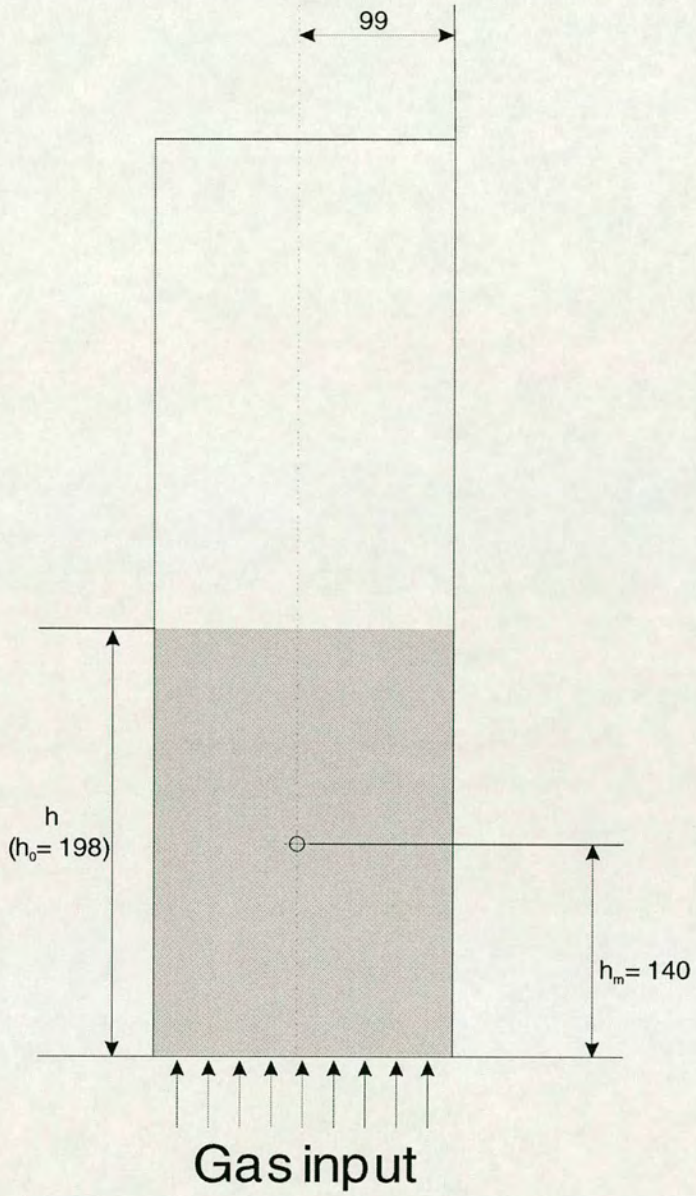

Figure 6.1 Fixed measuring position under various gas superficial velocities.

h_m=140 mm, h_0=198 mm, the bed height h varied from 198 to 330 mm depending on gas velocity

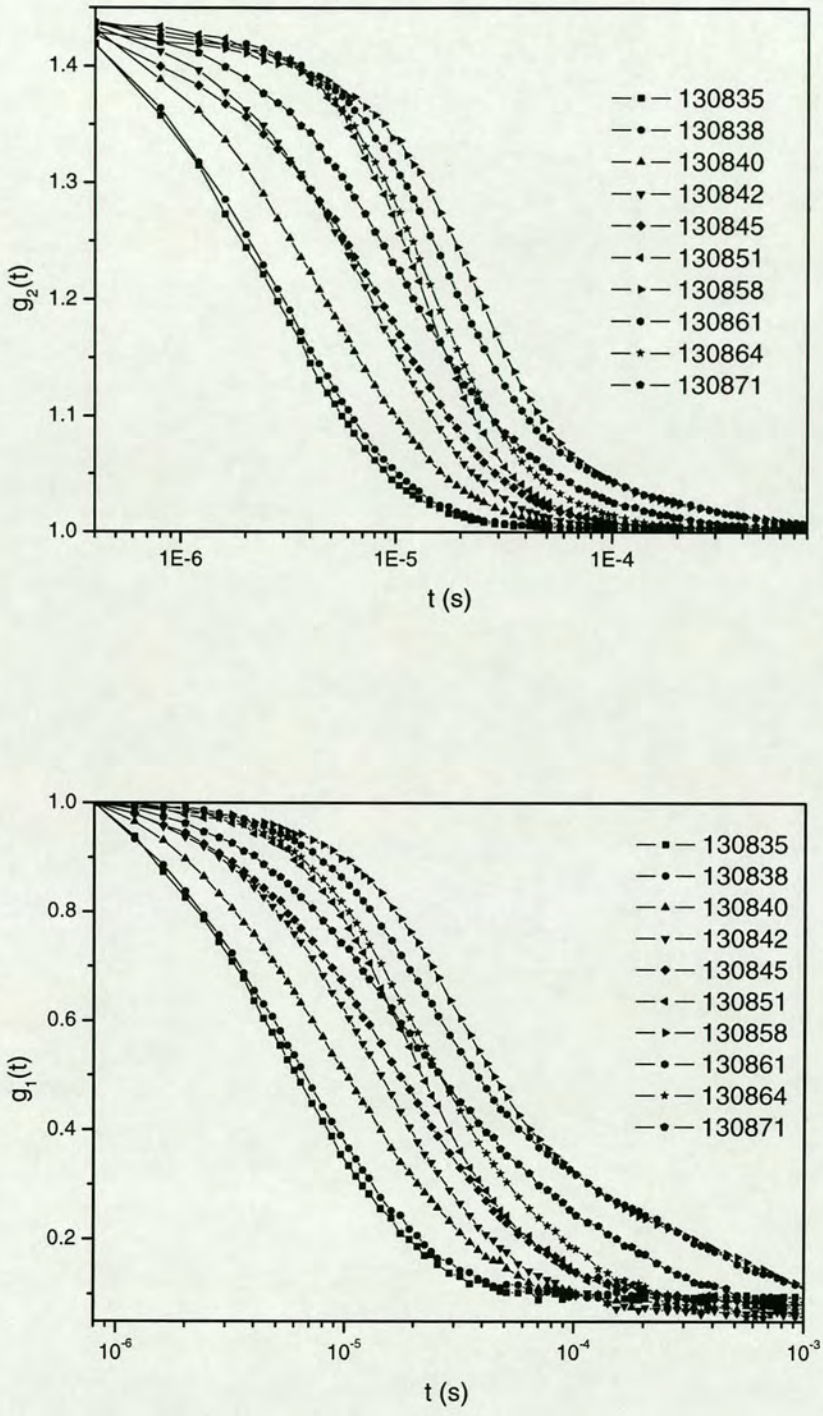

Figure 6.2 Backscattering intensity autocorrelation functions measured at several gas superficial velocities at h_m=140 mm. From left to right, U_s= 5.26, 4.80, 4.35, 3.79, 3.54, 3.13, 2.73, 2.27, 2.02, 1.71mm/s.

Figure 6.2 shows the intensity autocorrelation functions $g_2(t)$ measured at several gas superficial velocities. When the gas velocity increases, the decay time of $g_2(t)$ increased. As shown in the figure the autocorrelation functions shifted from left to right.

Table 6.1 Various gas velocities used in the experiments

Experimental No.	Gas superficial velocity (mm/s)
130835	5.26
130838	4.80
130840	4.35
130842	3.79
130845	3.54
130851	3.13
130858	2.73
130861	2.27
130864	2.02
130871	1.71

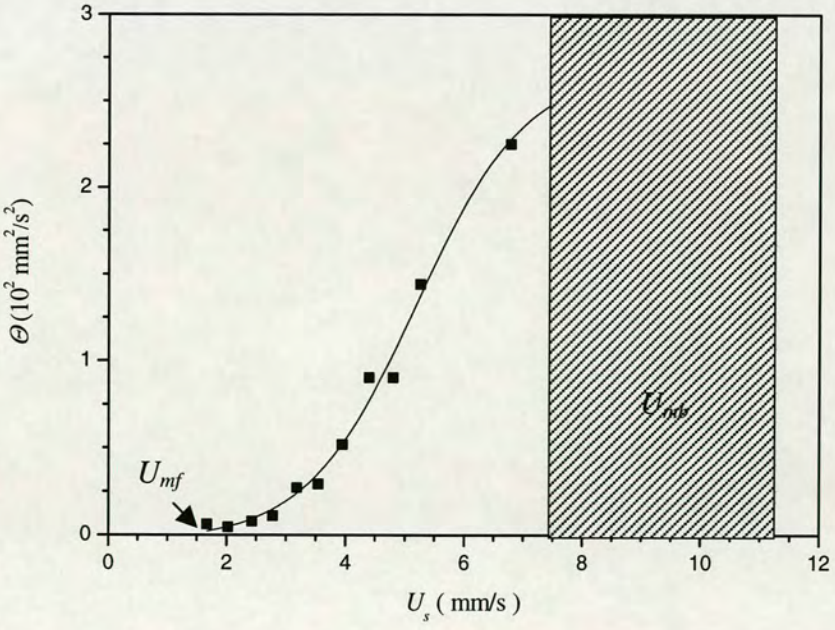

Figure 6.3 Granular temperature at h_m=140 mm under different gas superficial velocities

Figure 6.3 shows a typical plot of the variation of granular temperature with superficial velocity at h_m=140 mm on the centre line of the bed. From Figure 6.3 it can be seen that granular temperatures keep rising with the increasing gas superficial velocity. Menon et al. found the same trend in their work. Their results are averaged for the bed while our experimental results are measured at a fixed position in the fluidized bed. They found zero granular temperature before the onset of minimum bubbling. However in our experiments we successfully measured several non-zero granular temperature points before U_{mb}. At high gas velocity the granular temperature does not increase as quickly as that at low gas velocity. This figure also indicates that the velocity fluctuations are of the same order of magnitude as the gas superficial velocity, consistent with the results of Cody et al.[59] who used acoustic shot noise probes to measure granular temperature in the fluidized beds.

Gidaspow et al. studied maximum carrying capacity and granular temperatures of A, B and C particles, in their paper [113] equation 50,

$$\Theta_{\max} - \Theta_w = \left(\frac{\mu_s}{\kappa} \right)^{-2} \overline{u_s} \qquad (6.1)$$

Θ_w is granular temperature at the wall, μ_s solid viscosity, κ granular temperature conductivity, u_s solid velocity. (Note: μ_s / κ is not a constant here, it is a function of solid volume fraction)

Equation (6.1) shows the reasonable results that at low gas velocities, the granular temperature will be correspondingly low. This agrees with our experimental results above.

Granular temperature can be generated by several mechanisms. One of them can be described as follows: when two particles collide, their resultant velocities will depend not only on their initial velocities, but also on the angle at which the two particles collide, the surface friction at the point of contact, and other factors that may affect the geometry of the collision impulse. Thus, even if the particles initially move with the mean velocity appropriate to their positions within the velocity field,

their resultant velocities will contain apparently random velocity components. The magnitude of the random velocities generated in this mode will be proportional to the relative velocities of the particles at the time of impact and hence must, in an averaged sense, be proportional to the mean velocity gradient within the material. This mechanism agrees well with our experimental results as in Figure 6.3.

The variation of the granular temperature with high superficial velocity can be understood as follows. The energy imparted to the particles by the gas increases with the interstitial gas velocity until onset of bubbling where any further increases in gas flow rate pass through the bed as bubbles rather than through the interstices between the particles. The smallness of the number, size and speed of the bubbles at and 'slightly beyond' the minimum bubbling velocity means they will little affect the particles and, therefore, their granular temperature. Although we do not probe well beyond the minimum bubbling velocity due to the experimental limitations mentioned above, it is reasonable to expect the granular temperature to begin increasing again at higher superficial velocities as the number, size and velocity of bubbles increase, as well as those of their associated particulate wakes. It is, therefore, perhaps more appropriate to view the plateau we observe here as a saddle point between two rising sections. Qualitatively, the variation of granular temperature with superficial velocity seen here is very much in agreement with that of Valverde *et al.* [79] who also only probe up to the minimum bubbling velocity.

6.2 Granular temperature at vertical positions at a fixed gas superficial gas velocity

In a further series of experiments, variations of granular temperature with height at a fixed gas velocity were also studied. Measurements from two series of positions have been taken.

6.2.1 Granular temperature at the centre line of the fluidized bed

Firstly granular temperatures at the centre line of the fluidized bed were measured. As shown in Figure 6.4, a series of positions from h_m= 40 mm to h_m= 260 mm were studied. The distance between each pair of measuring positions is 20 mm.

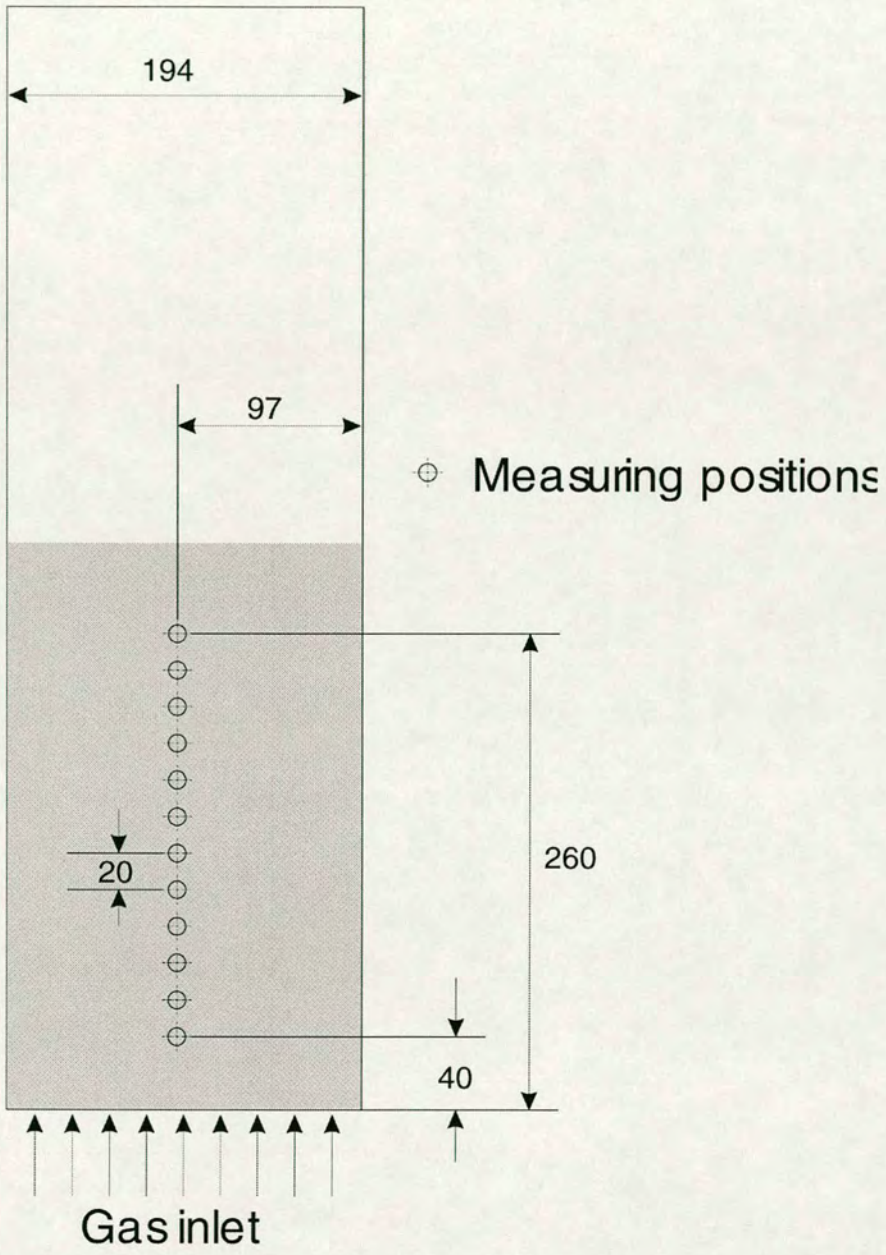

Figure 6.4 Vertical measuring positions on the centre line at fixed gas superficial velocity. The distance between each two measuring points is 20 mm approximately, which is near the laser spot diameter (20-30 mm) after multiple scattering in the fluidized bed.

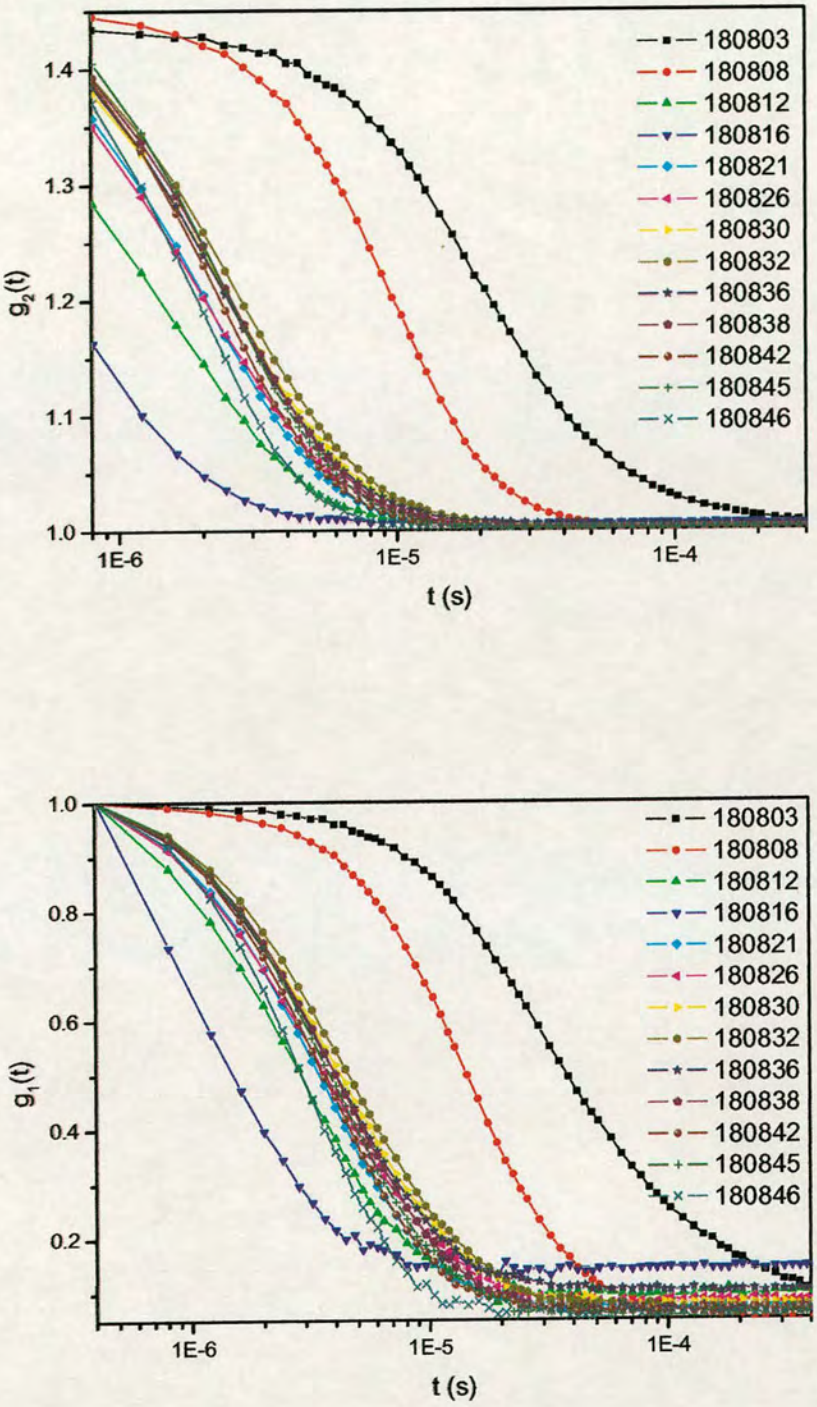

Figure 6.5 Intensity autocorrelation functions measured at several central positions at fixed gas superficial velocities. From left to right, h_m=40, 60, 80,100, 120, 140, 160, 180, 200, 220, 240, 260, 270 mm.

Table 6.2 Measuring heights in the DWS experiments (x = 0 mm)

Experiment No.	Measuring height h_m(mm)
180803	40
180808	60
180812	80
180816	100
180821	120
180826	140
180830	160
180832	180
180836	200
180838	220
180842	240
180845	260
180846	270

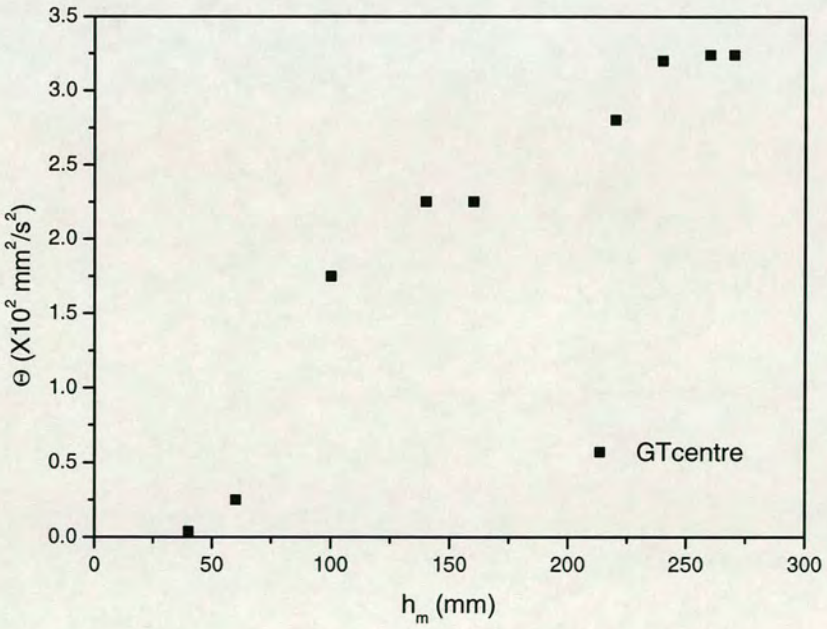

Figure 6.6 Granular temperature on the centre line positions of the bed as a function of height above the distributor at U_s= 7.3 mm/s

Figure 6.6 shows the granular temperature measured at centre line positions. With increases of the measuring height, granular temperature increased as well. From Figure 6.5 it can be seen that the intensity autocorrelation functions shift from right to left with increasing height of measuring position, yet the difference between these vertical positions is very small. On the other hand, different transport mean free paths l^* will affect the particle mean square displacement (MSD) results, which are used to calculate granular temperature, even when the autocorrelation function measurement data $g_2(t)$ are the same (equation 3.29 and equation 3.30). In our case because the transport mean free path l^* increases with the measuring height, this will enhance the granular temperature differences between vertical measuring positions.

Due to a few bubbles appearing at the centre line positions near the gas distributor and rising quickly in the bed, the experimental data at central positions fluctuated and were not easily acquired. To acquire stable and easily repeatable data another position at which fewer bubbles were observed in the experiment, about 45 mm from the fluidized bed edge, was studied.

6.2.2 Granular temperatures on a vertical line between the centreline and the wall of the fluidized bed

The second positions of interest are a series of vertical points between the central line and the wall, which is about 45 mm from the lateral boundary of the fluidized bed. (Figure 6.7)

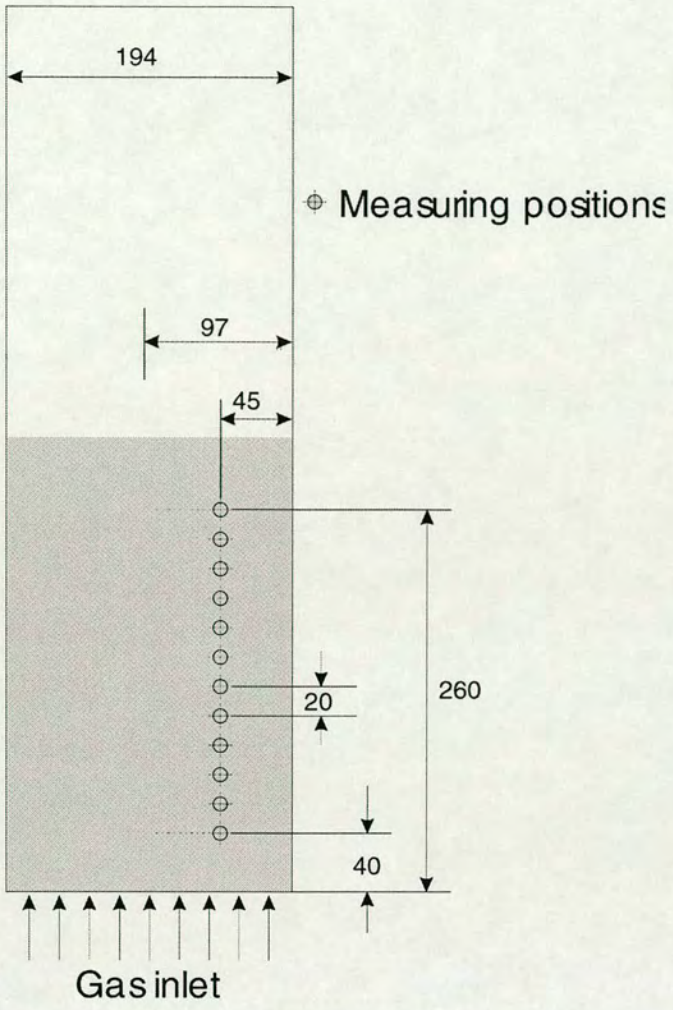

Figure 6.7 Vertical measuring positions 45 mm from the edge of the bed at fixed gas superficial velocity. The distance between each two measuring points is 20 mm approximately, which is near the laser spot diameter (20-30 mm) after multiple scattering in the fluidized bed.

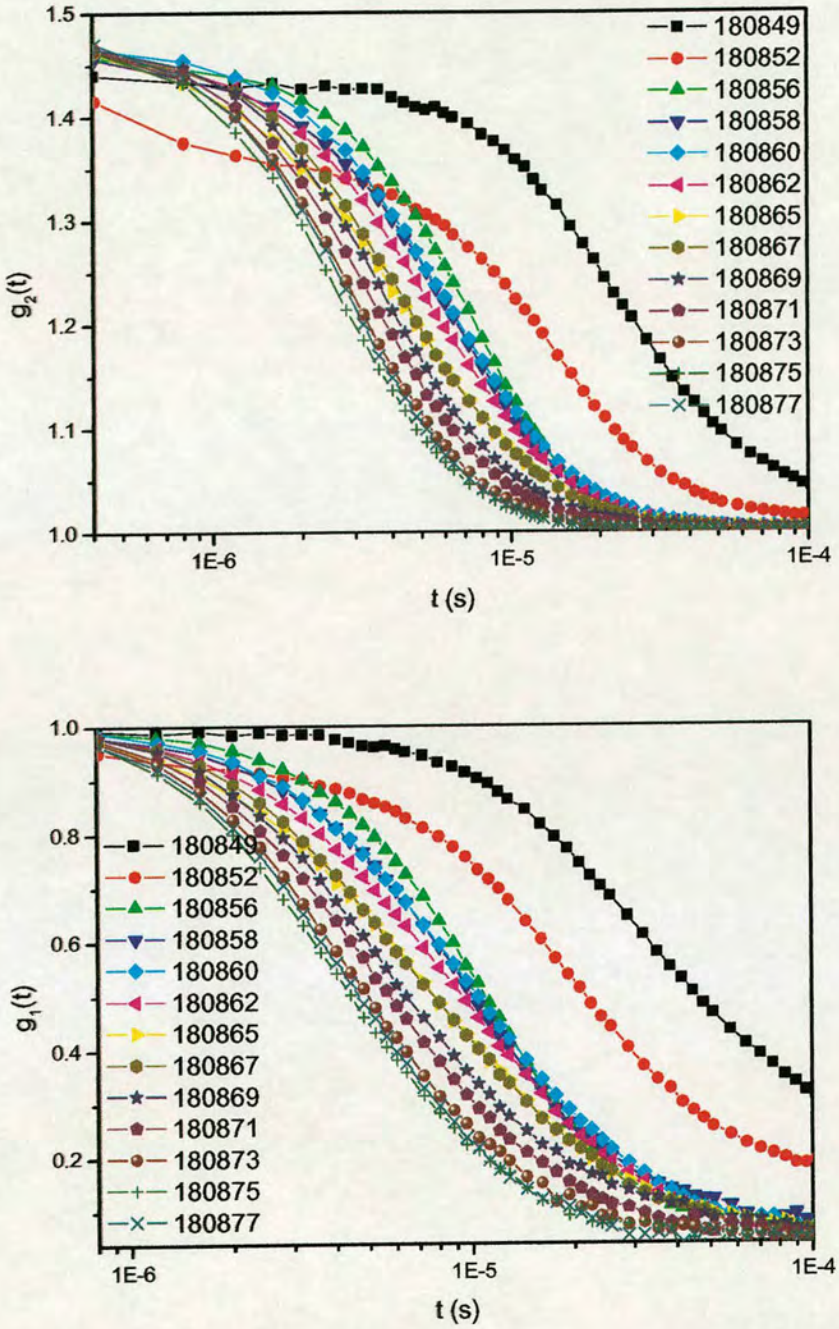

Figure 6.8 Intensity autocorrelation functions measured between the central line and the wall of the fluidized bed at fixed gas superficial velocities. From left to right, h_m=40, 60, 80,100, 120, 140, 160, 180, 200, 220, 240, 260, 270 mm.

Table 6.3 Measuring heights in the DWS experiments (x = 45 mm)

Experiment No.	Measuring height h_m(mm)
180849	40
180852	60
180856	80
180858	100
180860	120
180862	140
180865	160
180867	180
180869	200
180871	220
180873	240
180875	260
180877	270

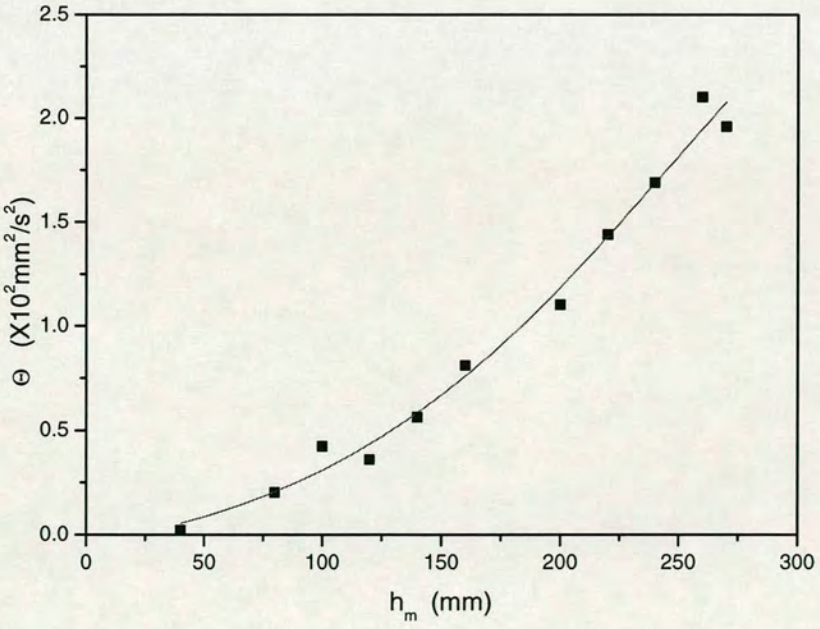

Figure 6.9 Granular temperature at a position 45 mm from the edge of the bed as a function of height above the distributor at U_s = 7.3 mm/s.

Figure 6.8 shows the intensity autocorrelation functions measured at 45 mm from the edge of the bed at fixed gas velocity. Compared with Figure 6.6 in which the intensity autocorrelation function on the centre line is plotted, the curves in Figure 6.8 are more regularly distributed than those in Figure 6.6. In the experiment, fewer bubbles were found at these positions which provided a more stable status for DWS to take better measurements.

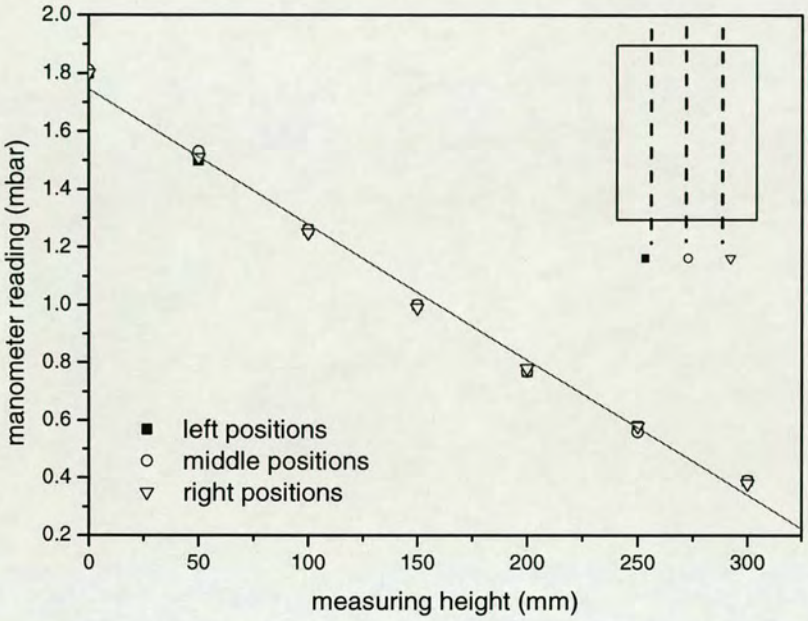

Figure 6.10 Pressure profile in the fluidized bed by direct measurement at U_s=7.3 mm/s. Three series of vertical positions were measured.

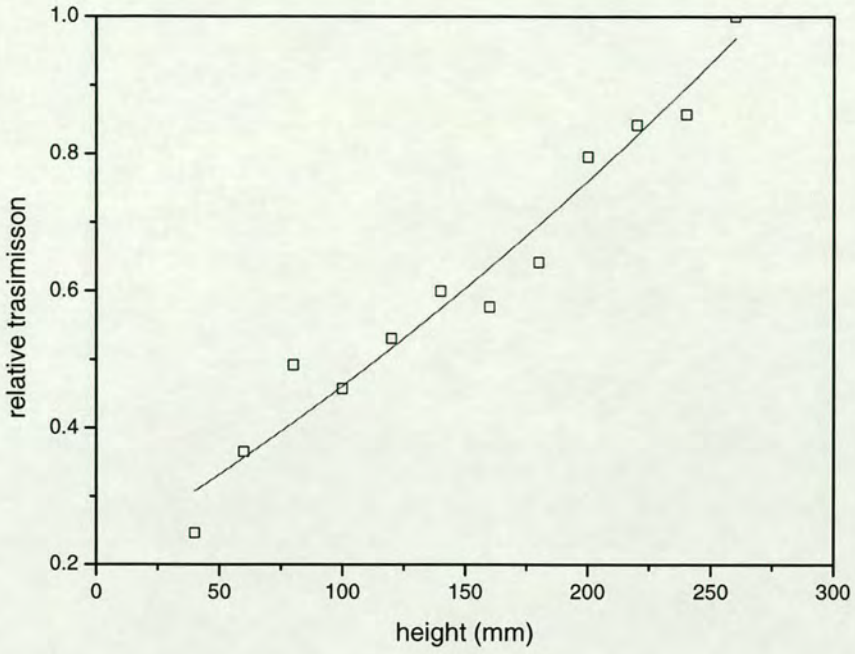

Figure 6.11 Relative transmission vs. bed height

A small diameter tubular glass probe was used to measure pressure distribution with height in the bed directly. One end of the glass duct was connected to a digital manometer, the other end, which was filled with some glass wool to avoid particles blocking the probe, was inserted into the fluidized bed to measure the pressure gradient in the bed.

According to Equation 3.1, the bed bulk voidage can be derived from:

$$\varepsilon_s = \frac{-dP/dh}{(\rho_s - \rho_g)g} \tag{6.2}$$

Figure 6.10 shows the pressure profile measurement results at the centre of the bed and at two positions near its wall. It suggests that the bulk voidage is homogeneous, but light transmission measurement results (Figure 6.11) suggests a denser phase near the bottom of the bed and a more dilute phase near the top. One possible reason that might be related both to the granular temperature increase with height and to the increase in light transmission is particle agglomeration.

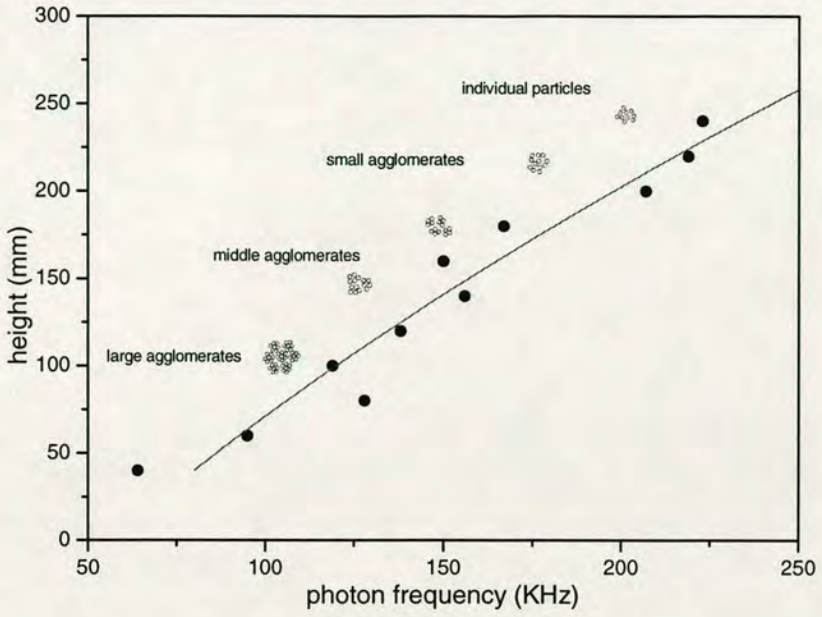

Figure 6.12 Particle agglomeration in the fluidized bed

When small particles agglomerate during fluidization, larger agglomerates are usually present near the bottom of the bed while small agglomerates and individual particles are near the top of the bed (Figure 6.12). The 'free space' for those large agglomerates to move is relatively small when they are near the gas distributor, while in the top part of the bed small agglomerates and individual particles have a relatively large space to move freely, which might result in a higher granular temperature. In the fluidization experiments, channelling flows could be easily observed in the bed at the onset of fluidization (corresponding to low gas velocity) and near the gas distributor at higher gas superficial velocity. These suggest cohesive particle behaviour. However, channels disappear at high gas velocity and the bed expands smoothly, resembling Group A particle behaviour. Particle agglomerates were observed by naked eye at the bottom of a circulating fluidized bed after a period of running (Figure 6.13). Whilst it was not possible to obtain direct evidence for such clustering in the non-circulating fluidized bed, it has been reported by a number of groups for cohesive particles such as those used here [107] and [114]. The presence of larger clusters will move the material's position in the Geldart particle diagram from Group C to Group A. The progression of fluidization behaviour from

channelling flow (Group C) to smooth expanding flow (Group A) was observed in the fluidization experiments when gas velocity increased.

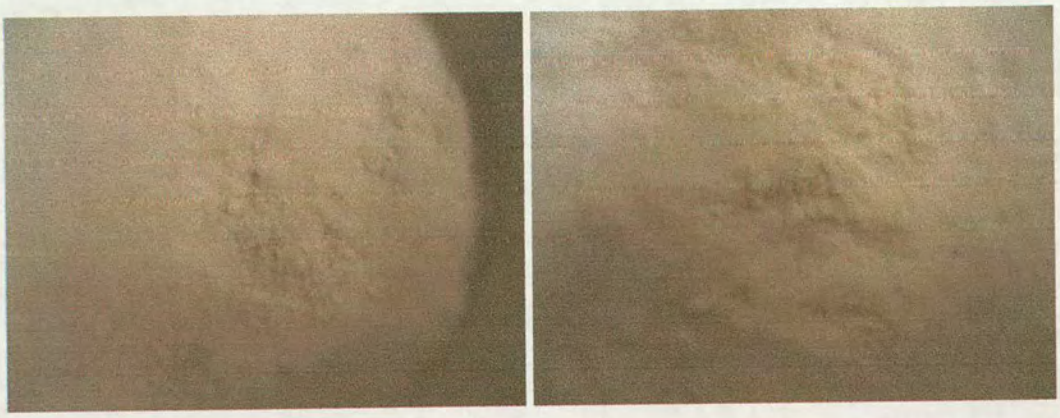

Figure 6.13 Agglomerates can be found at the bottom of the CFB after running.

From Figure 6.9 we found that the granular temperatures in the vertical direction obeyed the same trend as that in Figure 6.6 qualitatively, but their values were quantitatively smaller than those in the central positions. This arouses our interest in studying the granular temperature profiles in the horizontal direction.

6.2.3 Granular temperature profiles at different vertical positions

Granular temperatures at three vertical positions were studied at three different gas velocities from low to high. DWS experiments were performed at five measuring positions at each horizontal level as shown in Figure 6.14.

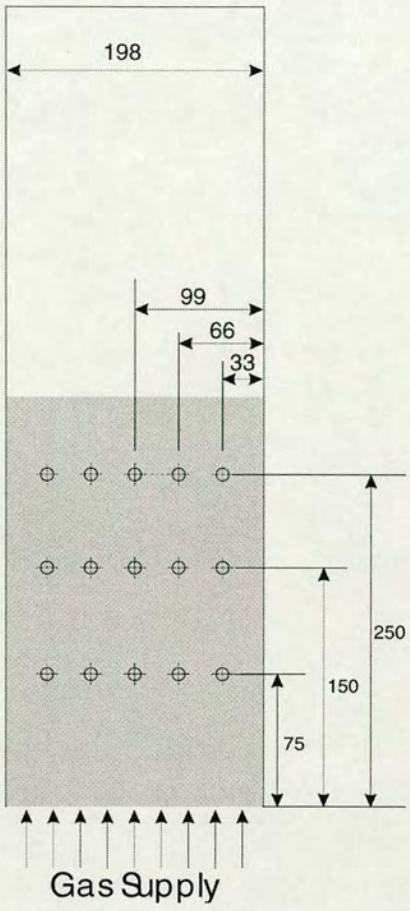

Figure 6.14 Measuring positions at different horizontal positions

Figure 6.15- Figure 6.17 show profiles of granular temperature with horizontal position at three heights above the distributor plate. At each gas velocity and horizontal position the maximum in granular temperature corresponding to the centreline of the bed agrees with intuitive ideas of maximal bed activity at the centreline, possibly agreeing with the "upwards at the centre, downwards at the walls" (UCDW) pattern of bulk particle motion often observed in 2-dimensional fluidized beds and suggesting that there is an empirical relationship between granular temperature and bulk particle velocity.

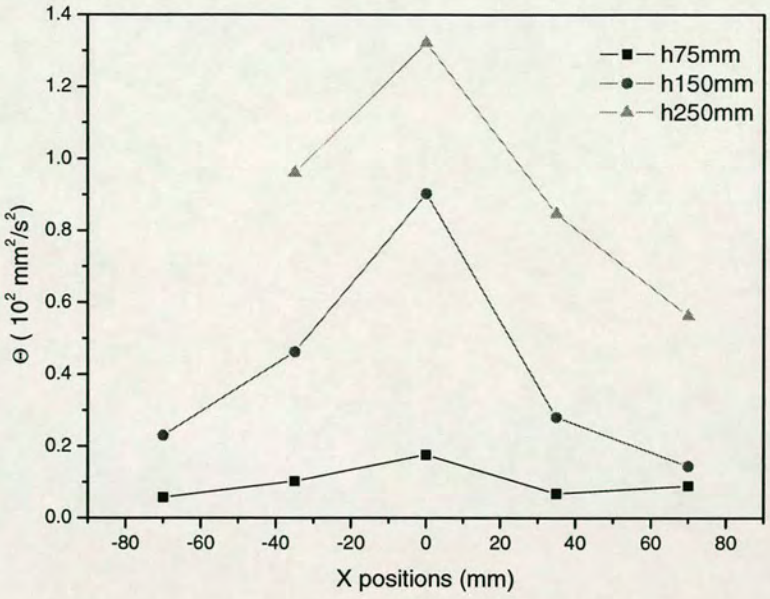

Figure 6.15 Granular temperature profiles in the fluidized bed at low gas velocity, U_s= 4.6 mm/s

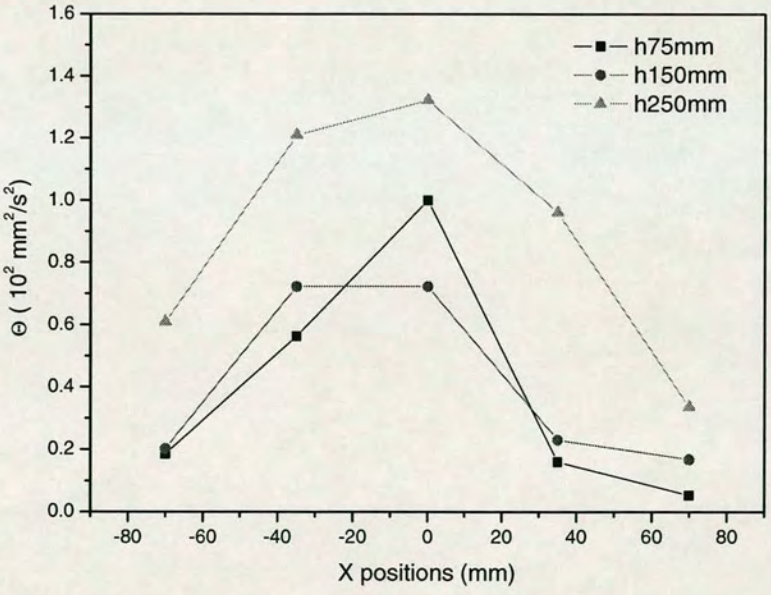

Figure 6.16 Granular temperature profiles in the fluidized bed at medium gas velocity, U_s= 5.3 mm/s

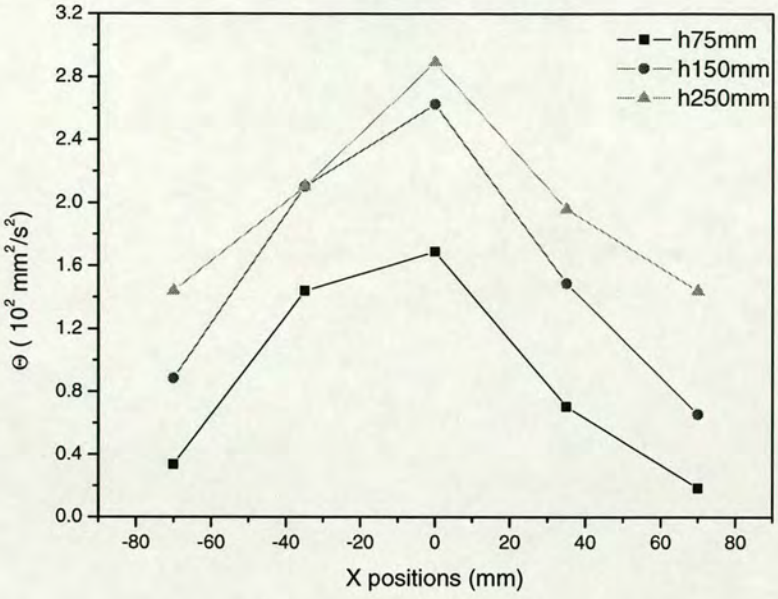

Figure 6.17 Granular temperature profiles in the fluidized bed at high gas velocity, U_s= 7.3 mm/s

6.3 Comparison of granular temperature results from transmission and backscattering geometry

Figure 6.18 is comparison of mean square displacements calculated from transmission and backscattering geometry. The straight line fits the curves very well at short time.

As discussed in Chapter 5, several parameters and factors will affect the DWS measurement results. Their variation could violate some fundamental assumptions of DWS theory under transmission and backscattering geometry. Since measurements from both transmission and backscattering DWS are studying the same area of interest, for ideal conditions the granular temperature results calculated from both geometries should have the same results. But after data analysis from the two geometries there sometimes exists a discrepancy between the two mean square displacement curves, especially at long time delays. In Figure 6.18 the MSD curves

coincide at short time and fit very well a straight line (ballistic motion assumption at short time), but there are large differences at longer time delays.

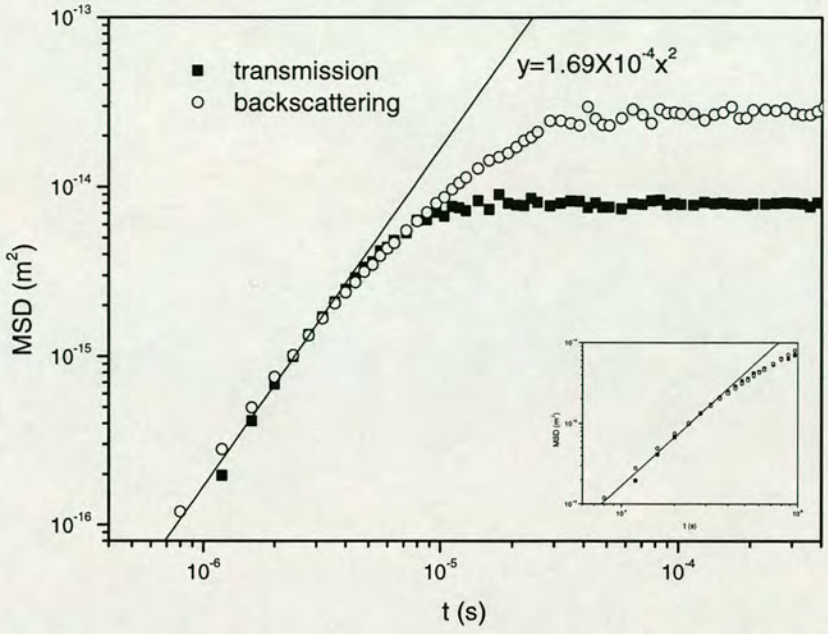

Figure 6.18 MSD differences at long autocorrelation time between transmission and backscattering geometries. At short time MSD curves for both transmission and backscattering measurements fit well the equation $MSD = (\delta V)^2 \cdot t^2$

In the data analysis process it is tempting to replace $6t/\tau$ in Equation (4.27) with $k_0^2 \langle \Delta r^2(t) \rangle$ and use backscattering measurements to probe $\Delta r^2(t)$ over the full range of decay times. Such an analysis of the data cannot be correct, except for the initial decay period. This is because the diffusion approximation and central limit theorem used in arriving at this result are valid only for long paths, and break down for short paths which correspond to long time decay. [95]

6.4 Granular temperature in a circulating fluidized bed

As mentioned in Chapter 3, when the gas velocity increases in a bed containing particles, the bed might successively undergo fixed bed, minimum fluidization,

smooth fluidization, bubbling fluidization, slugging and turbulent fluidization. When the gas velocity is higher than the particle terminal velocity, solid particles will be carried out from the fluidized bed with the fluidizing gas. With a cyclone, return leg and control valve added to the fluidization system, a circulating fluidized bed (CFB) results.

Gidaspow et al. used a CCD camera and image analysis to method measure granular temperature in a circulating fluidized bed of FCC catalyst [69]. For a dense gas-solid system, van Wachem et al compared different CFD simulation models [43]

Following are some preliminary experimental studies of CFB by diffusing-wave spectroscopy.

6.4.1 Circulating fluidized bed

A laboratory scale circulating fluidized bed was built. Several fluidization operating conditions were studied. The total height of the riser was 1.1 m with an inside diameter of 19 mm, the same inside diameter as the downcomer. The angle between the riser and the downcomer was 45° and the gas used in the experiment was compressed air.

The downcomer valve used was a simplification of the V-valve, as there was no aeration of the downcomer stream. In order to compensate for this, and to ensure good levels of particle recirculation were achieved, an inner pipe was added to the gas distribution section. This can be seen more clearly in Figure 6.19.

This inner pipe, with an outer diameter of 15 mm, allowed the primary gas flow to enter above the junction between the riser and downcomer, thus ensuring that only a very small proportion, if any, of the gas from this stream would flow straight into the downcomer. Were this to occur, then the flow rising through the downcomer would resist the flow of particles being recycled from the cyclone, which in turn would significantly decrease the solid recirculation rate.

A second, smaller gas stream entered at the base of the riser and flowed through the gap between the central pipe and the inner surface of the riser. The purpose of this stream was to fluidize the particles below the level of the primary air inlet, thus allowing the particles to be entrained into the higher velocity primary air stream and subsequently carried up the riser.

To simplify, the flow through the central pipe will be referred to as the centre gas flowrate and the flow through the gap between the pipe and the wall as the side gas flowrate.

Filter paper was used as gas distributor in the ring area between the central inner pipe and riser to give an adequately low pressure drop.

A metal mesh was used as the gas distributor in the central pipe. The size of mesh used for this was 48 μm. This mesh was included to ensure that no backflow of particles occurred through the inner pipe.

6.4.2 Fluidization conditions

In order to take measurements, the bed was manoeuvred so that the part of the bed to be investigated, either the riser or the downcomer, was directly in line with the laser beam between the last mirror and the detector. The bed was then raised or lowered so that the laser passed through the CFB at the height of interest.

Two positions, one in the riser and one in the downcomer, were studied. The position in the riser was located 515 mm above the central gas distributor. The position of interest in the downcomer was located at 250 mm above the point where the vertical downcomer joined the riser by a 45° connector.

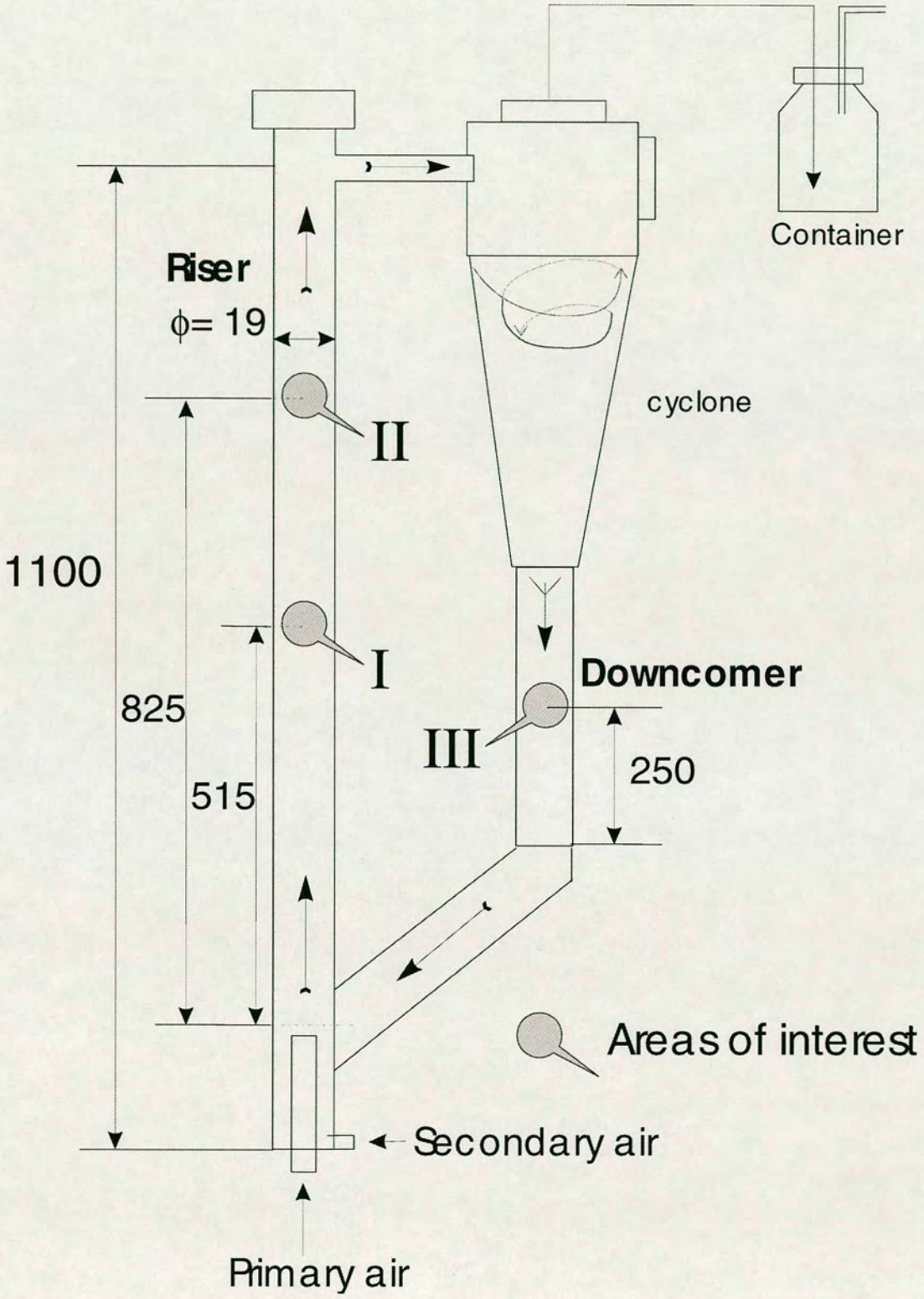

Figure 6.19 Studying areas of a laboratory scale circulating fluidized bed

6.4.3 CFB granular temperature results

Compared with a fluidized bed, gas-flow in a CFB is more dilute and faster. It is difficult to control the fluidization system in a stable state. In the fluidized bed, the transport mean free path could be determined by measuring total light transmission in different thickness of fluidized bed under the same conditions of bed expansion, but, for a CFB, it is very difficult to achieve the same flow conditions in different units.

However, in our CFB apparatus we found that the transmitted light intensity did not change much with gas velocity in most experiments. Thus, we assumed a constant transport mean free path in the data analysis. Because l^* was a constant in the analysis of granular temperature, the value of l^* will not change the trend of granular temperature. We can acquire quantitive granular temperature results by assuming constant transport mean free path.

An estimated value of transport mean free path $l^* \approx 2mm$ was used to calculate granular temperatures in the CFB. The diameter of the tube is 19 mm.

Under this condition $\frac{D}{l^*} \approx 10$, the DWS multiple scattering assumption is still valid.

Figure 6.20 and Figure 6.21 show granular temperature at the riser and downcomer. Since the CFB was running under much higher gas superficial velocity, the particle in the CFB had much higher kinetic energy, so its granular temperature would be expected to be correspondingly higher. However, from these two figures we found the granular temperatures in the CFB were relatively smaller than those in the non-circulating fluidized beds. Because the solid flow in the CFB was much more dilute than that of a non-circulating fluidized bed, the number of collisions between particles which will generate velocity fluctuation was much smaller in the CFB. As granular temperature is defined as the mean of velocity fluctuation, although a particle's velocity was high in the CFB, its fluctuation might be relatively small, which means a low granular temperature.

The granular temperatures are smaller in the downcomer position than in the riser. After the particle enters the cyclone, its movement is driven by gravity. Since there is no more energy input to the particle except from gravity, its energy dissipates by collision with other particles and the wall as the particle travels in the cyclone and down to the downcomer.

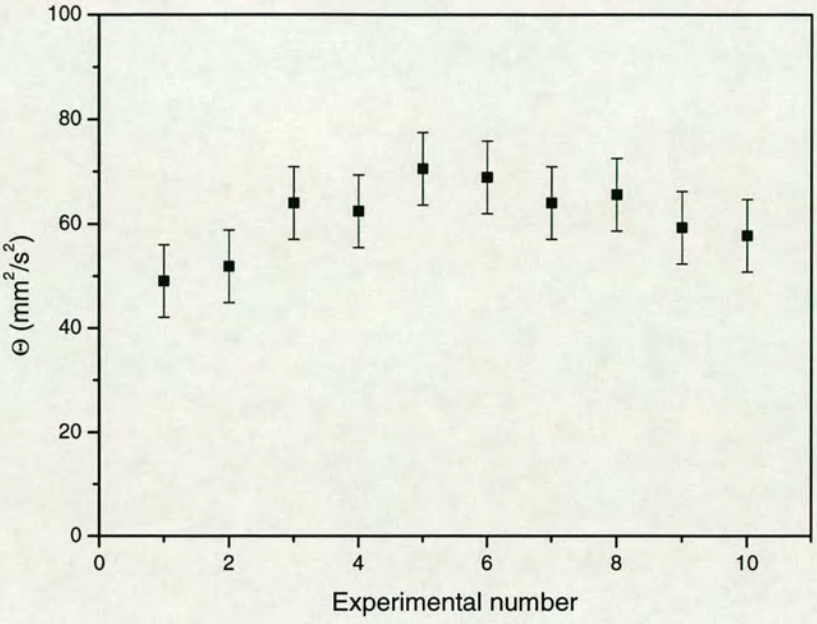

Figure 6.20 Granular temperatures in the CFB riser (area I in Figure 6.19)

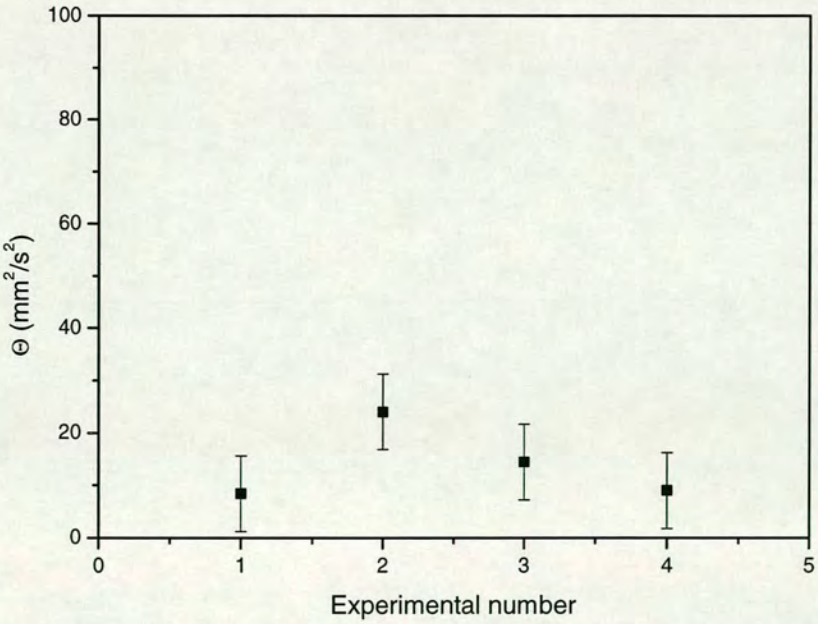

Figure 6.21 Granular temperatures in the CFB downcomer (area III in Figure 6.19)

6.5 Comparison of different granular temperature measurement results

Several techniques used in the study of granular temperature have been discussed in Chapter 2. Table 6.4 compares granular temperature measurement results from these techniques.

Table 6.4 Comparison of different granular temperature measurement results

Work done by	Method	Particle	Geometry	Group	Θ (m^2/s^2)
Menon & Durian [44]	DWS	Solid glass beads dp=49 – 194 μm	Fluidized bed	B	$10^{-9} - 10^{-4}$
Cody etc. [58]	ASNP	Glass beads dp=63 – 595μm	Fluidized bed	A	$1\times10^{-4} - 2.1\times10^{-3}$
				B	$2.29\times10^{-3} - 0.062$
Valverde etc. [79]	Colour analysis	Xerographic toner dp=8.53μm	Fluidized bed	C	$2\times10^{-8} - 3.76\times10^{-5}$
Gidaspow etc. [69]	Image analysis	FCC catalyst dp=75 μm	CFB	A	0.21 – 2.74
This work	DWS	Hollow glass beads, dp=60 μm	Fluidized bed	C	$4.41\times10^{-6} - 3.0\times10^{-4}$
This work	DWS	Hollow glass beads, dp=60 μm	CFB	C	$8.41\times10^{-6} - 7.06\times10^{-5}$

6.6 Conclusions

1) Granular temperature increases with increasing gas velocity at a fixed position.
2) At fixed gas velocity, the higher the measuring position, the larger the granular temperature. This might be due to different transport mean free paths and particle agglomeration at different parts of the bed.
3) Granular temperature profiles seem to correspond to UCDW patterns of particle circulation (Upwards at the Centre, Downwards at the Wall) for the horizontal direction.

4) At long time delays the backscattering geometry breaks down. As a result MSD curves are different from transmission and backscattering geometries.

5) In CFB, granular temperatures in the riser are much higher than that in the downcomer.

Chapter 7 Conclusions and future work

7.1 Conclusions

This thesis concerns the granular temperatures in the fluidized bed by the non-intrusive diffusing-wave spectroscopy technique.

Chapter 3 concerns the diffusing-wave spectroscopy technique. Based on the light diffusion approximation and an averaged movement path of photons, multiple dynamic light scattering was successfully developed to study opaque samples such as fluidized beds. By using Q-Cel 5020 hollow glass particles with a specifically designed fluidized bed apparatus, we applied both transmission and backscattering DWS geometries to study particle micro-dynamics under different fluidization states. Particle mean square displacement at short time delay was determined by measuring the intensity autocorrelation functions of transmitted and backscattered light. Then particle granular temperature was calculated from the curve of mean square displacement versus autocorrelation time at short delays.

Chapter 4 reports experimental characterization of Q-Cel 5020 hollow glass particles. In this chapter the Geldart particle classification was first introduced. According to their density and size distribution, Q-Cel 5020 particles belong to Group C which is very difficult to fluidize. In the fluidization experiments with these particles we found that channelling flows appeared in the bed at the onset of fluidization. However, with increasing gas superficial velocity these channels were observed only near the gas distributor and then they disappeared at high gas velocity. The bed expanded smoothly and remained homogeneous over a wide range of gas velocity

until bubbles could be observed at high gas velocity. Minimum fluidization velocity and minimum bubbling velocity were determined from the curves of bed expansion vs. gas superficial velocity and pressure drop across bed vs. gas superficial velocity respectively. Both velocities were in good agreement with theoretically predicted results. The characterization experiments showed that the Q-Cel 5020 particles had distinctive fluidization properties which could not be easily assigned to any single group on the Geldart particle diagram.

Chapter 5 reports a parametric study of the DWS results. Firstly, total light transmission was studied. The transmitted light displayed a Gaussian profile. With total transmission data measured from five fluidized beds under three bed expansions, a full equation was used to analyse transport mean free path l^* and absorption length l_a. l^* ranged from 0.12 mm to 0.70 mm. In our experiment it increased with bed expansion. At the same bed expansion, the higher measuring position, the larger l^*. l_a did not change much under all measurement conditions and was treated as a constant. To acquire best measurement in the DWS experiments, measuring geometry, measuring positions, detector positions, laser power and polarization angle effects were studied. For the backscattering geometry, the detector position was crucial to the measurement of the autocorrelation function. Laser power did not affect autocorrelation function much, but a higher laser power is suggested to get good signal-noise ratio. For transmission geometry, fluctuations could be found when a polarizer was added. For backscattering geometry, there is no difference when a polarizer was added -- on the other hand, this also proved that the multiple scattering assumption is valid when DWS is applied to the fluidized beds.

Chapter 6 presents systematic measurement results of granular temperature in the fluidized bed. Granular temperatures at a fixed position were found to increase with gas superficial velocity. Measurements from two series of positions have been taken to study variations of granular temperature with height at a fixed gas velocity. At both positions the granular temperatures increased montonically with measuring height. Use of a probe to measure the pressure profile with height in the bed suggested, because the pressure gradient was constant, that voidage does not vary

significantly with height. The light transmission results suggest the presence of agglomerates in the bed, which might change the size of the particle clusters and result in different fluidization behaviour under different gas superficial velocity conditions. The granular temperature profiles at three horizontal positions were studied. The horizontal profile seems to reflect UCDW patterns of particle circulation. Granular temperatures in a laboratory scale CFB were also studied. The granular temperatures in the riser are higher than those in the downcomer. Compared with a stationary fluidized bed, granular temperatures in the CFB were smaller.

7.2 Future work

7.2.1 Improvement of current work

When the laser light penetrates into the fluidized bed and is scattered by the particles, a bright scattering region can be found. Its size depends on the bed expansion (local voidage) and thickness of the bed. In most DWS experiments the diameter of the bright spot is between 1 cm and 2.5 cm. In the DWS experiment what we measured was averaged granular temperature of this scattering volume. To get precise granular temperature data at exact points rather than over a region, pinholes could be added to the DWS configuration (Figure 7.1).

By adding two pinholes in either geometry of the DWS set-up, granular temperature might be measured exactly at a point position. This improvement of current DWS could extend its application to more common conditions and explore more details of the objects studied. The disadvantage of this set-up is that a very low proportion of the light would be able to pass through the two pinholes, which would result in a low photon density and possibly a relatively low signal-noise ratio at the detector.

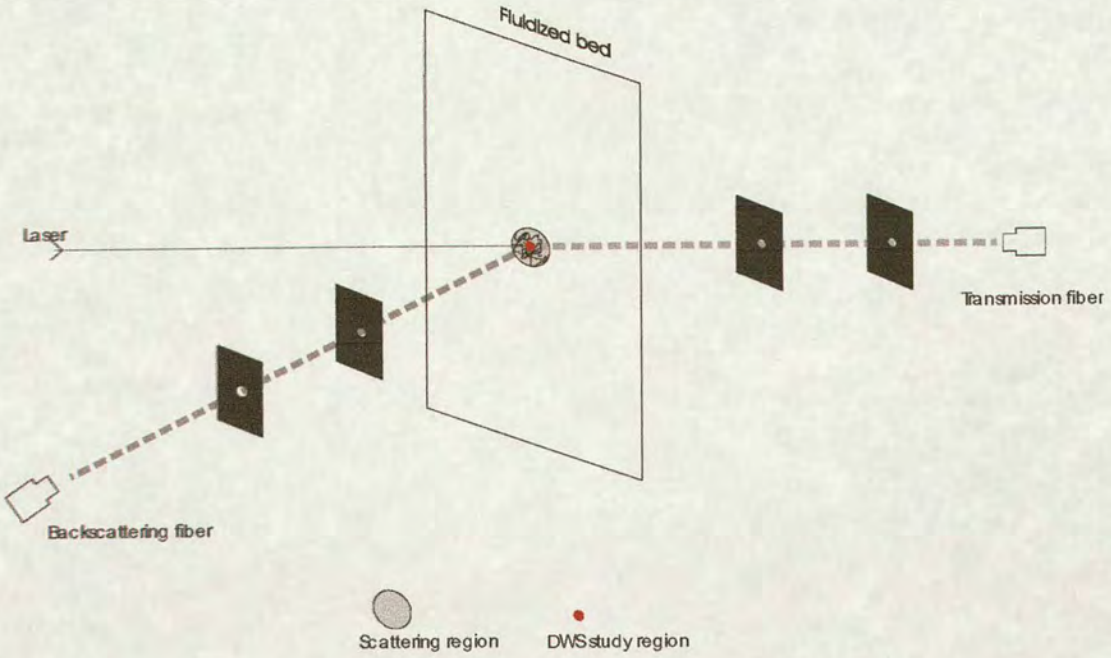

Figure 7.1 Measuring granular temperature precisely at a point position

In Chapter 6, granular temperature profiles, possibly related to UCDW patterns were found. It would be interesting to combine DWS with other particle circulation measurements and local voidage measurement techniques, such as PEPT, PIV and tomographic methods, to study the behaviour of particle agglomerates during fluidization.

7.2.2 Towards the study of more representative systems

In this project, granular temperatures in a rectangular fluidized bed and a laboratory scale circulating fluidized bed were studied. In industry, both the dimensions and geometry of a fluidized bed system might be quite different from our laboratory models. For transmission geometry it is very difficult to collect a sufficient laser intensity after numerous multiple scattering events when they occur in a large dimensioned object. Also it is almost impossible to determine transport mean free path by measuring transmitted light from objects of various thicknesses. Yet DWS in backscattering geometry is a promising technique because for this system it is not necessary to know the transport mean free path in order to analyse data when the boundary is semi-infinite. In fact large scale industrial units would always provide a

good approximation to a semi-infinite boundary for DWS backscattering measurements. The difficulty would be in identifying the volume of the unit interior actually sampled by the backscattered light. Some further theoretical or experimental study of the path length distribution in the backscattering mode would be necessary.

Studying heat transfer in complex geometries such the region near fluidized bed tube bundles would be of particular interest [115-119]. By DWS, particle micro-dynamics near cylinders inserted into the fluidized bed can be measured in geometries similar to those illustrated in Figure 7.2. These results would also be interesting to compare with granular temperatures in the unimpeded bed.

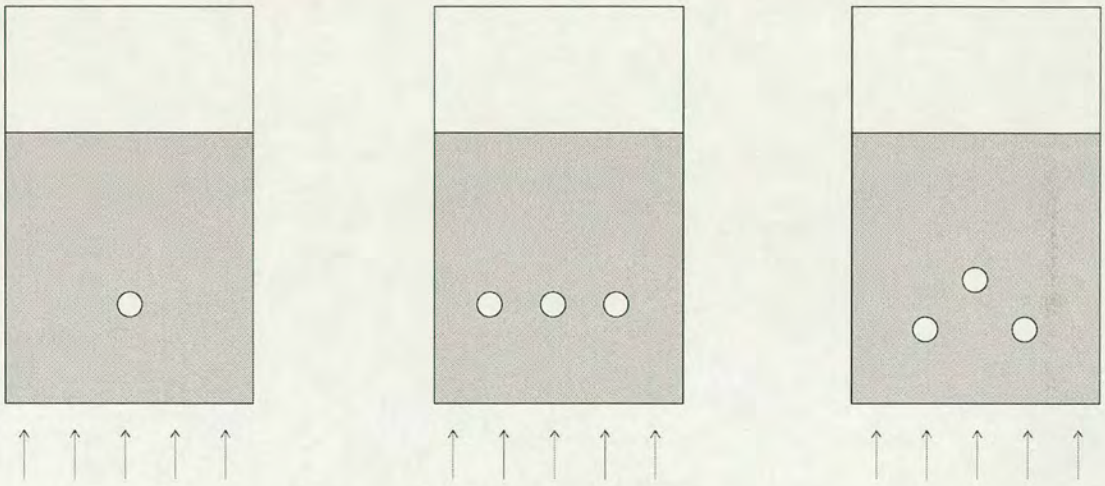

Figure 7.2 Using DWS to study geometrically complex systems

DWS has been used in the study of many liquid samples such as colloidal systems and bubbling flows. When the fluidizing fluid is a liquid, the bed will expand more smoothly and stably. As liquid-solid granular flows are also widely used in the chemical industry, the DWS technique would be a practical approach to study particle/droplet behaviour in complex gas-liquid-solid multiphase systems.

References

[1] Jacques D., *Sands, Powders, and Grains. An Introduction to the Physics of Granular Materials*. Springer-Verlag, (2000).

[2] Squires A. M., Kwauk M. and Avidan A. A., "Fluid Beds - at Last, Challenging 2 Entrenched Practices," *Science*, **230**, 1329-1337 (1985).

[3] Seville J. P. K., Tuzun U. and Clift R., *Processing of particulate solids*. Blackie academic and profesional, London (1997).

[4] Ristow G. H., Strassburger G. and Rehberg I., "Phase diagram and scaling of granular materials under horizontal vibrations," *Physical Review Letters*, **79**, 833-836 (1997).

[5] Shinbrot T., "Competition between randomizing impacts and inelastic collisions in granular pattern formation," *Nature*, **389**, 574-576 (1997).

[6] Savage S. B., "Analyses of slow high-concentration flows of granular materials," *Journal of Fluid Mechanics*, **377**, 1-26 (1998).

[7] Lemaitre A., "Origin of a repose angle: Kinetics of rearrangement for granular materials," *Physical Review Letters*, **89**, art. no.-064303 (2002).

[8] Trujillo L. and Herrmann H. J., "Hydrodynamic model for particle size segregation in granular media," *Physica A: Statistical Mechanics and its Applications*, **330**, 519-542 (2003).

[9] Campbell C. S., "Rapid Granular Flows," *Annual Review of Fluid Mechanics*, **22**, 57-92 (1990).

[10] Campbell C. S., "The Stress Tensor for Simple Shear Flows of a Granular Material," *Journal of Fluid Mechanics*, **203**, 449-473 (1989).

[11] Savage S. B. and Sayed M., "Gravity Flow of Coarse Cohesionless Granular-Materials in Conical Hoppers," *Zeitschrift Fur Angewandte Mathematik Und Physik*, **32**, 125-143 (1981).

[12] Nedderman R. M., Tuzun U., Savage S. B. and Houlsby G. T., "The Flow of Granular-Materials .1. Discharge Rates from Hoppers," *Chemical Engineering Science*, **37**, 1597-1609 (1982).

[13] Aranson I. S. and Tsimring L. S., "Dynamics of axial separation in long rotating drums," *Physical Review Letters*, **82**, 4643-4646 (1999).

[14] Felix G., Falk V. and D'Ortona U., "Segregation of dry granular material in rotating drum: experimental study of the flowing zone thickness," *Powder Technology*, **128**, 314-319 (2002).

[15] Sherritt R. G., Chaouki J., Mehrotra A. K. and Behie L. A., "Axial dispersion in the three-dimensional mixing of particles in a rotating drum reactor," *Chemical Engineering Science*, **58**, 401-415 (2003).

[16] Nag P. K. and Moral M. N. A., "Effect of Probe Size on Heat-Transfer at the Wall in Circulating Fluidized-Beds," *International Journal of Energy Research*, **14**, 965-974 (1990).

[17] Wu R. L., Lim C. J., Grace J. R. and Brereton C. M. H., "Instantaneous Local Heat-Transfer and Hydrodynamics in a Circulating Fluidized-Bed," *International Journal of Heat and Mass Transfer*, **34**, 2019-2027 (1991).

[18] Qian R. Z. and Saxena S. C., "Heat-Transfer from an Immersed Surface in a Magnetofluidized Bed," *International Communications in Heat and Mass Transfer*, **20**, 859-869 (1993).

[19] Barigou M. and Greaves M., "A Capillary Suction Probe for Bubble-Size Measurement," *Measurement Science & Technology*, **2**, 318-326 (1991).

[20] Coronella C. J. and Deng J. X., "A novel method for isokinetic measurement of particle flux within the riser of a circulating fluidized bed," *Powder Technology*, **99**, 211-219 (1998).

[21] Malcus S., Cruz E., Rowe C. and Pugsley T. S., "Radial solid mass flux profiles in a high-suspension density circulating fluidized bed," *Powder Technology*, **125**, 5-9 (2002).

[22] Lesinski J., Mizeralesinska B., Fanton J. C. and Boulos M. I., "Laser Doppler Anemometry Measurements in Gas-Solid Flows," *AIChE Journal*, **27**, 358-364 (1981).

[23] Ainsworth R. W., Thorpe S. J. and Manners R. J., "A new approach to flow-field measurement - A view of Doppler global velocimetry techniques," *International Journal of Heat and Fluid Flow*, **18**, 116-130 (1997).

[24] Rheims J., Wriedt T. and Bauckhage K., "Sizing of inhomogeneous particles by a differential laser Doppler anemometer," *Measurement Science & Technology*, **10**, 68-75 (1999).

[25] Ibsen C. H., Solberg T., Hjertager B. H. and Johnsson F., "Laser Doppler anemometry measurements in a circulating fluidized bed of metal particles," *Experimental Thermal and Fluid Science*, **26**, 851-859 (2002).

[26] Lueptow R. M., Akonur A. and Shinbrot T., "PIV for granular flows," *Experiments in Fluids*, **28**, 183-186 (2000).

[27] Chehata D., Zenit R. and Wassgren C. R., "Dense granular flow around an immersed cylinder," *Physics of Fluids*, **15**, 1622-1631 (2003).

[28] Grant I. and Smith G. H., "Modern Developments in Particle Image Velocimetry," *Optics and Lasers in Engineering*, **9**, 245-264 (1988).

[29] Grant I., "Particle image velocimetry: A review," *Proceedings of the Institution of Mechanical Engineers Part C- Journal of Mechanical Engineering Science*, **211**, 55-76 (1997).

[30] Mueth D. M., Debregeas G. F., Karczmar G. S., Eng P. J., Nagel S. R. and Jaeger H. M., "Signatures of granular microstructure in dense shear flows," *Nature*, **406**, 385-389 (2000).

[31] Nikitidis M. S., Tuzun U. and Spyrou N. M., "Measurement of size segregation by self-diffusion in slow- shearing binary mixture flows using dual photon gamma-ray tomography," *Chemical Engineering Science*, **53**, 2335-2351 (1998).

[32] Zhu K. W., Rao S. M., Huang Q. H., Wang C. H., Matsusaka S. and Masuda H., "On the electrostatics of pneumatic conveying of granular materials using electrical capacitance tomography," *Chemical Engineering Science*, **59**, 3201-3213 (2004).

[33] vanWachem B. G. M., Bakker A. F., Schouten J. C., Heemels M. W. and deLeeuw S. W., "Simulation of fluidized beds with lattice gas cellular automata," *Journal of Computational Physics*, **135**, 1-7 (1997).

[34] Seibert K. D. and Burns M. A., "Simulation of fluidized beds and other fluid-particle systems using statistical mechanics," *AIChE Journal*, **42**, 660-670 (1996).

[35] Kawaguchi T., Tanaka T. and Tsuji Y., "Numerical simulation of two-dimensional fluidized beds using the discrete element method (comparison between the two- and three-dimensional models)," *Powder Technology*, **96**, 129-138 (1998).

[36] Yuu S., Umekage T. and Johno Y., "Numerical simulation of air and particle motions in bubbling fluidized bed of small particles," *Powder Technology*, **110**, 158-168 (2000).

[37] Boemer A., Qi H. and Renz U., "Eulerian simulation of bubble formation at a jet in a two- dimensional fluidized bed," *International Journal of Multiphase Flow*, **23**, 927-944 (1997).

[38] Boemer A., Qi H. and Renz U., "Verification of Eulerian simulation of spontaneous bubble formation in a fluidized bed," *Chemical Engineering Science*, **53**, 1835-1846 (1998).

[39] Mathiesen V., Solberg T. and Hjertager B. H., "Predictions of gas/particle flow with an Eulerian model including a realistic particle size distribution," *Powder Technology*, **112**, 34-45 (2000).

[40] Schmidt A. and Renz U., "Numerical prediction of heat transfer in fluidized beds by a kinetic theory of granular flows," *International Journal of Thermal Sciences*, **39**, 871-885 (2000).

[41] Schmidt A. and Renz U., "Eulerian computation of heat transfer in fluidized beds," *Chemical Engineering Science*, **54**, 5515-5522 (1999).

[42] Ogawa S., Multitemperature theory of granular meterials. *Proc. US-Japan Seminar on Continuum-Mechanical and Statistical Approaches in the Mechanics of Granular Materials*, Tokyo, 208 (1978).

[43] van Wachem B. G. M., Schouten J. C., van den Bleek C. M., Krishna R. and Sinclair J. L., "Comparative Analysis of CFD Models of Dense Gas-Solid Systems," *AIChE Journal*, **47**, 1035-1051 (2001).

[44] Menon N. and Durian D. J., "Particle motions in a gas-fluidized bed of sand," *Physical Review Letters*, **79**, 3407-3410 (1997).

[45] Ahn H., Brennen C. E. and Sabersky R. H., "Measurements of Velocity, Velocity Fluctuation, Density, and Stresses in Chute Flows of Granular-Materials," *Journal of Applied Mechanics-Transactions of the Asme*, **58**, 792-803 (1991).

[46] Hsiau S. S. and Hunt M. L., "Shear-Induced Particle Diffusion and Longitudinal Velocity Fluctuations in a Granular-Flow Mixing Layer," *Journal of Fluid Mechanics*, **251**, 299-313 (1993).

[47] Roberson J. A. and Clayton T. C., *Engineering fluid mechanics*. John Wiley & Sons, New York (1997).

[48] Kim Y. J. and Kim S. S., "Experimental-Study of Particle Deposition onto a Circular- Cylinder in High-Temperature Particle-Laden Flows," *Experimental Thermal and Fluid Science*, **5**, 116-123 (1992).

[49] Zhang Y. F. and Arastoopour H., "Dilute Fluidized Cracking Catalyst Particles - Gas-Flow Behavior in the Riser of a Circulating Fluidized-Bed," *Powder Technology*, **84**, 221-229 (1995).

[50] Samuelsberg A. and Hjertager B. H., "An experimental and numerical study of flow patterns in a circulating fluidized bed reactor," *International Journal of Multiphase Flow*, **22**, 575-591 (1996).

[51] Ibsen C. H., Solberg T. and Hjertager B. H., "Evaluation of a three-dimensional numerical model of a scaled circulating fluidized bed," *Industrial & Engineering Chemistry Research*, **40**, 5081-5086 (2001).

[52] Werther J., Hage B. and Rudnick C., "A comparison of laser Doppler and single-fibre reflection probes for the measurement of the velocity of solids in a gas- solid circulating fluidized bed," *Chemical Engineering and Processing*, **35**, 381-391 (1996).

[53] Wildman R. D., Huntley J. M., Hansen J. P., Parker D. J. and Allen D. A., "Single-particle motion in three-dimensional vibrofluidized granular beds," *Physical Review E*, **62**, 3826-3835 (2000).

[54] Wildman R. D., Huntley J. M. and Parker D. J., "Granular temperature profiles in three-dimensional vibrofluidized granular beds," *Physical Review E*, **6306**, art. no.-061311 (2001).

[55] Wildman R. D. and Huntley J. M., "Scaling exponents for energy transport and dissipation in binary vibro-fluidized granular beds," *Physics of Fluids*, **15**, 3090-3098 (2003).

[56] Wildman R. D. and Parker D. J., "Coexistence of two granular temperatures in binary vibrofluidized beds," *Physical Review Letters*, **88**, art. no.-064301 (2002).

[57] Stewart R. L., Bridgwater J., Zhou Y. C. and Yu A. B., "Simulated and measured flow of granules in a bladed mixer - a detailed comparison," *Chemical Engineering Science*, **56**, 5457-5471 (2001).

[58] Cody G. D., Goldfarb D. J., Storch J., G. V. and Norris A. N., "Particle granular temperature in gas fluidized beds," *Powder Technology*, **87**, 211-232 (1996).

[59] Cody G. D., Goldfarb D. J., Storch G. V. and Norris A. N., "Particle granular temperature in gas fluidized beds," *Powder Technology*, **87**, 211-232 (1996).

[60] Cody G. D., Bellows R. J., Goldfarb D. J., Wolf H. A. and Storch G. V., "A novel non-intrusive probe of particle motion and gas generation in the feed injection zone of the feed riser of a fluidized bed catalytic cracking unit," *Powder Technology*, **110**, 128-142 (2000).

[61] Warr S., Huntley J. M. and Jacques G. T. H., "Fluidization of a 2-Dimensional Granular System - Experimental- Study and Scaling Behavior," *Physical Review E*, **52**, 5583-5595 (1995).

[62] Wildman R. D., Huntley J. M. and Hansen J. P., "Self-diffusion of grains in a two-dimensional vibrofluidized bed," *Physical Review E*, **60**, 7066-7075 (1999).

[63] Losert W., Cooper D. G. W., Delour J., Kudrolli A. and Gollub J. P., "Velocity statistics in excited granular media," *Chaos*, **9**, 682-690 (1999).

[64] Blair D. L. and Kudrolli A., "Collision statistics of driven granular materials," *Physical Review E*, **67**, art. no.-041301 (2003).

[65] Hsiau S.-S. and Jang H.-W., "Measurements of velocity fluctuations of granular materials in a shear cell," *Experimental Thermal and Fluid Science*, **17**, 202-209 (1998).

[66] Hsiau S.-S. and Shieh Y.-M., "Effect of solid fraction on fluctuations and self-diffusion of sheared granular flows," *Chemical Engineering Science*, **55**, 1969-1979 (2000).

[67] Drake T. G., "Antigranulocytes Flow - Physical Experiments and Their Implications for Microstructural Theories," *Journal of Fluid Mechanics*, **225**, 121-152 (1991).

[68] Natarajan V. V. R., Hunt M. L. and Taylor E. D., "Local measurements of velocity fluctuations and diffusion coefficients for a granular material flow," *Journal of Fluid Mechanics*, **304**, 1-25 (1995).

[69] Gidaspow D. and Huilin L., "Equation of state and radial distribution functions of FCC particles in a CFB," *AIChE Journal*, **44**, 279-293 (1998).

[70] Kantzas A., "Computation of Holdups in Fluidized and Trickle Beds by Computer-Assisted Tomography," *AIChE Journal*, **40**, 1254-1261 (1994).

[71] Seville J. P. K., Morgan J. E. P. and Clift R., Tomographic determination of the voidage structure of gas fluidized beds in the jet region. *Fluidization V*, New York, 87 (1986).

[72] Chung K. Y., Belfort G., Edelstein W. A. and Li X. M., "Dean Vortices in Curved Tube Flow .5. 3-D Mri and Numerical- Analysis of the Velocity-Field," *AIChE Journal*, **39**, 1592-1602 (1993).

[73] Simons S. J. R. and Williams R. A., "Particle-Size Measurement Using Noninvasive Dielectric Sensors," *Powder Technology*, **73**, 85-90 (1992).

[74] Chaouki J., Larachi F. and Dudukovic M. P., "Noninvasive tomographic and velocimetric monitoring of multiphase flows," *Industrial & Engineering Chemistry Research*, **36**, 4476-4503 (1997).

[75] Grassler T. and Wirth K. E., "X-ray computer tomography - potential and limitation for the measurement of local solids distribution in circulating fluidized beds," *Chemical Engineering Journal*, **77**, 65-72 (2000).

[76] Romer S., Urban C., Bissig H., Stradner A., Scheffold F. and Schurtenberger P., "Dynamics of concentrated colloidal suspensions: diffusion, aggregation and gelation," *Philosophical Transactions of the Royal Society of London Series a-Mathematical Physical and Engineering Sciences*, **359**, 977-984 (2001).

[77] Menon N. and Durian D. J., "Diffusing-wave spectroscopy of dynamics in a three-dimensional granular flow," *Science*, **275**, 1920-1922 (1997).

[78] Gidaspow D. and Lu H. L., "Collisional viscosity of FCC particles in a CFB," *AIChE Journal*, **42**, 2503-2510 (1996).

[79] Valverde J. M., Castellanos A. and Quintanilla M. A. S., "Self-diffusion in a gas-fluidized bed of fine powder," *Physical Review Letters*, **86**, 3020-3023 (2001).

[80] Chu B., *Laser light scattering*. Academic Press, INC., (1974).

[81] Berne B. J., *Dynamic light scattering : with applications to chemistry, biology, and physics*. Wiley, New York (1976).

[82] Ishimaru A., *Wave Propagation and Scattering in Random Media*. Wiley-IEEE Press, (1999).

[83] Bicout D. and Maret G., "Multiple Light-Scattering in Taylor-Couette Flow," *Physica A*, **210**, 87-112 (1994).

[84] Lisy V., Brutovsky B. and Miskovsky P., "On dynamic light scattering from vesicle-like droplets," *Physica B*, **266**, 300-309 (1999).

[85] Mason T. G., Gang H. and Weitz D. A., "Rheology of complex fluids measured by dynamic light scattering," *Journal of Molecular Structure*, **383**, 81-90 (1996).

[86] Dixon P. K. and Durian D. J., "Speckle visibility spectroscopy and variable granular fluidization," *Physical Review Letters*, **90**, art. no.-184302 (2003).

[87] Hallett F. R., "Particle-Size Analysis by Dynamic Light-Scattering," *Food Research International*, **27**, 195-198 (1994).

[88] Pine D. J., Weitz D. A., Chaikin P. M. and Herbolzheimer E., "Diffusing-Wave Spectroscopy," *Physical Review Letters*, **60**, 1134-1137 (1988).

[89] Zhu J. X., Durian D. J., Muller J., Weitz D. A. and Pine D. J., "Scaling of Transient Hydrodynamic Interactions in Concentrated Suspensions," *Physical Review Letters*, **68**, 2559-2562 (1992).

[90] Romer S., Urban C., Lobaskin V., Scheffold F., Stradner A., Kohlbrecher J. and Schurtenberger P., "Simultaneous light and small-angle neutron scattering on aggregating concentrated colloidal suspensions," *Journal of Applied Crystallography*, **36**, 1-6 (2003).

[91] Stark H. and Lubensky T. C., "Multiple light scattering in nematic liquid crystals," *Physical Review Letters*, **77**, 2229-2232 (1996).

[92] Stark H., Kao M. H., Jester K. A., Lubensky T. C., Yodh A. G. and Collings E. J., "Light diffusion and diffusing-wave spectroscopy in nematic liquid crystals," *Journal of the Optical Society of America a-Optics Image Science and Vision*, **14**, 156-178 (1997).

[93] Durian D. J., Weitz D. A. and Pine D. J., "Dynamics and Coarsening in 3-Dimensional Foams," *Journal of Physics-Condensed Matter*, **2**, SA433-SA436 (1990).

[94] Vera M. U., Saint-Jalmes A. and Durian D. J., "Scattering optics of foam," *Applied Optics*, **40**, 4210-4214 (2001).

[95] Weitz D. A. and Pine D. J., *Diffusing Wave Spectroscopy, in Dynamic Light Scattering*. Oxford University Press, (1993).

[96] Wiersma D. S., Bartolini P., Lagendijk A. and Righini R., "Localization of light in a disordered medium," *Nature*, **390**, 671-673 (1997).

[97] Cao H., "Lasing in random media," *Waves in Random Media*, **13**, R1-R39 (2003).

[98] Pine D. J., Weitz D. A., Zhu J. X. and Herbolzheimer E., "Diffusing-Wave Spectroscopy - Dynamic Light-Scattering in the Multiple-Scattering Limit," *Journal De Physique*, **51**, 2101-2127 (1990).

[99] Rega C., Lloyd C. J., Attwood D., Clarke D. and Geraghty P., "Temporal autocorrelation function for a diffusing-wave spectroscopy experiment with a point source and backscattering detection," *Applied Optics*, **40**, 4204-4209 (2001).

[100] Durian D. J., Weitz D. A. and Pine D. J., "Multiple Light-Scattering Probes of Foam Structure and Dynamics," *Science*, **252**, 686-688 (1991).

[101] Kunii D. and Levenspiel O., *Fluidization Engineering 2nd Edition*. Butterworth-Heinemann, Boston (1991).

[102] Ergun S., "Fluid Flow through Packed Columns," *Chemical Engineering Progress*, **48**, 89-94 (1952).

[103] Geldart D., "Types of gas fluidization," *Powder Technology*, **7**, 285-292 (1973).

[104] Geldart D. and Abrahamsen A. R., "Homogeneous fluidization of fine powders using various gases and pressures," *Powder Technology*, **19**, 133-136 (1978).

[105] Geldart D. and Ling S. J., "Dense Phase Conveying of Fine Coal at High Total Pressures," *Powder Technology*, **62**, 243-252 (1990).

[106] Chaouki J., Chavarie C., Klvana D. and Pajonk G., "Effect of interparticle forces on the hydrodynamic behaviour of fluidized aerogels," *Powder Technology*, **43**, 117-125 (1985).

[107] Zhao G. Y., Zhu C. W. and Hlavacek V., "Fluidization of Micron-Size Ceramic Powders in a Small-Diameter Fluidized-Bed," *Powder Technology*, **79**, 227-235 (1994).

[108] Richardson J. F. and Zaki W. N., "The Sedimentation of a Suspension of Uniform Spheres under Conditions of Viscous Flow," *Chemical Engineering Science*, **3**, 65-73 (1954).

[109] Geldart D. and Wong A. C. Y., "Fluidization of powders showing degrees of cohesiveness--I. Bed expansion," *Chemical Engineering Science*, **39**, 1481-1488 (1984).

[110] Davidson J. R. and Harrison D., *Fluidised particles*. Cambridge University Press, Cambridge (1963).

[111] Leutz W. and Ricka J., "On light propagation through glass bead packings," *Optics Communications*, **126**, 260-268 (1996).

[112] Kaplan P. D., Kao M. H., Yodh A. G. and Pine D. J., "Geometric Constraints for the Design of Diffusing-Wave Spectroscopy Experiments," *Applied Optics*, **32**, 3828-3836 (1993).

[113] Gidaspow D. and Mostofi R., "Maximum carrying capacity and granular temperature of A, B and C particles," *AIChE Journal*, **49**, 831-843 (2003).

[114] Wang Z. L., Kwauk M. and Li H. Z., "Fluidization of fine particles," *Chemical Engineering Science*, **53**, 377-395 (1998).

[115] Garim M. M., Freire J. T. and Goldstein R. J., "Local mass transfer coefficients around a cylinder in a fluidized bed," *Powder Technology*, **101**, 134-141 (1999).

[116] Muroyama K., Yoshikawa T., Takakura S. and Yamanaka Y., "Mass transfer from an immersed cylinder in three-phase systems with fine suspended particles," *Chemical Engineering Science*, **52**, 3861-3868 (1997).

[117] Sunderesan S. R. and Clark N. N., "Local Heat-Transfer Coefficients on the Circumference of a Tube in a Gas-Fluidized Bed," *International Journal of Multiphase Flow*, **21**, 1003-1024 (1995).

[118] Nieh S., Lee S. W. and Fu T. T., "Effects of Tube Orientation and Gas Velocity on the Erosion of a Tube Inserted into a Fluidized-Bed," *Powder Technology*, **67**, 229-235 (1991).

[119] Moslemian D., Chen M. M. and Chao B. T., "Heat-Transfer to Horizontal Tubes in a Fluidized-Bed - the Role of Superficial Gas and Local Particle Velocities," *Experimental Thermal and Fluid Science*, **4**, 76-89 (1991).